LABORATORY CHARACTERIZATION OF GEOMECHANICAL AND HYDRAULIC PROPERTIES OF DEEP-SEA HYDRATE DEPOSITS

A Thesis
Presented to
The Academic Faculty

by

Jongchan Kim

In Partial Fulfillment
of the Requirements for the Degree
Doctor of Philosophy in the
School of Civil and Environmental Engineering

Georgia Institute of Technology
May 2020

LABORATORY CHARACTERIZATION OF GEOMECHANICAL AND HYDRAULIC PROPERTIES OF DEEP-SEA HYDRATE DEPOSITS

Approved by:

Dr. Susan E. Burns
School of Civil and Environmental Engineering
Georgia Institute of Technology

Dr. Sheng Dai, Advisor
School of Civil and Environmental Engineering
Georgia Institute of Technology

Dr. J. David Frost
School of Civil and Environmental Engineering
Georgia Institute of Technology

Dr. Zhigang Peng
School of Earth and Atmospheric Sciences
Georgia Institute of Technology

Dr. Yongkoo Seol
National Energy Technology Laboratory
Department of Energy

Date Approved: March 5, 2020

"With all your heart you must trust the Lord and not your own judgment.

Always let Him lead you, and He will clear the road for you to follow" (Proverbs 3:5-6)

ACKNOWLEDGMENTS

First of all, I would like to express my most profound appreciation to my advisor, Dr. Sheng Dai for his guidance, patience, insightful advice, encouragement, and all support thought my Ph.D. study. It is a great pleasure to be one of his graduate students at the Georgia Institute of Technology.

I would like to thank the members of my committee for their insightful and helpful comments and suggestion: Dr. Susan Burns, Dr. Davis Frost, Dr. Zhigang Peng, and Dr. Yongkoo Seol. I also wish to express my gratitude to my former advisor in Korea, Dr. Jong-Sub Lee for his excellent advice and support.

I also would like to thank the members of Subsurface Process Laboratory (SPL) for their help, discussion, and encouragement: Boyoung Jeong, Wilson Espinoza, Yimin Lu, Yumeng Zhao, Zhichao Liu, Lunxiang Zhang, and Haitao Zhang. Additionally, I would like to thank all of my colleagues and friends in the Geosystems at the Georgia Institute of Technology. I would also like to thank the Korean Civil Engineering Society.

Last but not least, my gratitude extends to my parents, Chulmo Kim and Jungsoon Ahn, my brother, Jonghyun Kim, and my sister, Hyeshin Kim, for their patience, dedicated support, and prayers. I would also like to thank my wife, Sungjin Park, my daughter, Yeseul Joy Kim, for their love, supports, and encouragements during my Ph.D. study.I do not believe that I could finish my work without their help.

TABLE OF CONTENTS

LIST OF FIGURES

SUMMARY

Methane hydrate has been considered as a future energy resource due to the vast amount of carbon in the hydrate reservoir. Gas production via the depressurization of pore water in deep-sea deposits may induce a significant increase in the effective stress of hydrate-bearing sediment. This stress increase can change the mechanical, physical, and hydraulic properties of hydrate-bearing sediments.

The central theme of this research is the fundamental investigation of the mechanical and hydraulic properties of hydrate-bearing sediments under various vertical stress in oedometer condition. An instrumented high-stress oedometer is used to investigate the sand grain crushing in hydrate-bearing sediments. The breakage index B_r and crushing parameters are adapted to quantify the degree of sand grain crushing. Using natural cored hydrate-bearing sediments from offshore India, compressibility, particle crushing, physical properties with elastic wave measurements, and permeability anisotropy are explored. Furthermore, hydrate morphology and elastic wave attenuation of hydrate-bearing clayey sediment are investigated using 3D X-ray computed tomography (CT) and elastic wave measurements.

The major findings of this research are as follows: (i) the presence of hydrate crystals restrains particle rotation and rearrangement during loading, resulting in less pronounced particle crushing in higher hydrate saturation sediments; (ii) hydrate saturation and applied stress levels play a vital role in the coefficient of earth pressure at rest K_0 with cementation debonding and the creep behavior of hydrate crystals; (iii) the permeability anisotropy of hydrate-bearing sediments increases exponentially with the increase of effective vertical

stress in oedometer condition, implying that vertical direction permeameter tests may underestimate the reservoir's flow performance; and (iv) the morphology and hydrate saturation of laboratory-made tetrahydrofuran hydrate-bearing clayey sediments are affected by temperature and induction time, and the sediments with higher hydrate saturation have higher *P*- and *S*-wave attenuations.

CHAPTER 1 INTRODUCTION

1.1 Motivation

Gas hydrates are clathrate compounds that are composed of gas molecules caged within water molecules (Sloan and Koh, 2007). The most common gas hydrate in nature is methane hydrate. Methane hydrates have been considered as a potential future energy resource due to the vast amount of reserves (Boswell and Collett, 2011, Sloan and Koh, 2007), a potential risk to the environment (Kvenvolden, 1993, Glasby, 2003, Ruppel and Pohlman, 2008), and a possible cause to large-scale submarine landslides (Kvenvolden, 1993, Kayen and Lee, 1991, Grozic, 2010). The amount of carbon from the methane hydrate exceeds the total amount of carbon from conventional sources such as coal, oil, and non-hydrate natural gas (Kvenvolden, 1993). Methane hydrate requires low temperature and high pressure conditions for its formation and stability, so methane hydrate deposits are commonly found in permafrost or deep-sea sediments (Kvenvolden, 1993). Therefore, the proper investigation of the physical and geomechanical properties of hydrate-bearing sediments is necessary to develop stable and economical production strategies.

To utilize methane hydrate as an energy resource, three practical hydrate dissociation methods, i.e., thermal stimulation, depressurization, and inhibitor injection, have been proposed for the recovery of methane gas from hydrate-bearing deposits (Holder et al., 1984, Moridis, 2002, Moridis, 2008). Depressurization method is considered to be a particularly efficient means of gas production in deep-sea or permafrost sediments (Moridis et al., 2009, Moridis and Reagan, 2007), and the process can cause significant increases in

effective stress by up to tens of megapascals, depending on the water depth and overburden stress in deep-sea sediments (Collett et al., 2019). This increase in effective stress can induce critical changes in the engineering properties' behavior of hydrate-bearing sediments.

The goal of this research is to explore the geomechanical and hydraulic properties of hydrate-bearing sediments under various vertical stress conditions. These properties, including the volumetric change, sand crushing, lateral stress response, elastic wave velocity, and permeability anisotropic of tetrahydrofuran (THF) hydrate-bearing sediments, are experimentally investigated using instrumented experimental cells. Moreover, the hydrate morphology and wave attenuation of THF hydrate-bearing clayey sediments are examined using 3D X-ray computed tomography (CT) scanning and elastic wave measurements.

1.2 Tetrahydrofuran Hydrate

Tetrahydrofuran (THF) hydrate is a suitable analog for methane hydrate in this research because of mechanical properties and core scale distribution similarities between the two hydrates. Moreover, THF hydrate allows having a simpler experimental setup and more precise control of hydrate saturation compared to that for methane hydrate.

Notably that although THF and methane form Structure II and Structure I hydrates respectively, they both present similar physical properties, such as density ρ = ~910 kg/m^3, shear wave velocity V_s = 1,890-1,950 m/s, tensile strength σ_t = 0.16-0.18 MPa, and adhesion strength to minerals σ_{ad} = 0.1-0.15 MPa (Jung and Santamarina, 2011, Sloan and Koh, 2007, Helgerud et al., 2003, Lee et al., 2007). As reviewed by Lee et al. (Lee et al.,

2007), the wave velocities of sediments containing both hydrates are similar, and their measured strengths also overlap. The mechanical properties of hydrate-bearing sediment, however, depend critically on the pore-space morphology of the hydrate (Dvorkin et al., 2000, Dai et al., 2012), and the macroscale mechanical properties of hydrate-bearing sediments are mostly affected by the pore-scale spatial distribution of hydrate rather than the differences between THF and methane hydrate crystals themselves (Lee et al., 2007).

Such tests using methane hydrate are extremely challenging due to (i) high pressure to keep hydrate stable must be maintained throughout the tests; (ii) hydrate saturation may be subjected to change during water circulation for permeability measurement; and (iii) forming methane hydrate with high saturation is extremely time-consuming. Additionally, THF is soluble in water. The formed THF hydrate has no preferential nucleation site in a typical pore. The pore habit of THF hydrate (Mahabadi et al., 2016a, Tohidi et al., 2001) resembles that of methane hydrate formed from dissolved methane in pore water (Buffett and Zatsepina, 2000, Spangenberg et al., 2005, Spangenberg et al., 2014), although concentrated gas hydrate accumulation may result from methane migration in gas phase (Collett et al., 2010) and corresponding hydrate pore habit has not been well studied.

1.3 Thesis Organization

The work performed in this study focuses on the geotechnical properties of THF hydrate-bearing sediments under various vertical stress conditions with taking hydrate formation and dissociation processes into consideration. This thesis is divided into the following chapters:

Chapter 2 explores how the presence of hydrate crystals affects sand grain crushing. Vertical stress up to 40 MPa is applied to the various hydrate-saturated sediment to generate the sand grain crushing. The breakage index B_r and crushing parameters are calculated based on the grain size distribution before and after the tests. The changes in hydraulic conductivity caused by the particle crushing are estimated based on the evolution of particle size.

Chapter 3 is a case study focusing on the compressibility and particle crushing of natural hydrate-bearing sediment cores obtained from offshore India. THF hydrate is formed in the natural sediments, and the physical and geomechanical properties of the sediments experienced loading up to 25 MPa vertical stress are investigated.

Chapter 4 investigates the coefficient of earth pressure at rest K_0 of hydrate-bearing sediments with various hydrate saturation. A thick wall oedometer cell is designed to apply relatively high vertical stress up to 25 MPa, which is sufficient to break the cementation bonding and to cause particle crushing. Also, the lateral stress response during hydrate formation and dissociation is monitored.

Chapter 5 provides the permeability anisotropy of hydrate-bearing sediments under various vertical stress conditions. A customized flow anisotropy cell is used to evaluate the hydraulic properties of natural cores recovered from offshore India. Both the vertical and lateral permeabilities of the hydrate-bearing sediments are measured under various vertical stress levels.

Chapter 6 details the hydrate distribution in clayey sediments and its effects on the physical properties. This study uses X-ray CT to visualize the distribution of hydrate in

kaolinite sediments. A series of *P*- and *S*-wave signatures are measured to explore the underlying physics of hydrate formation in fine-grained sediments and to enhance the wave-based characterization of hydrate-bearing clays.

This research has resulted in the following journal manuscripts published or in preparation:

Chapter 2: Kim, J., Zhang, Y., Seol, Y., and Dai, S., 2019. Particle crushing in tetrahydrofuran hydrate-bearing sands. *Geomechanics for Energy and the Environment*, https://doi.org/10.1016/j.gete.2019.100133

Chapter 3: Kim, J., Dai, S., Jang, J., Waite, W.F., Collett, T.S. and Kumar, P., 2019. Compressibility and particle crushing of Krishna-Godavari Basin sediments from offshore India: Implications for gas production from deep-water gas hydrate deposits. *Marine and Petroleum Geology*, 108, pp.697-704.

Chapter 4: Kim, J. and Dai, S., Coefficient of earth pressure at rest of hydrate-bearing sediments, In preparation.

Chapter 5: Dai, S., Kim, J., Xu, Y., Waite, W.F., Jang, J., Yoneda, J., Collett, T.S. and Kumar, P., 2019. Permeability anisotropy and relative permeability in sediments from the National Gas Hydrate Program Expedition 02, offshore India. *Marine and Petroleum Geology*, 108, pp.705-713.

Chapter 6: Liu, Z., Kim, J., Lei, L., Ning, F., and Dai, S., 2019. Tetrahydrofuran hydrate in clayey sediments–laboratory formation, morphology, and wave characterization. *Journal of Geophysical Research: Solid Earth*, 124, pp.3307-3319.

CHAPTER 2 PARTICLE CRUSHING IN HYDRATE-BEARING SEDIMENT

2.1 Introduction

The depressurization of natural hydrate deposits to extract methane gas can increase the effective stress in hydrate-bearing sediments. Such stress increase may induce grain crushing and lead to additional sediment deformation and permeability reduction. Sand crushing is mainly affected by particle size and shape, relative density, grain mineralogy, grain size distribution, and the stress level (Lade et al., 1996, Lee and Farhoomand, 1967, Nakata et al., 2001, Hardin, 1985, Billam, 1972, McDowell et al., 1996). For quartz sand, minor sand crushing occurs at effective stress of 2-6 MPa, and massive sand crushing happens when the stress exceeds 10-20 MPa (Chuhan et al., 2002, Bellotti et al., 1991, Hagerty et al., 1993). Sand crushing may become detrimental to gas production because the breakage of solid particles can cause extra volume contraction (Zheng and Tannant, 2016, Mesri and Vardhanabhuti, 2009) and permeability reduction (Zheng and Tannant, 2016), as well as generate finer particles exacerbating solids migration and sand production. Thus, an enhanced understanding of sand crushing in hydrate-bearing sediments is critical to developing efficient and safe gas production strategies.

This study experimentally investigates how the presence of tetrahydrofuran (THF) hydrate crystals in sands affects sand particle crushing. Sands with various saturation of THF hydrate are loaded up to 40 MPa vertical stress within an oedometer cell. The vertical strain, grain size distributions before and after loading, and scanning electron microscopy (SEM) images of crushed particles are obtained. The results quantitatively demonstrate the

effect of hydrate on sand crushing and the consequent volumetric and conductivity changes in hydrate-bearing sediments.

2.2 Experimental Study

2.2.1 Experimental Setup

A customized stainless steel oedometer cell (with 50.8 mm inner diameter and 152.4 mm outer diameter) is used in this study. The oedometer cell is instrumented with a T-type thermocouple to monitor the temperature within the specimen during the test. An additional thermocouple is placed outside but right next to the oedometer cell to monitor the environment temperature. The vertical load is applied using a manually controlled hydraulic pump and measured using a load cell. The vertical displacement is measured using a linear variable displacement transducer (LVDT). The whole setup is placed within a walk-in environmental chamber (Darwin Chamber TH055) for temperature control during hydrate formation and dissociation.

2.2.2 Specimen Preparation

Two types of sands, F110 and Ottawa 20/30, are used. The F110 sand have a mean grain diameter D_{50} = 120 μm, specific gravity G_s = 2.65, uniformity coefficient C_u = 1.82, and maximum and minimum void ratios $e_{max/min}$ = 0.85/0.54. The Ottawa 20/30 sand is slightly bigger in size with mean grain diameter D_{50} = 720 μm, specific gravity G_s = 2.65, uniformity coefficient C_u = 1.21, and maximum and minimum void ratios $e_{max/min}$ = 0.74/0.50. The grain size distributions and microscope images of the two types of sands are shown in Figure 2.1.

The sands are saturated by aqueous mixtures of THF solution and deionized water with various pre-determined mass ratios to achieve different targeted hydrate saturation in the specimens. In this study, four hydrate saturation cases are tested, i.e., S_h = 0, 0.3, 0.6 and 0.96. The corresponding THF:H_2O mass ratios are 0:100, 9.8:90.2, 14.3:85.7, and 20.3:79.7, respectively (Strauch et al., 2018). All specimens are then packed into the oedometer cell with a relative density D_r = 40%. The corresponding initial void ratios are e_0 = 0.74 for F110 and e_0 = 0.65 for Ottawa 20/30 sands.

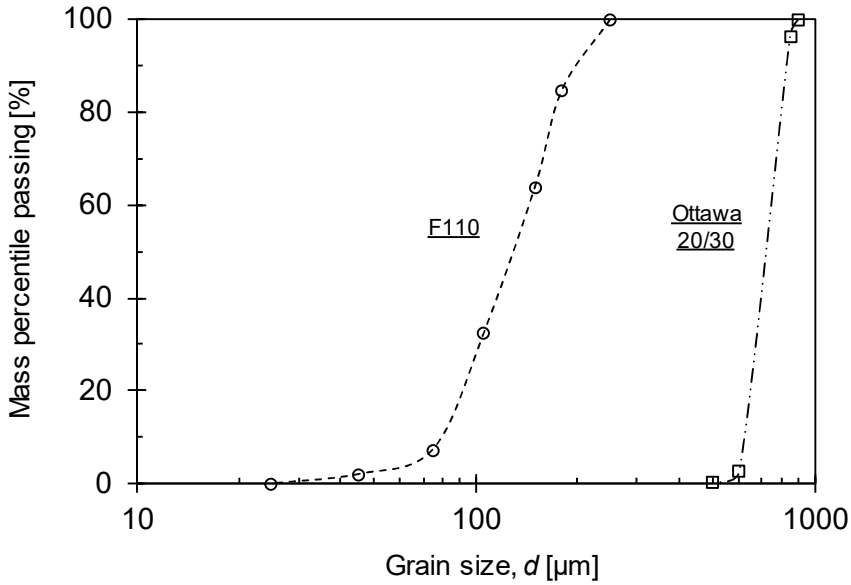

Figure 2.1 − The initial grain size distribution of F110 fine and Ottawa 20/30 coarse sands.

2.2.3 Experimental Procedures

After packing the specimen in the oedometer cell, the self-weight of the top cap induces a vertical stress σ_v = 0.007 MPa in the specimen. The temperature of the environmental chamber is then decreased to 0.3°C and kept constant to trigger THF hydrate

formation without freezing the water. Hydrate forms when the thermocouple signatures show a thermal spike. Then the temperature is kept constant for an additional 12 hours to ensure sufficient crystal nucleation and growth time. After that, additional vertical stress is applied using the hydraulic pump. Four different maximum vertical stress, σ_{max} = 15, 25, 35, and 40 MPa, are tested using specimens with and without hydrate. The loading is applied at a rate of 5 MPa per minute until the targeted maximum vertical stress is achieved. The maximum stress is then kept constant until no evident vertical deformation (i.e., the change in vertical strain is $\Delta\varepsilon_v < 10^{-4}$ over one minute) is observed. After that, the applied vertical stress is unloaded to 2 MPa, and then hydrate is dissociated by increasing the temperature at this stress.

A set of complementary tests using Ottawa 20/30 sand with S_h = 0, 0.3, 0.6, and 0.96 are all loaded up to σ_{max} = 25 MPa to evaluate the effects of particle size and shape on sand crushing in hydrate-bearing sediments.

Grain size distributions before and after the tests for each specimen are measured using sieve analysis (ASTM C136). Temperature and vertical deformation of the tested specimens are continuously monitored throughout the experiments.

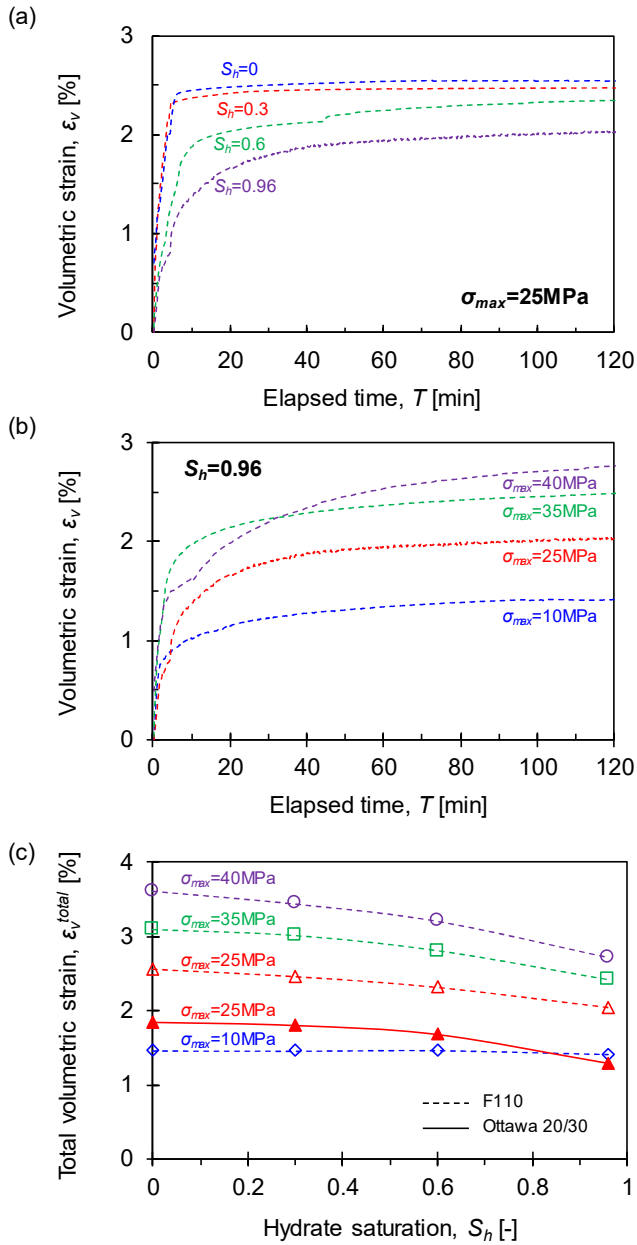

Figure 2.2 − Changes in volumetric strain ε_v of F110 hydrate-free and hydrate-bearing specimens. (a) Volumetric strain ε_v versus elapsed time with 25 MPa maximum vertical stress. (b) Volumetric strain ε_v versus elapsed time of S_h = 0.96 specimens. (c) Total volumetric strain ε_v^{total} versus hydrate saturation. The hydrate-bearing F110 specimens (empty markers with dotted line) and hydrate-bearing Ottawa 20/30 specimens (solid markers with solid line) are plotted.

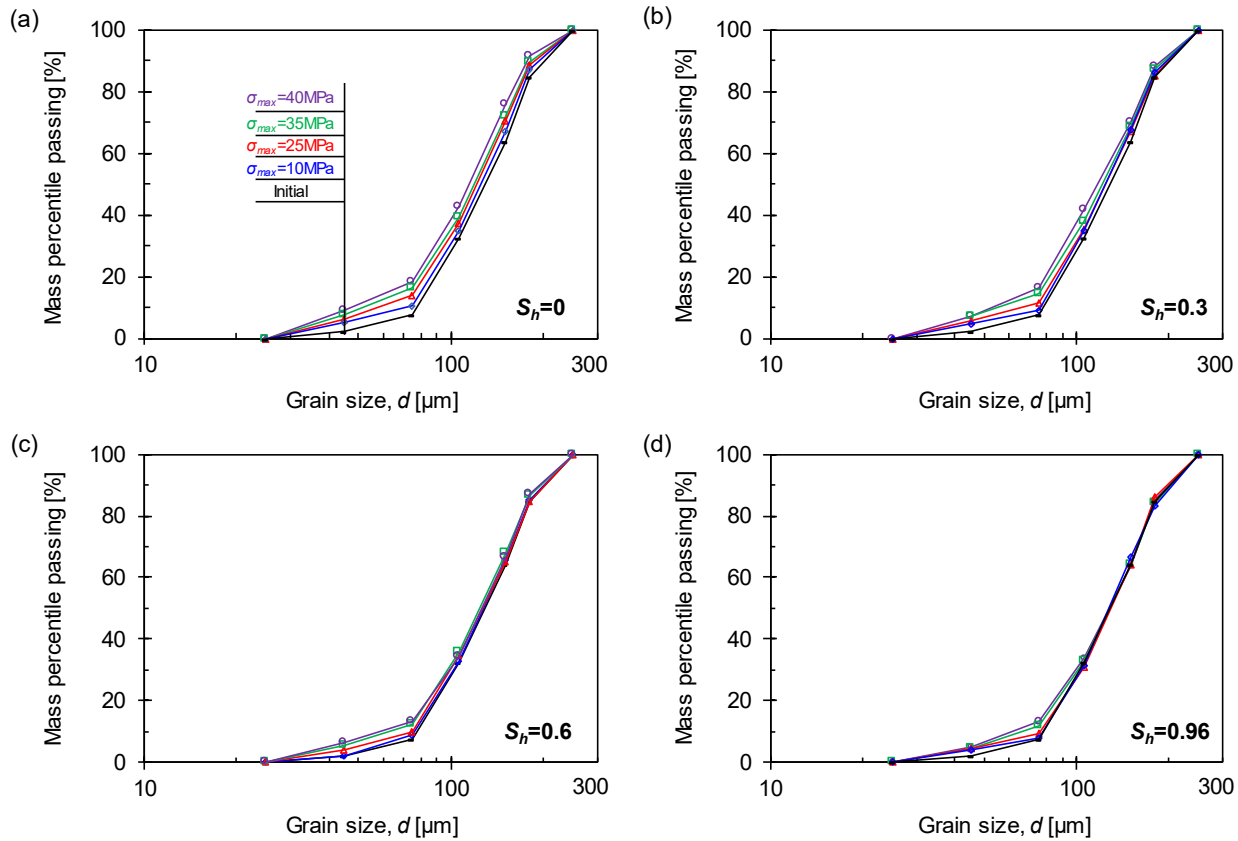

Figure 2.3 − The grain size distribution of tested F110 specimens with various hydrate saturation S_h. (a) S_h = 0. (b) S_h = 0.3. (c) S_h = 0.6. (d) S_h = 0.96. The hydrate-bearing specimens are experienced the various maximum vertical stress (σ_{max} = 10, 25, 35, and 40 MPa).

2.3 Experimental Result

2.3.1 Stress-Volume Responses

Figure 2.2a shows the volumetric strain ε_v with time during the loading up to 25 MPa for F110 sands with S_h = 0, 0.3, 0.6, and 0.96. Note that specimens in an oedometer test have zero lateral strain so that the volume metric strain ε_v equals the vertical strain ε_z, which is measured by using the LVDT. Since the loading rate is 5 MPa per minute, it takes approximately 5 minutes to reach the targeted maximum vertical stress of 25 MPa in this set of tests. Then the vertical stress is held constant until no evident vertical deformation is observed. The total deformation is less pronounced in specimens with higher hydrate saturation. Additionally, the total volumetric strain in specimens with identical hydrate saturation increases with the applied maximum vertical stress, as shown in Figure 2.2b.

Figure 2.2c summarizes the total volumetric strain of tested F110 sand with various hydrate saturation subjected to different maximum vertical stresses, and that of the Ottawa 20/30 sand with various hydrate saturation subjected to the maximum vertical stress of 25 MPa. It is observed that the Ottawa 20/30 specimens undergo less volumetric strain compared to the F110 specimens under identical hydrate saturation and loading conditions.

2.3.2 Sand Crushing

Figure 2.3 shows the grain size distributions of all tested F110 specimens before and after loading. Loading breaks the grains and generates solids with smaller particle sizes. This shifts the post-loading grain size distribution curves left- and upwardly compared to their initial grain size distribution curves before loading. The more evident shift in grain

size distribution curves indicates more pronounced sand crushing. Thus, specimens with fewer amounts of hydrate and under higher stress are more susceptible to sand crushing.

2.4 Analyses and Discussion

2.4.1 The Breakage Index

The breakage index B_r is often used to quantify the extent of grain crushing (Hardin, 1985, Einav, 2007a, Hyodo et al., 2016, Xiao et al., 2015). Figure 2.4a illustrates the calculation of the breakage index based on certain area measurements of the grain size distribution curves before and after the loading (Einav, 2007a, Hardin, 1985, Einav, 2007b):

$$B_r = \frac{B_t}{B_p} \tag{2-1}$$

where B_t refers to the area between the post-crushing and the initial grain size distribution curves (i.e., area B in Figure 2.4a). B_p is the area between the ultimate F_u and the initial grain size distribution curves (i.e., areas A+B in Figure 2.4a). The ultimate distribution curve F_u reflects the grain size distribution at the ultimate potential of sand crushing and can be computed as (Einav, 2007a):

$$F_u = \left(\frac{d}{d_{\max}} \right)^{3-\alpha} \tag{2-2}$$

where d represents the sand particle size of the ultimate distribution and d_{max} is the maximum particle size of the initial grain size distribution. The fractal dimension α is assumed to be 2.6 for sands (Coop et al., 2004).

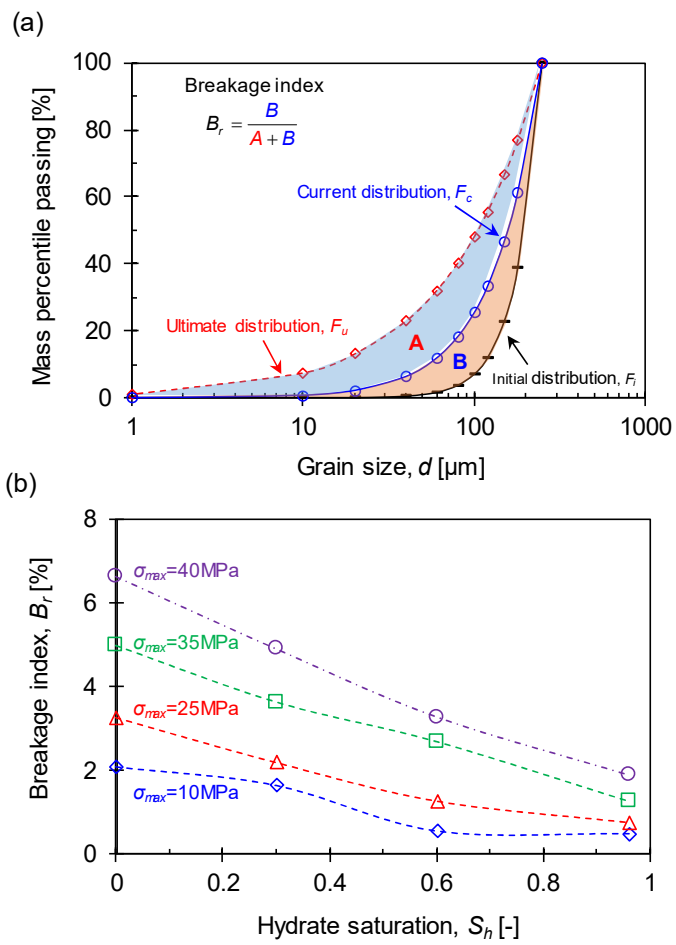

Figure 2.4 − Breakage index B_r of F110 hydrate-free (S_h = 0, water-saturated) and hydrate-bearing (S_h = 0.3, 0.6, and 0.96). (a) Illustration of the breakage index B_r. (b) The breakage index B_r of tested F110 specimens.

Figure 2.4b summarizes the values of the calculated breakage index for all F110 specimens tested in this study. The results show that more pronounced sand crushing occurs in specimens with lower hydrate saturation subjected to higher maximum stress. To

some extent, the presence of hydrate stiffens the sand skeleton and yields smaller strain (i.e., particle deformation) under the same stress condition (see also Figure 2.2c); and additionally, the hydrate crystals can carry part of the load. Therefore, the presence of hydrate can help mitigate sand crushing and that the loss of hydrate crystals during gas production from hydrate deposits can exacerbate particle crushing and finer solids generation (Kim et al., 2019a).

2.4.2 Effects of Maximum Stress and Hydrate Saturation

To furtherly quantify the reduction in particle size due to grain breakage, the following parameters P_{10}, P_{50}, and P_{90} are calculated:

$$P_{10} = \frac{D_{10}^{current}}{D_{10}^{initial}} \tag{2-3}$$

$$P_{50} = \frac{D_{50}^{current}}{D_{50}^{initial}} \tag{2-4}$$

$$P_{90} = \frac{D_{90}^{current}}{D_{90}^{initial}} \tag{2-5}$$

where D-values (i.e., D_{10}, D_{50}, and D_{90}) are the particle sizes corresponding to the 10%, 50%, and 90% of the cumulative mass on the grain size distribution curves. The superscripts (i.e., initial and current) refer to the D-values before and after the loading. Therefore, the crushing parameter P_{10} reflects the change in the characteristic particle size D_{10} before and after sand crushing, and likewise for P_{50} and P_{90}.

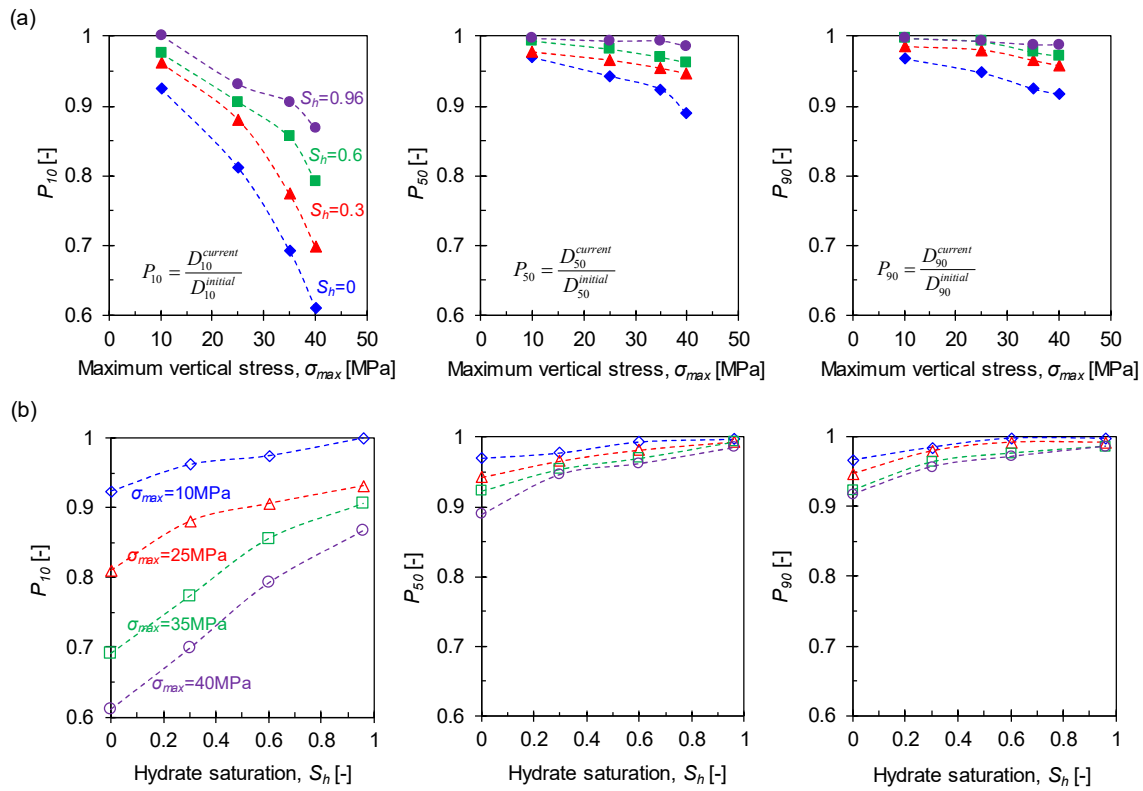

Figure 2.5 − Crushing parameters (i.e., P_{10}, P_{50}, and P_{90}) of F110 hydrate-free (S_h = 0, water-saturated) and hydrate-bearing specimens (S_h = 0.3, 0.6, and 0.96). The hydrate is dissociated under 2 MPa vertical stress, then collected for the grain size distribution analysis. (a) Crushing parameters as a function of the maximum vertical stress. (b) Crushing parameters as a function of the hydrate saturation.

Figure 2.5 shows that the crushing parameters, i.e., P_{10}, P_{50}, and P_{90}, decrease with increasing maximum vertical stress and decreasing hydrate saturation in all tested specimens. The reduction in P_{10} is more evident than in P_{50} and P_{90} under identical stress and hydrate saturation conditions. This result highlights that particle crushing can significantly increase the content of finer particles in hydrate-bearing sediments adversely affecting gas production. The specimens with lower hydrate saturation subjected to higher maximum stress can generate a larger amount of finer particles.

Larger particles surrounded and cushioned by small particles are less susceptible to be massively fractured, but more likely to generate asperities from the surface and edges without significant changes in size (Sadrekarimi and Olson, 2010, McDowell et al., 1996, Cheng et al., 2004, Nakata et al., 2001, Guimaraes et al., 2007). Scanning electron microscopy (SEM) images of tested sands before and after loading are shown in Figure 2.6. For F110 sands, significant amounts of finer particles are generated from the splitting of large particles into intermediate and even smaller particles. Generated fine particles (Figure 2.6c) are very angular but still with a high roundness. However, for Ottawa 20/30 sands, larger particles undergo predominantly surface grinding and shear-off asperities, resulting in angular fine particles with low roundness.

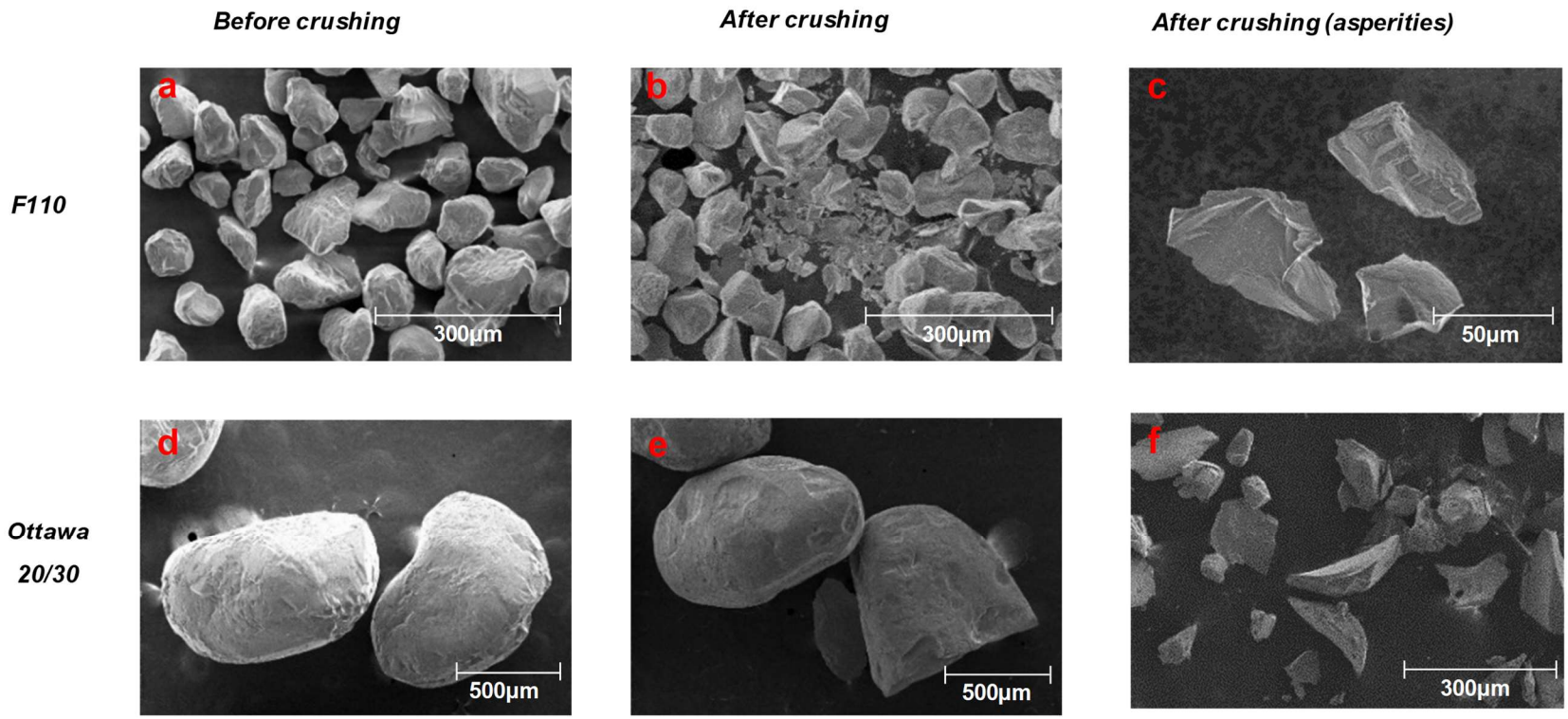

Figure 2.6 − Scanning electron microscopy images of F110 and Ottawa 20/30 sands with hydrate saturation S_h = 0.3 and the maximum applied vertical stress σ_{max} = 40 MPa.

2.4.3 Effects of Stress History

Effects of stress history are investigated by loading an additional set of hydrate-bearing F110 sands up to 25 MPa, at which stress the hydrate is dissociated by increasing the temperature. The results are compared with that of the specimen being loaded to 25 MPa and then unloaded to 2MPa at which stress the hydrate is dissociated. In both stress paths, the specimens experience 25 MPa maximum vertical stress but the hydrate is dissociated at different vertical stresses (i.e., 2 MPa versus 25 MPa), as illustrated in Figure 2.7a.

Figure 2.7b shows the calculated breakage index values for the two sets of tests. The results show that the degree of sand crushing decreases with the increase of hydrate saturation, and the specimens with hydrate dissociated at 25 MPa vertical stress have more pronounced sand crushing than those with hydrate dissociated at 2 MPa. As shown in Figure 2.7c, the characteristic particle size D_{10} decreases more in specimens that hydrate is dissociated at 25 MPa than at 2MPa. The P_{50} values (i.e., the reduction in the mean particle size D_{50}) show minor differences. For the specimens that hydrate is dissociated at 25 MPa, the particle skeleton experiences maximally 25 MPa stress; while for those that hydrate is dissociated at 2 MPa, even though the maximally applied total stress is 25 MPa, the particle skeleton may experience less stress as hydrate crystals may carry part of the load. During hydrate dissociation, the stress carried by the hydrate crystals will transit to the sand particles that result in an increase in effective stress. Therefore, more pronounced sand crushing is observed in the specimens where hydrate is dissociated at 25 MPa.

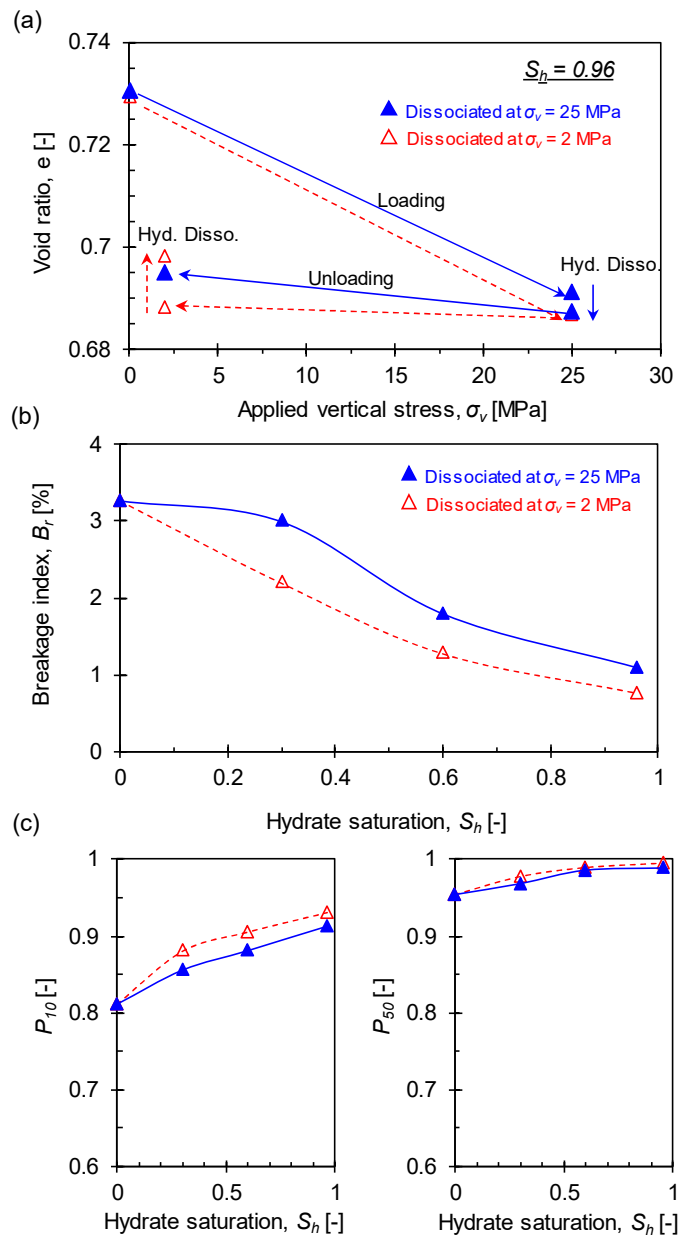

Figure 2.7 – Effects of stress history during the hydrate dissociation on sand crushing. The hydrate-bearing specimens are experienced 25 MPa vertical stress, and hydrate is dissociated under 2 MPa (red markers and dotted line) and 25 MPa (blue markers and solid line). (a) Changes in the void ratio of hydrate-bearing F110 specimens with S_h = 0.96. (b) Comparison of breakage index B_r. (c) Comparison of crushing parameters P_{10} and P_{50}.

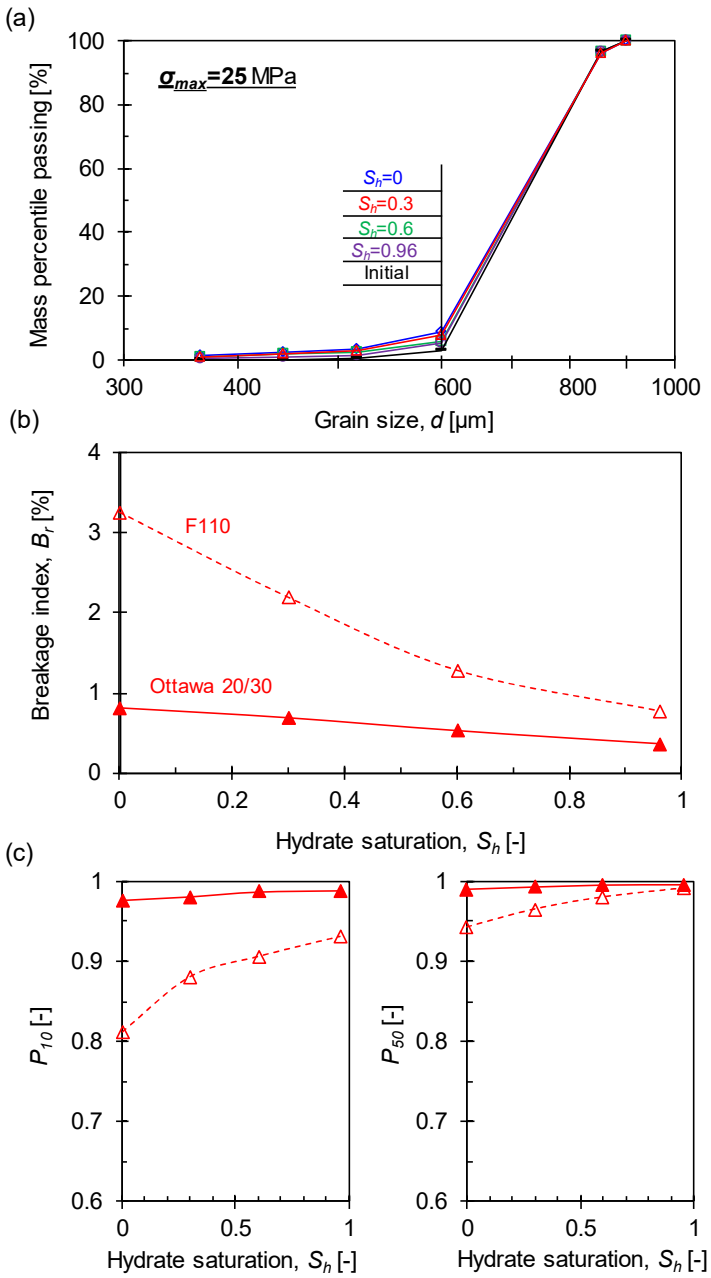

Figure 2.8 − Effect of particle size on sand crushing of F110 and Ottawa 20/30 specimens with various hydrate saturation. The hydrate-bearing specimens are experienced 25 MPa vertical stress, and hydrate is dissociated under 2 MPa. (a) The grain size distribution of Ottawa 20/30 specimens. (b) Comparison of breakage index B_r. (c) Comparison of crushing parameters P_{10} and P_{50}.

2.4.4 Effects of Particle Size

Figure 2.8a shows the grain size distribution curves of Ottawa 20/30 sands with various hydrate saturation before and after 25 MPa loading. The results are also compared with that in F110 specimens (Figure 2.8b and Figure 2.8c). Similarly, the most pronounced sand crushing is observed in hydrate-free specimens and the presence of hydrate inhibits sand crushing. Less pronounced sand crushing is observed in Ottawa 20/30 specimens and the F110 specimens. This is consistent with the particle size evolution, i.e., more evident reduction in the crushing parameters, P_{10} and P_{50}, for F110 compared to Ottawa 20/30 specimens (Figure 2.8c). This may in part because Ottawa 20/30 sand has higher stiffness and thus less volumetric deformation than F110 specimens do.

2.4.5 Total Volumetric Strain in Hydrate-Bearing Sands

The volumetric strain (i.e., contraction) in hydrate-bearing sands subjected to stress is mainly caused by skeleton deformation and partly from particle crushing. The particle crushing can occur when the effective stress exceeds the particle's yield strength. The total volumetric strain of hydrate-bearing sands depends on the specimen's compressibility, initial packing, hydrate saturation, and the maximally applied stress. Therefore, it can be predicted by:

$$\varepsilon_v = 90 \cdot \frac{a_v}{(1+e_0)} \cdot \frac{\sigma_{\max}^{\beta}}{(1+S_h)^{1-\beta}} \tag{2-6}$$

where, a_v = 0.0035 is the coefficient of compressibility of the hydrate-free specimen at 1 MPa vertical stress; e_0 is the initial void ratio; σ_{max} is the maximum vertical stress applied,

and S_h is the hydrate saturation. The constant 90 and the exponent β = 0.7 are fitting parameters obtained from the results of all tested specimens (Figure 2.9). This equation provides a satisfactory estimation of the total volumetric strain in hydrate-bearing sands under certain vertical stress conditions.

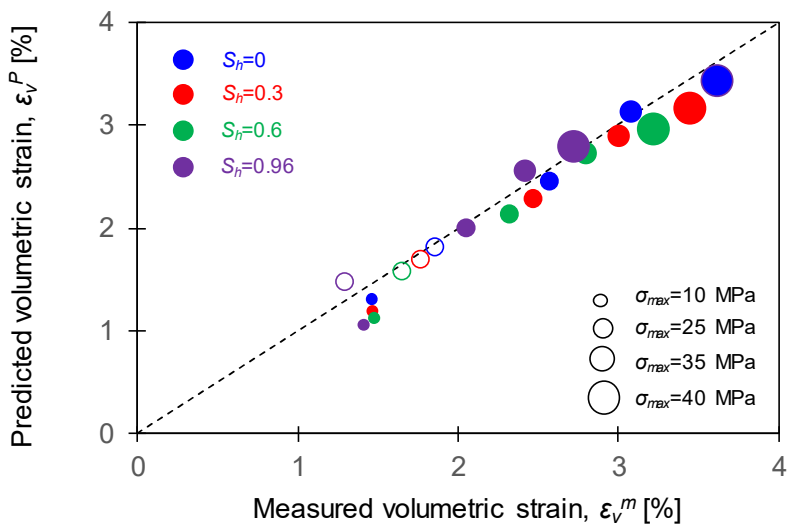

Figure 2.9 − Validation of predicted volumetric strain for all tested F110 (Solid markers) and Ottawa 20/30 (empty markers) specimens. Marker size indicates the magnitude of applied vertical stress.

2.4.6 Hydraulic Conductivity Reduction due to Sand Crushing

The hydraulic conductivity of soils can be expressed using a semi-theoretical equation (Kozeny, 1927, Carman, 1939):

$$k = \left(\frac{\gamma}{\mu}\right) \cdot \left(\frac{1}{C_{K-C}}\right) \cdot \left(\frac{e^3}{S_s^2 \cdot (1+e)}\right) \tag{2-7}$$

where γ is the unit weight of permeant; μ is the viscosity of the permeant; $C_{K\text{-}C}$ is an empirical coefficient; e is the void ratio; S_s is the specific surface area per unit volume of the particles. The specific surface can be estimated using the grain size distribution as (Santamarina et al., 2002):

$$S_s = \frac{3 \cdot (C_u + 7)}{4 \cdot \rho_w \cdot G_s \cdot D_{50}} \tag{2-8}$$

where C_u is the coefficient of uniformity; ρ_w is the mass density of water; G_s is the specific gravity of the particles. Assuming material properties (i.e., γ, μ, G_s, ρ_w) are constants, the hydraulic conductivity becomes a function of void ratio e, mean particle size D_{50}, and the coefficient of uniformity C_u as:

$$k \propto \frac{e^3 D_{50}^2}{(1+e)(C_u + 7)^2} \tag{2-9}$$

Since these three parameters are known for all tested specimens before and after sand crushing, one can calculate the reduction in hydraulic conductivity $k_{crushing}/k_{ini}$, where subscripts *crushing* and *ini* represent post-crushing and initial states. Figure 2.10 shows the reduction in hydraulic conductivity due to sand crushing as a function of the breakage index. Even a small breakage index of B_r = 3% can cause an approximately 50% reduction in specimen's hydraulic conductivity.

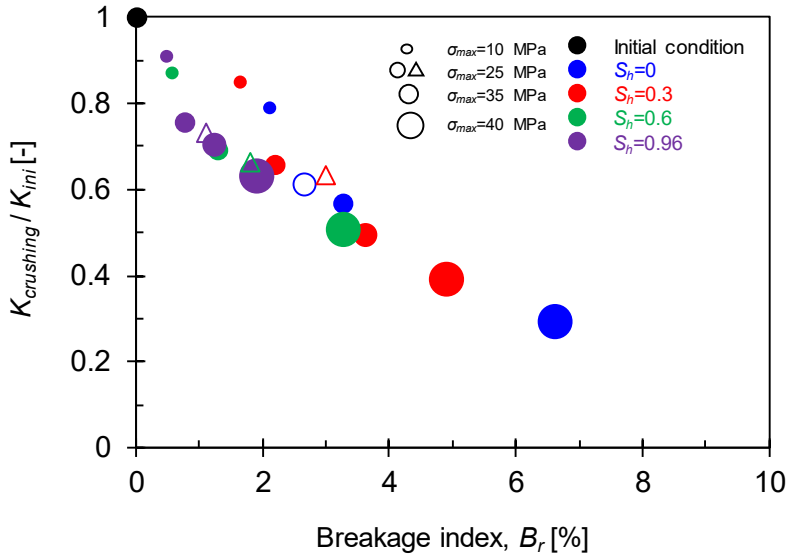

Figure 2.10 − Sand crushing induced a reduction in hydraulic conductivity. Hydrate saturation and the maximum vertical stress of the tested specimens are indicated by the color and the size of the markers. Circles represent F110 specimens and triangles Ottawa 20/30 specimens.

2.5 Conclusions

This study experimentally investigates the effects of hydrate crystals on the crushing characteristics of hydrate-bearing sediments. Salient observations can be summarized as the following:

- As quantified by the particle size reduction parameters and the breakage index values, the presence of hydrate crystals inhibits sand particle crushing. Hydrate crystals can stiffen sand skeleton stiffness, restrain particles from rotation and rearrangement, and at the same time share part of the total stress during loading. Therefore, the loss of hydrate crystals during gas production from hydrate deposits can exacerbate particle crushing.

- Sand particle crushing generates finer particles. The grain size distribution analyses show that relatively larger sand particles undergo surface grinding and breakage and contribute to the increase of the smaller particle proportion. Finer particles generated from crushing are very angular.

- Stress-dissociation history affects the extent of sand crushing in hydrate-bearing sediments. The stress transfer due to hydrate dissociation or pore pressure change alters the effective stress, which governs the sand crushing.

- The total volumetric strain in hydrate-bearing sands decreases with increased hydrate saturation and reduced maximum effective stress. Specimens with higher hydrate saturation undergo more considerable creep deformation, possibly due to the creep of THF hydrate crystals. The total volumetric strain in hydrate-bearing sediments can be estimated using Equation (2-6) with known hydrate saturation, skeleton stiffness, and effective stress.

- The estimation of hydraulic conductivity reduction due to sand crushing suggests that a breakage index of $B_r = 3\%$ can reduce the specimen's hydraulic conductivity by 50%.

CHAPTER 3 CASE STUDY – COMPRESSIBILITY AND PARTICLE CRUSHING OF NATURAL SEDIMENTS FROM OFFSHORE INDIA

3.1 Introduction

Hydrate-bearing sediments in some deep-water reservoirs like in the Krishna-Godavari Basin are subjected to ~30 MPa total stress in situ, i.e., ~25-28 MPa water pressure and ~1-3 MPa effective stress depending on the core below seafloor (Collett et al., 2019, Kumar et al., 2019). To simulate gas production at the NGHP-02-16 site, Myshakin et al. (Myshakin et al., 2019) consider depressurizing the reservoir down to 3 MPa pore pressure (barely above the ice point in terms of the gas hydrate stability curve). Given the water depths and overburden, such depression will cause a pore pressure drop of nearly 20-25 MPa (Boswell et al., 2019). The decreased pore pressure means more of the total overburden stress will be transferred onto the sediment skeleton, increasing the effective stress that essentially determines soil behavior in accordance with the sediment's compressibility, sand crushing, and permeability. Measuring the effective stress dependence of these soil behavior parameters is essential for evaluating deep-water gas hydrate deposits in terms of potential gas production efficiency and geomechanical stability.

This study investigates the physical and geomechanical properties of natural sediments subjected to high effective stresses of up to 25 MPa to match the modeled peak effective stress applied to the target reservoir. Here the focus is on stiffness, compressibility, and sand crushing. During India's National Gas Hydrate Program Expedition 02 (NGHP-02) in the spring of 2015, pressure cores were collected, preserving hydrate-bearing

sediment from offshore Eastern India (Collett et al., 2019, Kumar et al., 2019, Myshakin et al., 2019). Sediment tested in this study was collected from Site NGHP-02-23 (Figure 3.1), which penetrated an interbedded unit of high and low hydrate saturation sediment at the anticline crest of Area B. This is the same gas hydrate reservoir modeled at Site NGHP-02-16 by Myshakin et al. (Myshakin et al., 2019) and Boswell et al. (Boswell et al., 2018). Additional details about Site NGHP-02-23 and the Area-B anticline crest reservoir are presented by Jang et al. (Jang et al., 2019) and Collett et al. (Collett et al., 2019).

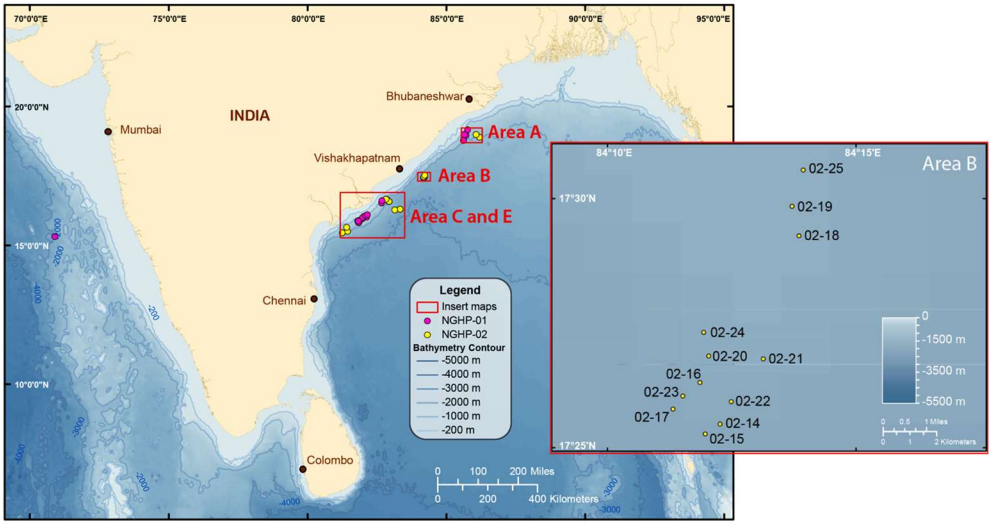

Figure 3.1 − Area map indicating the NGHP drill sites from the 2006 NGHP-01 expedition (red circles) and the 2015 NGHP-02 expedition (yellow circles). The specimen tested in this study is from the primary hydrate reservoir at the crest of the Area B anticline that was cored at Sites NGHP02-16, -17, and -23.

The material tested here, from Core NGHP-02-23C-10P, is a sandy silt subsection spanning the interval 284.5-284.65 mbsf from within a highly hydrate-saturated layer near the base of the primary gas hydrate reservoir. The water depth at this site is 2,553.5 m and the base of gas hydrate occurrence is at 289 mbsf (Collett et al., 2019, Waite et al., 2019).

This core was recovered as a pressure core, so elevated pressure (10-20 MPa) was maintained for the specimen during core recovery, initial property scans (Holland et al., 2019), storage and transport to the U.S. Geological Survey's Woods Hole Coastal and Marine Science Center (WHCMSC). Once the core had been depressurized, a whole-round subsample was shipped to the Georgia Institute of Technology for further geomechanical and hydraulic properties characterization of the sediments with and without tetrahydrofuran (THF) hydrate.

3.2 Experimental Design

3.2.1 Experimental Setup

The geomechanical responses of samples subjected to high effective stresses are measured using an instrumented oedometer cell (shown schematically in Figure 3.2). An oedometer cell measures soil deformation in response to effective stress change under the drained condition. The drainage port locates at the bottom pedestal, which also houses a T-type thermocouple for temperature monitoring, and a pair of piezo-cylinders and bender elements on the top and bottom pedestals are used for *P*- and *S*-wave measurements. A linear variable displacement transducer (LVDT) is affixed to the main body of the cell to measure the vertical deformation of tested specimens during loading and unloading. The vertical stress is applied using a hydraulic piston below the specimen. The applied stress is calculated from the specimen geometry and the measured oil pressure driving the hydraulic piston. All tests are conducted in a freezer with a temperature control accuracy of 0.1°C.

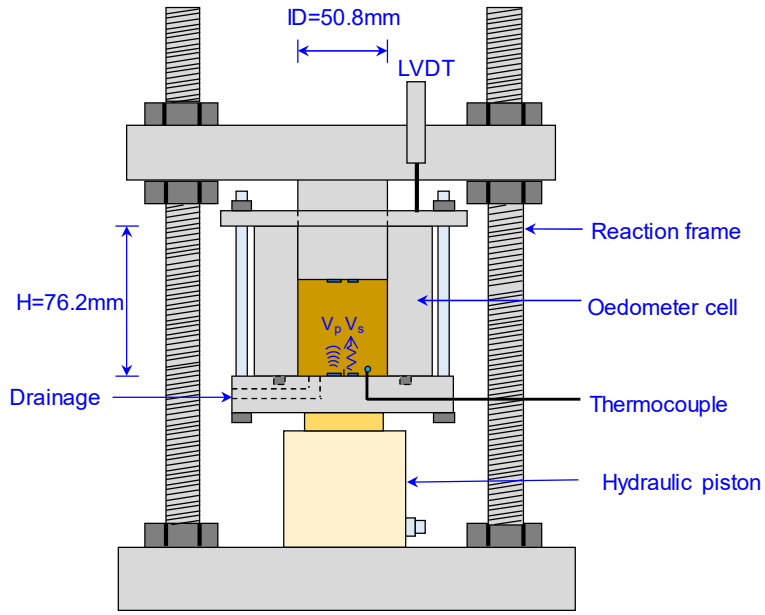

Figure 3.2 − A schematic illustration of the experimental setup. Specimens are tested within an oedometer cell, equipped with *P*- and *S*-wave piezo crystals, a thermocouple for temperature measurement, and an LVDT for monitoring the specimen's height change during loading and unloading.

3.2.2 Sediments Characterization and Sample Preparation

The natural sediment core in this study was split for testing at three specimen test conditions: water-saturated with THF hydrate (S_h = 0.8), water-saturated with no hydrate (S_h = 0), and dry. Complementary sand crushing tests were performed on F110 fine and Ottawa 20/30 coarse sands. Specimen grain size distributions are shown in Figure 3.3. The hydrate saturation S_h = 0.8 was chosen to match the measured hydrate saturation calculated from the gas evolved from the core specimen during degassing S_h = 0.79 ± 0.03.

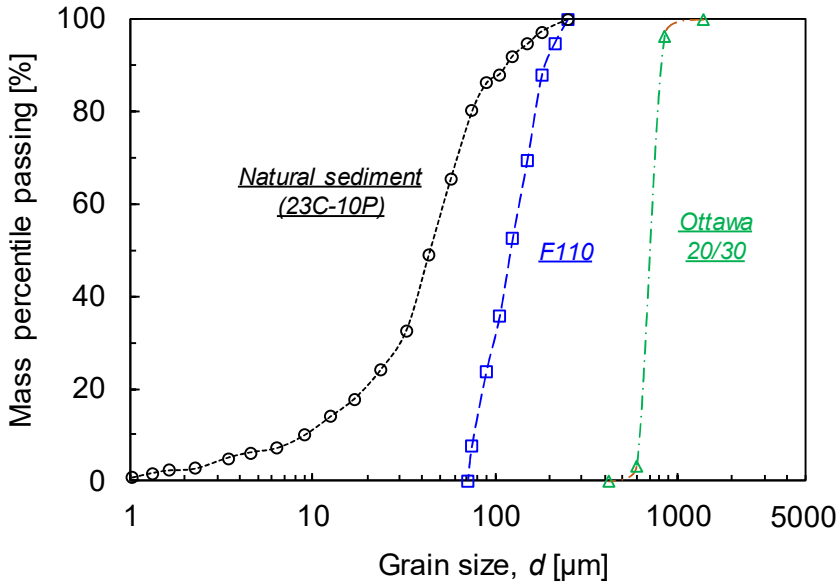

Figure 3.3 − The grain size distributions of sediments tested in this study: natural sandy silt sediment (Core NGHP-02-23C-10P), F110 fine sands, and Ottawa 20/30 coarse sands.

The natural gas hydrate reservoir sediment from Core NGHP-02-23C-10P tested in this study is classified as sandy silt, with 19% by mass of fine sands, 2% by mass of clay-sized particles, and a coefficient of uniformity c_u = 5.8. The core subsample has a median grain size d_{50} = 44.1 μm, characteristic grain size d_{10} = 9.0 μm, an initial void ratio e_o = 1.14, and specific gravity G_s = 2.65. The fine grains (< 75 μm only) have liquid limit LL% = 35.1, plastic limit PL% = 15.5, and specific surface S_s = 17.7 m^2/g. As a reference, typical specific surface area values for sands, kaolinite, illite, and montmorillonite are < 0.1, 10-30, 80-100, and 400-800 m^2/g, respectively (Jang and Santamarina, 2015).

The natural sediment for this study, initially received and retained as whole rounds in a plastic liner with an inner diameter of 53.8 mm, can be directly transferred into the instrumented oedometer cell which also has an inner diameter of 53.8 mm. To create a THF

hydrate saturation of 0.8, 200 ml of 17.3THF:82.7H_2O solution (Strauch et al., 2018) is initially circulated through the core to replace the original pore fluids. The 200 ml represents 30 times the original pore fluid volume. After circulating the THF mixture, the specimen temperature is lowered to -5ºC to trigger THF hydrate formation. Once a clear positive thermal spike is observed, indicating hydrate formation, the temperature is raised to 1ºC and held constant throughout the course of the tests to ensure no water ice is present.

The F110 fine sand is nearly pure quartz and has specific gravity $G_s = 2.65$, median grain size d_{50} = 120 μm, maximum and minimum void ratios $e_{max/min}$ = 0.85/0.54, and coefficient of uniformity $c_u = 1.7$. The Ottawa 20/30 coarse sand has specific gravity G_s = 2.65, median grain size d_{50} = 720 μm, maximum and minimum void ratios $e_{max/min}$ = 0.742/0.502, and coefficient of uniformity $c_u = 1.2$ (Cho et al., 2006). Complementary tests are run using F110 fine sand mixed with various mass ratios of THF and deionized water. To obtain S_h = 0.3, 0.6, and 0.96, mass ratios of 9.8THF:90.2H_2O, 14.3THF:87.5H_2O, and 20.3THF:79.7H_2O are used, respectively.

3.2.3 Experimental Procedures

The vertical effective stress on the samples inside the instrumented oedometer cell is increased in steps up to σ_v = 25 MPa, then unloaded to σ_v = 2 MPa. Each specimen, including the natural sediments with and without THF hydrate and F110 sands with various hydrate saturations, is allowed to consolidate (i.e., pore pressure equilibration back to atmospheric pressure) at each vertical stress level. The hydrate-bearing specimens are then dissociated after unloading to σ_v = 2 MPa by increasing temperature. Following dissociation, vertical stress is reduced to the initial stress condition σ_v = 7 kPa. The

specimen height is measured continuously through the test. For each loading and unloading step, consolidation is considered complete when the height stabilizes after each vertical effective stress change. The *P*- and *S*-wave velocities are measured after the specimen height stabilizes at each applied stress. Grain size distributions are also measured before and after each test to quantify the extent to which high stress causes particle crushing.

3.3 Experimental Results

3.3.1 Stress-Volume Relation

The stress-volume (void ratio) responses of the natural sediments are shown in Figure 3.4 for the specimen conditions: water-saturated with THF hydrate (S_h = 0.8), water-saturated with no hydrate (S_h = 0), and dry.

The natural sediments saturated with 17.3THF:82.7H_2O solution starts with an initial height of H_o = 58mm, corresponding to an initial void ratio of e_o = 1.13. Upon THF hydrate formation of S_h = 0.8 at σ_v = 7 kPa, the specimen's height increases 0.94 mm to H = 58.94 mm and the void ratio increases to e = 1.16. With the gradual increase in the vertical effective stress to σ_v = 25 MPa, the void ratio decreases to e = 1.01. The overall void ratio-stress curve appears to have a slightly convex-downward trend at higher stresses, which differs from typical trends in hydrate-free sediments that usually have no curvature and instead indicate a constant compression index C_c above the in situ stress. This convex-downward trend is also observed in other hydrate-bearing sediments from NGHP-02 loaded to high effective vertical stress (Yoneda et al., 2019a). When this specimen is unloaded from σ_v = 25 MPa to 2 MPa, height increases from H = 54.59 mm to 54.65 mm and the void ratio increases slightly from e = 1.006 to 1.008, with a swelling index C_s =

0.001. THF hydrate dissociation is then triggered at this stress, causing a settlement of 0.2 mm and a void ratio reduction from e = 1.008 to 1.000, in close agreement with the void ratios of the THF hydrate-free specimens that have only experienced a peak effective vertical stress of 2 MPa. Finally, the specimen is unloaded to σ_v = 7 kPa, with final height H_f = 15.64 mm and final void ratio e_f = 1.002.

For water-saturated natural sediments with no hydrate, the void ratio decreases from e_o = 1.15 to e = 0.89 when vertical load increases from σ_v = 7 kPa to 25 MPa, indicating much higher compressibility than that of the hydrate-bearing specimen. After being unloaded back to σ_v = 7 kPa, the void ratio rebounds slightly to e_f = 0.90, with a corresponding swelling index of C_s = 0.005.

The dry natural sediments start with a slightly lower initial void ratio e_o = 1.14 than that of the water-saturated specimen. The void ratio decreases to e = 0.86 when being loaded to σ_v = 25 MPa, and increases to e_f = 0.89 after being unloaded to σ_v = 7 kPa. The results suggest that water has negligible effects on the stress-volume responses of the tested natural sediments when compression occurs slowly enough for pore pressure to equilibrate in the water-saturated specimen.

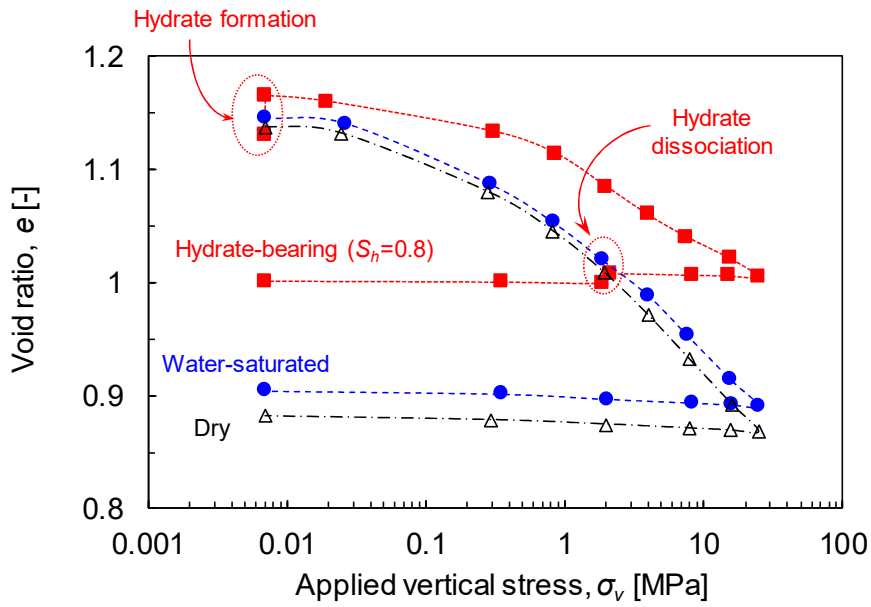

Figure 3.4 − Evolution of void ratio of the natural sediments tested at the following conditions: water-saturated hydrate-bearing (S_h = 0.8, red squares), water-saturated with no hydrate (S_h = 0, blue circles), and dry (black triangles). THF hydrate is formed at 7 kPa vertical stress and dissociated when the vertical stress is unloaded to 2 MPa.

3.3.2 Wave Velocities

Figure 3.5 compares the measured *P*- and *S*-wave velocity dependence on applied vertical stress for the three natural sediment specimen conditions: water saturated with THF hydrate (S_h = 0.8), water-saturated with no hydrate (S_h = 0), and dry. Natural sediments with S_h = 0.8 THF hydrate start with a *P*-wave velocity V_p = 2,422 m/s and s-wave velocity V_s = 1,217 m/s at σ_v = 7 kPa. Both velocities remain nearly unchanged during loading until the vertical effective stress reaches nearly σ_v = 1 MPa, then both velocities increase logarithmically with the vertical stress. The results highlight how the stiffness of hydrate-bearing sediments is mainly governed by the interconnected solid hydrate phase at low

stress but increases at high-stress conditions as the sediment skeleton consolidate (Figure 3.4) and contribute to the overall specimen stiffness. Unloading to the in situ vertical stress, σ_v = 2 MPa, does not cause a significant velocity decrease in either *P*- or *S*-waves, implying significant stress locking. THF hydrate dissociation to a fully-liquid phase at this stress decreases *P*-wave velocity from V_p = 3,817 m/s to 1646 m/s, in close agreement with the water-saturated, hydrate-free specimen at the same stress. The agreement is expected based on the similar void ratios between the two specimens at this condition (Figure 3.4), and the negligible effect liquid THF has on the stiffness of the interconnected water phase. The *S*-wave velocity drops from V_s = 1,887 m/s to an unknown value because no clear first arrival can be detected in the shear waveform after dissociation.

The *P*-wave velocity of the water-saturated natural sediments starts from V_p = 1,350 m/s at σ_v = 7 kPa, remains nearly unchanged until the vertical stress is loaded approximately to σ_v = 1 MPa, and then increases logarithmically with stress. The results show that, as with the THF hydrate case, the sediment's stiffness is dominated by the interconnected water phase at low stresses and enhanced due to increased skeleton stiffness at higher stresses. After unloading back to σ_v = 7 kPa, the *P*-wave velocity becomes V_p = ~1,693 m/s, which is higher than its initial velocity under the same vertical stress because of the unrecovered void ratio loss due to the loading at high stress. The interconnected water phase has no shear stiffness, however, so the *S*-wave velocity measures only the stiffness of the soil skeleton and, on a logarithmic scale, changes linearly with changes in the applied vertical stress. The *S*-wave velocity changes rapidly with vertical stress during loading in response to the increasing number of grain contacts and increasing horizontal stresses as particles become more interlocked during consolidation. The particle rearrangement during

consolidation is not reversible (Figure 3.4). For the given vertical stress, the number of grain contacts, the horizontal stresses between interlocked grains, and hence, the *S*-wave velocity, are all higher during unloading from the peak stress than during loading to the peak stress.

Both *P*- and *S*-wave velocities of the dry natural sediments increase logarithmically with stress starting immediately at 7 kPa, unlike for the hydrate or water-bearing cases, which had velocity plateaus until ~1 MPa. This is expected given the insignificant stiffness contribution from the interconnected air phase and the control of dry sediment stiffness mainly by stress. The V_s-logσ_v relation in the dry sediments is almost identical to that in water-saturated sediments, reflecting the lack of shear stiffness in both interconnected phases. The slight offset between the dry and water-saturated curves can be related to the higher density of water relative to air. The *P*- and *S*-wave velocities change more rapidly with applied vertical stress during loading than unloading, indicating the elevated contact numbers and the stress locked within jammed particles in the dry sediments during loading is mostly retained during unloading. The stiffness of this sandy silt core is affected by stress history.

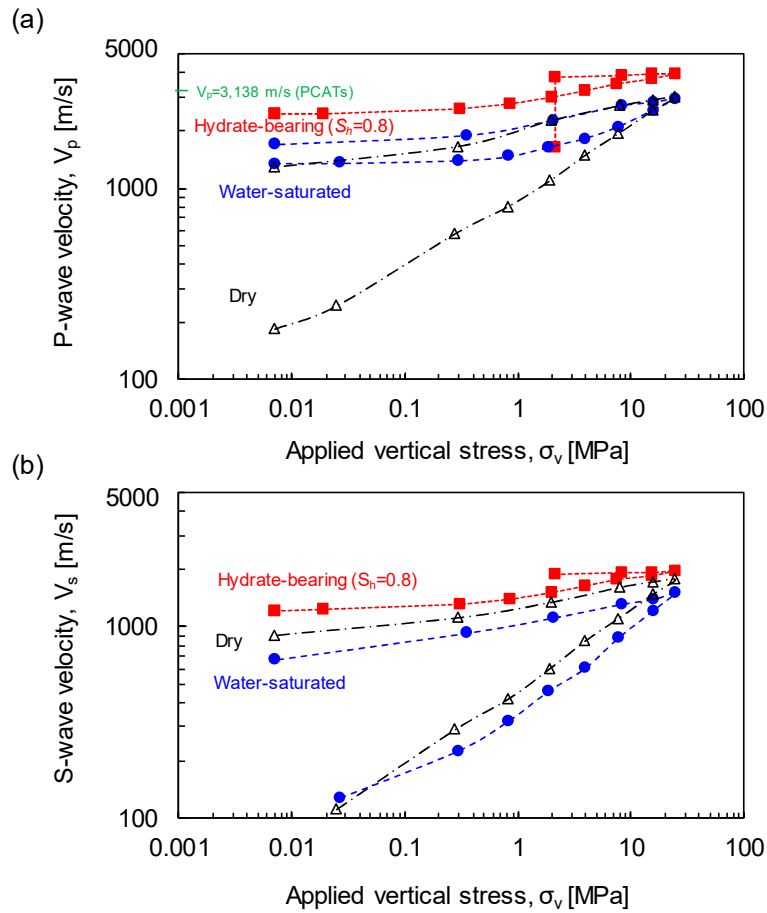

Figure 3.5 − *P*- and *S*-wave velocities of the natural sediments tested at the following conditions: water-saturated hydrate-bearing (S_h = 0.8, red squares), water-saturated with no hydrate (S_h = 0, blue circles), and dry (black triangles). THF hydrate is formed at 7 kPa vertical stress and dissociated when the vertical stress is unloaded to 2 MPa. (a) *P*-wave velocities. The original pressure core subsection had an averaged *P*-wave velocity of 3,138 m/s under no effective stress. (b) *S*-wave velocities.

3.4 Analyses and Discussion

3.4.1 The Poisson's Ratio of Hydrate-Bearing Sediments

With simultaneous measurements of *P*- and *S*-wave velocities, one can compute the sediment's Poisson's ratio as:

$$\upsilon = \frac{\left(V_P/V_s\right)^2 - 2}{2\left(V_P/V_s\right)^2 - 2} \tag{3-1}$$

The computed Poisson's ratio of the natural sediments tested with their three different pore-space components during loading and unloading is shown in Figure 3.6a.

The Poisson's ratio of the sediments with an interconnected hydrate phase (S_h = 0.8) at the initial applied vertical stress of 7 kPa has v = 0.33, identical to that of pure THF hydrate crystals (Bathe et al., 1984), suggesting the Poisson's ratio is initially controlled by the interconnected hydrate phase. As the stress increases to σ_v = 25 MPa, the Poisson's ratio increases only slightly to v = 0.34. The Poisson's ratio of the water-saturated natural sediments starts at low vertical stress with v = 0.49, nearly identical to that of water, suggesting the elastic behavior of the system is governed by the interconnected water phase. With increasing stress, however, the Poisson's ratio gradually decreases to v = 0.32 at σ_v = 25 MPa. The elastic properties of this water-saturated sediment system become more affected by the sediment skeleton due to increased skeleton stiffness as the void ratio is reduced at high stress (Figure 3.4). The Poisson's ratio of the dry sediments starts from v = 0.37 at σ_v = 7 kPa, decreasing to v = 0.24 at σ_v = 25 MPa, indicating the insignificant stiffness contribution from the interconnected gas phase, and how the void ratio decrease allows the skeletal stiffness to approach that of pure quartz. Unloading causes minute changes in the Poisson's ratio of the sediments in all three pore-content conditions. This result also suggests the high applied stress caused stress locking within the sediments, and that the elastic properties of such sediments are affected by stress history.

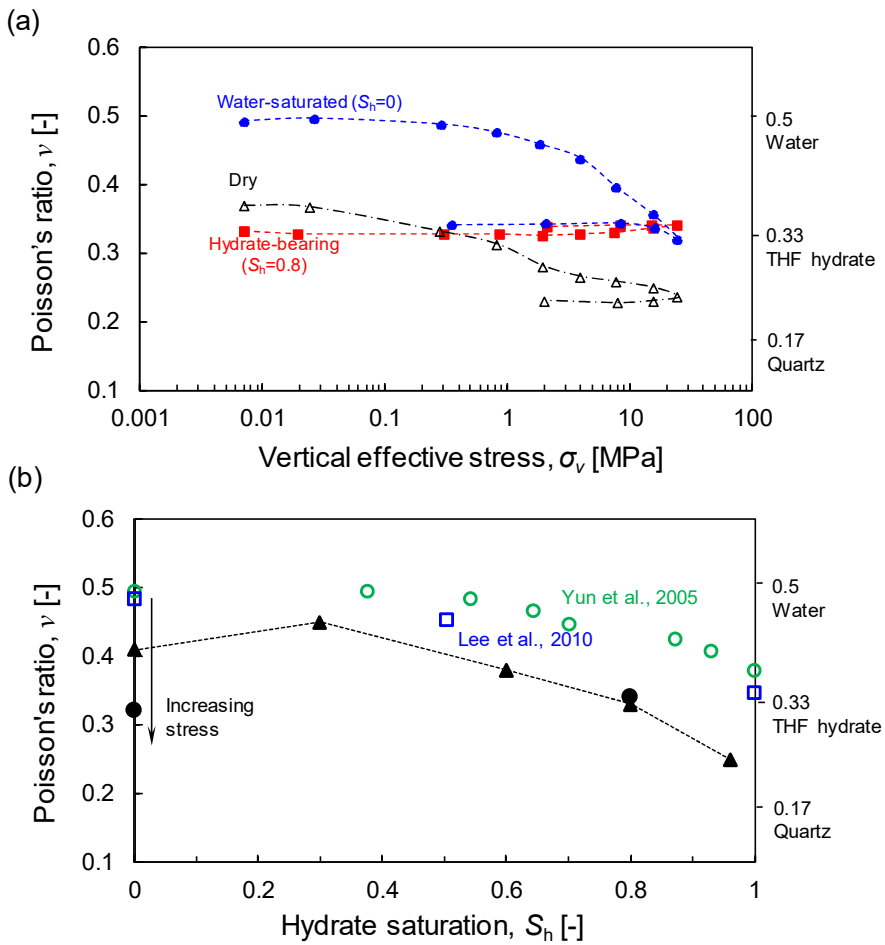

Figure 3.6 − Calculated Poisson's ratio from *P*- and *S*-wave measurements. (a) The Poisson's ratio of natural sediments in their hydrate-bearing (S_h = 0.8), water-saturated (S_h = 0), and dry conditions in response to vertical loading and unloading. (b) Poisson's ratio for natural sediments in comparison to F110 fine quartz sand versus hydrate saturation at low stress (open markers from Yun et al. (2005) and Lee et al. (2010a)) and high vertical stresses (solid symbols, this work). Literature data are results of hydrate-bearing F110 fine sands subjected to nominal stress. High-stress data from this study include hydrate-bearing F110 fine sands (solid triangles) and natural sediments (solid circles) at a vertical stress σ_v = 25 MPa.

The low-stress, pre-loading Poisson's ratio relationships between sediments with different pore-filling materials are consistent with published data. Poisson's ratio of water-saturated hydrate-bearing F110 fine sands decreases from ν = 0.49 to ν = ~0.33 with

increasing hydrate saturation from $S_h = 0$ to $S_h = \sim 1$ at relatively low stresses (Figure 3.6b). In water-saturated sediments, the Poisson's ratio ranges between that of water at low stress, to that of the quartz mineral at high stress. For the hydrate-bearing F110 fine quartz sand tested to high stresses in this study, the Poisson's ratio ranges between that of THF hydrate at low stress and that of pure quartz at high stress. These data suggest at low stress (< 2 MPa) Poisson's ratio in sandy sediments is mainly governed by the Poisson's ratio of the pore-filling phase. At high stress (i.e., $\sigma_v = 25$ MPa in this study), however, the soil skeleton stiffness can be comparable to the stiffness of the pore-filling phase (i.e., water, hydrate, or water and hydrate mixture), and the bulk Poisson's ratio is influenced by the elastic properties of both the skeleton and the pore-filling phase.

3.4.2 Compressibility

When the loading exceeds the sediment's in situ stress (~1.6 MPa based on LWD density log), the consolidation curve for the THF hydrate-bearing sediments fails to follow a constant compression index C_c line and instead trends with a convex-downward shape (Figure 3.7). This trend is due, at least in part, to a transition from the specimen consolidating by eliminating water-filled pore space to consolidating by compressing the solid sediment and hydrate phases. This has also been observed by Yoneda et al. (Yoneda et al., 2019b) for sediment from this Area B anticline crest hydrate reservoir. Additionally, sediment grain crushing could further restrict particle rearrangement and inhibit consolidation.

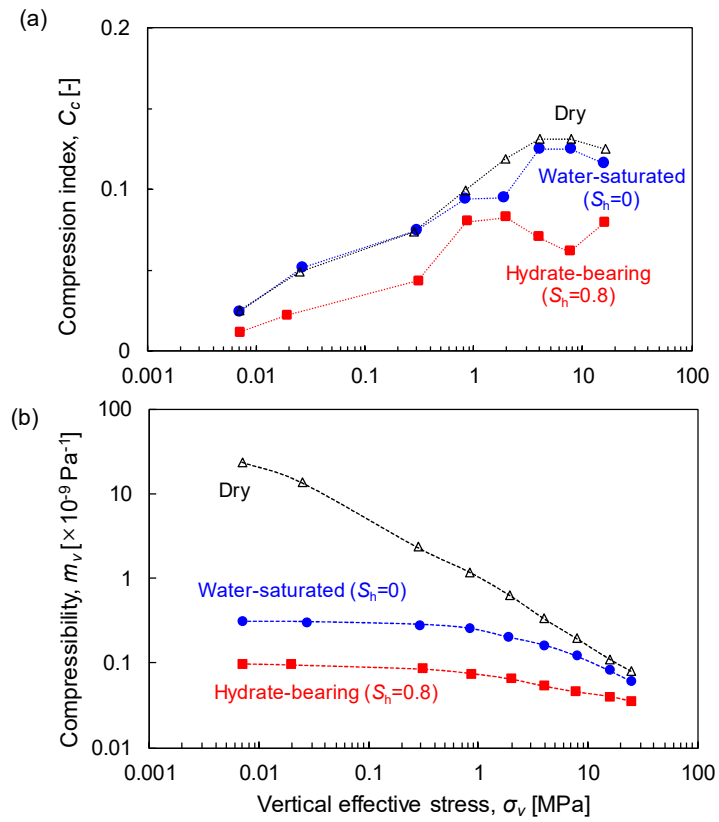

Figure 3.7 − Stress dependent compressibility of the natural sediments. (a) The evolution of the compression index C_c with increasing stress. (b) The pore compressibility m_v with increasing stress.

The compression index C_c is defined as the void ratio change over the logarithmical stress change:

$$C_c = \frac{\Delta e}{\Delta \log \sigma} \tag{3-2}$$

Additionally, pore compressibility m_v is defined as the change in volumetric strain over the stress change ($\Delta\varepsilon_v/\Delta\sigma$), which is also the inverse of the constraint modulus M, which can be accurately determined based on measured P-wave velocity V_p at each stress:

$$m_v = \frac{1}{M} = \frac{1}{\rho V_p^2} \tag{3-3}$$

where ρ is the specimen bulk density, calculated from the density and volume fraction of each phase (i.e., grain, water, and hydrate). Computed compression index C_c and pore compressibility m_v values are shown in Figure 3.7.

Results show C_c is smaller for hydrate-bearing sediments than for hydrate-free sediments. The compression index of the hydrate-free sediments increases with stress and eventually reaching a plateau. The compression index of the hydrate-bearing sediments reaches a peak value at a lower stress than the hydrate-free case, then begins to decrease with additional stress increases, indicating the system possibly undergoes a transition from compressing water-filled voids to compressing the solid sediment and hydrate phases, eventually reaching a nearly constant compression index value. The corresponding pore compressibility (in $\times 10^{-9}$ Pa^{-1}) of hydrate-bearing and hydrate-free sediments results show that compressibility decreases exponentially with increasing stress, and a hydrate saturation of $S_h = 0.8$ can reduce the sediment's pore compressibility by about half relative to hydrate-free, water-saturate sediment. The dry and water-saturated compressibility reflects the volumetric strain change in sediments under drained and undrained loading conditions, respectively.

3.4.3 Sand Crushing Effect

In order to quantify the effects of hydrates on particle crushing, the relative particle breakage index B_r is calculated (Einav, 2007a, Hardin, 1985):

$$B_r = \frac{B_t}{B_p} \tag{3-4}$$

where B_t is the area between the initial and post-crushing grain size distribution curves. B_p denotes the area between the initial grain size distribution and the ultimate gradation U_g (i.e., the ultimate grain size distribution):

$$U_g = \left(\frac{d}{d_{\max}} \right)^{3-\alpha} \tag{3-5}$$

where d represents the particle size, d_{max} is the maximum particle size of the initial distribution, and α is a fractal dimension and suggested to be α = 2.6 for sands (Einav, 2007a). Higher breakage index values reflect more pronounced and extensive sand crushing.

Figure 3.8a presents the grain size distributions for the initial, post maximum loading of 25 MPa, and ultimate grain size cases for the natural specimens, together with the breakage index B_r values as a function of hydrate saturation S_h. Note that it is the effective stress governing the sand crushing. Pressure coring and pressure core depressurization most likely will not cause a significant increase in effective stress, and thus these processes will not cause evident sand crushing before the specimen being tested in this study. Complementary tests using hydrate-bearing F110 fine sands with various hydrate saturations S_h = 0, 0.3, 0.6, and 0.96 were also run to a maximum vertical stress of 25 MPa (Figure 3.8b). The calculated breakage index B_r results from both the natural and the F110

sands specimens suggest the presence of gas hydrate in sediments can mitigate particle crushing at high stress. This decreased extent of sand crushing with increasing hydrate saturation highlights that the loss of gas hydrate due to dissociation during gas production can aggravate particle crushing.

Particle breakage or crushing can initially decrease soil skeleton stiffness if the crushed particles are easily rearranged into the surrounding pore volume. When post-crushing particle rearrangement hinders inter-particle slip and rotation, however, the bulk stiffness increases (Mesri and Vardhanabhuti, 2009). The presence of an interconnected hydrate phase in the pore space can reduce the load supported by sediment grains and will also interfere with sediment grain rearrangement.

Figure 3.9 shows an array of microscopic images of F110 fine (d_{50} = 120 μm) and Ottawa 20/30 coarse sands (d_{50} = 720 μm) after they experienced various maximum vertical stresses σ_{max} = 0, 25, 50, 75, and 100 MPa in the oedometer cell. The results highlight the effects of particle size and maximum stress on sand crushing. More severe sand crushing is observed when larger particles are subjected to higher stresses. Crushed particles tend to be more angular in shape. Sand crushing causes volumetric contraction and generates fine particles more susceptible to migration during gas production (Dai et al., 2011). Pronounced particle crushing occurs in sediments that are poorly-graded, larger in size, more angular, and with higher void ratios (Lee and Farhoomand, 1967, Lade et al., 1996, McDowel and Bolton, 1998, Nakata et al., 2005, Hardin, 1985, Billam, 1972). Crushing of quartz sands starts at ~4 MPa stress and massive grain crushing is estimated to begin between 10-20 MPa (Lo and Roy, 1973, McDowell, 1999, Nakata et al., 2001), within the

~25 MPa range of effective stress proposed for methane extraction from the Area B anticline crest has hydrate reservoir (Boswell et al., 2018, Myshakin et al., 2019). Effective stress as high as 100 MPa will not occur across the whole reservoir during gas production. However, localized stress concentration, such as near the wellbore screen during gas production or at the tip of a cone penetration test, can happen and cause localized particle crushing.

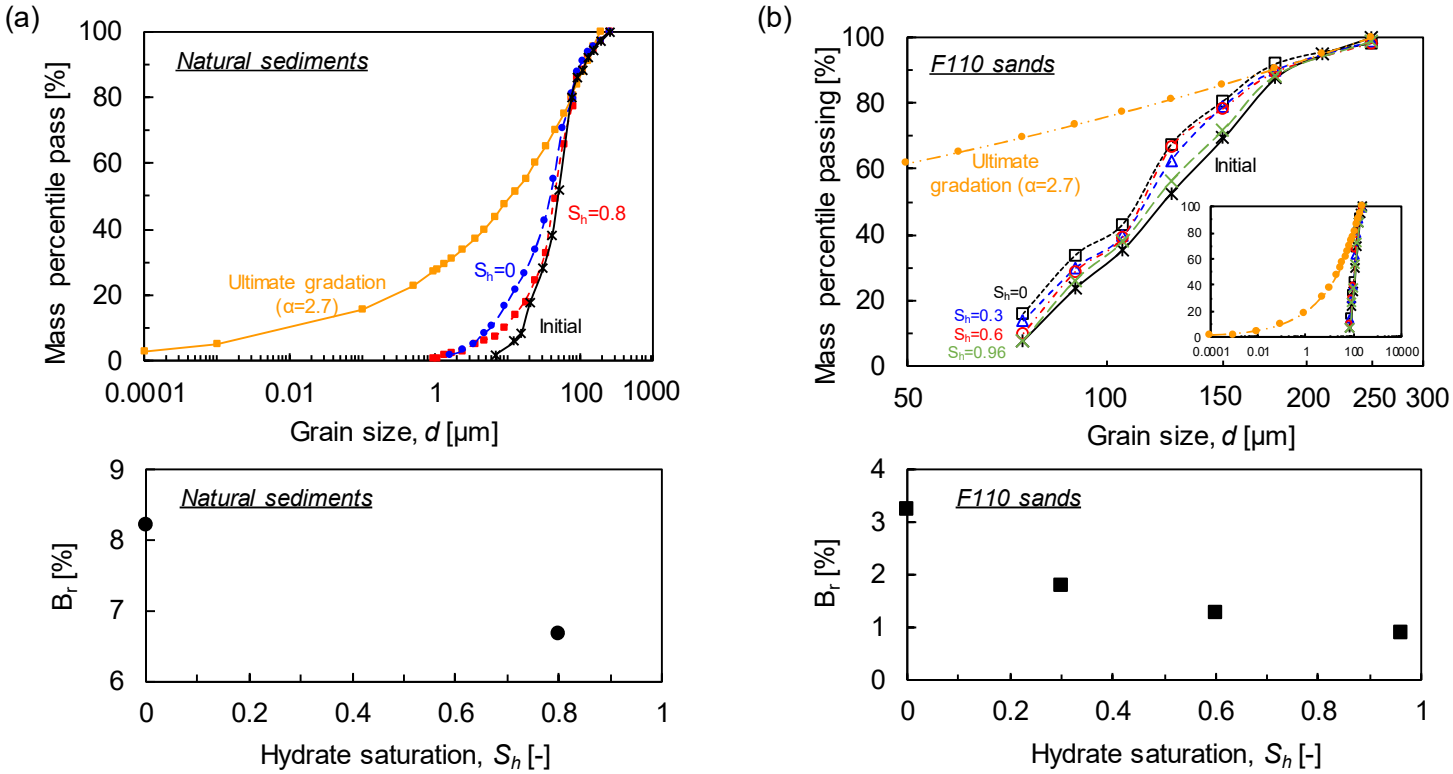

Figure 3.8 − Particle crushing in hydrate-bearing sediments. (a) The grain size distributions of the initial, post-crushing, and ultimate gradation of natural sediments with and without THF hydrate (S_h = 0.8 and 0, respectively). The maximum vertical load is 25 MPa. (b) Complementary results obtained using F110 fine sands with various THF hydrate saturation.

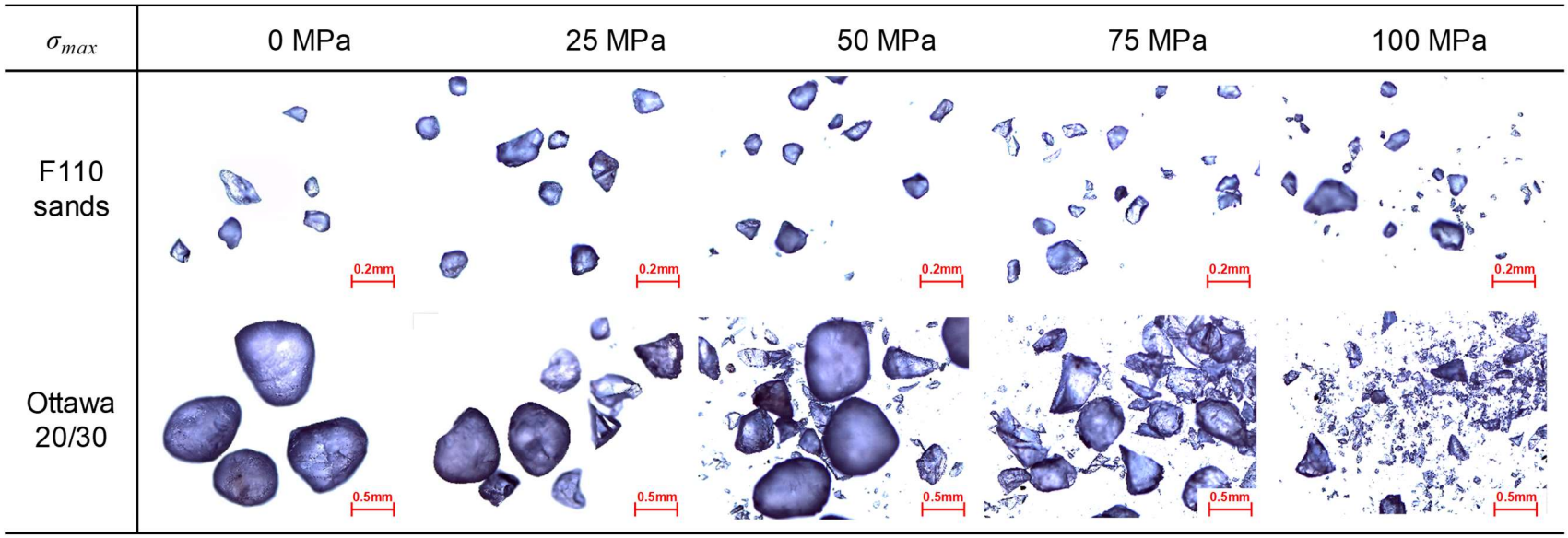

Figure 3.9 – Microscopic images of F110 fine sand (d_{50} = 120 µm) and Ottawa 20/30 coarse sands (d_{50} = 720 µm) after experiencing different levels of maximum vertical stresses σ_{max} = 0, 25, 50, 75, and 100 MPa.

3.5 Conclusions

This study investigates the physical and geomechanical properties of natural sediments subjected to effective stresses up to 25 MPa, with a focus on stiffness, compressibility, and sand crushing. Complementary tests using laboratory standard quartz sands, F110 fine sands and Ottawa 20/30 coarse sands, provide a framework for understanding the NGHP-02 sediment laboratory results. Experimental results show that:

- In addition to inducing a void ratio reduction, loading can lock stress inside the sediments, where a significant portion remains even during unloading. Thus, the stiffness of the sandy silt specimens tested here is affected by stress history. At high stresses, the stiffness of hydrate-free sediments is mainly governed by the stress state on the sediment skeleton, while the stiffness of hydrate-bearing sediments reflects both the grain supporting nature of the interconnected hydrate phase and stress effects on the sediment skeleton.

- The Poisson's ratio of sediments is dominated by stiff components. At low stress, the sediment's Poisson's ratio is dominated by the Poisson's ratio of the pore-filling phases, i.e., water and/or hydrate. At high stress, the sediment's skeleton develops a stiffness that is comparable to the water or hydrate phase stiffness, and thus the bulk Poisson's ratio captures the elastic properties of both the skeleton and the pore-occupying phases.

- The water-filled reservoir sediment from Site NGHP-02-23 in Area B consolidates with a constant compression index, C_c for stresses above the pre-consolidation

stress. When the sediment has a hydrate saturation of 0.8, however, C_c decreases with increasing stress above 4 MPa. This difference highlights how C_c is influenced by compressing hydrate and sediment grains rather than only compressing water-filled void space. Grain motion restrictions due to particle crushing may also reduce C_c at high effective stress.

- The pore compressibility, m_v, (in $\times 10^{-9}$ Pa^{-1}) of hydrate-bearing and hydrate-free sediments decreases exponentially with increasing stress, and hydrate saturation S_h = 0.8 can reduce the sediment's compressibility by about a factor of two.

- The particle breakage index B_r decreases with increasing hydrate saturation S_h. Results suggest the presence of gas hydrate in sediments can mitigate particle crushing by supporting a portion of the load that would otherwise have to be carried by the sediment grains and can interfere the particle rearrangement of the post-crushing particles.

- Extracting methane by depressurizing gas hydrate deposits decreases gas hydrate saturation, increases effective stress, and this combination can cause particle crushing, even for less than the ~25 MPa effective stress suggested for depressurizing this hydrate reservoir to extract the methane as an energy resource. More severe crushing is expected in larger particles with less hydrate subjected to higher stresses.

CHAPTER 4 THE COEFFICIENT OF EARTH PRESSURE AT REST IN HYDRATE-BEARING SEDIMENTS

4.1 Introduction

The coefficient of earth pressure at rest K_0 describes the ratio of the vertical to the lateral stresses at zero lateral strain conditions, as expressed below:

$$K_0 = \frac{\sigma'_l}{\sigma'_v} \tag{4-1}$$

where σ'_v and σ'_l are the vertical and lateral effective stresses. Since the value of K_0 indicates the in situ stress state of natural soil deposits, the stress ratio is an essential factor in understanding soil deposit behavior, such as stress transfer and stability analysis. The value of K_0 in soils can be influenced by the effective stress, stress history, the over-consolidation ratio (OCR), cementation bonding and debonding, packing density, and particle shape and size (Andrawes and El-Sohby, 1973, Yun and Evans, 2011, Brooker and Ireland, 1965, Zhu et al., 1995, Kumar et al., 2019, Wanatowski and Chu, 2007).

For non-cemented soils, the values of K_0 does not change significantly during loading, i.e., the lateral stress increases linearly with the increase in vertical stress. However, the K_o increases during unloading due to the increased OCR and enhanced interlocked soil skeleton (Mayne and Kulhawy, 1982, Okochi and Tatsuoka, 1984, Brooker and Ireland, 1965, Yun and Evans, 2011). The response of the K_0 of cemented soils to vertical stress changes is different from that of the non-cemented soils. For cemented soils, the values of K_0 are mainly governed by the cementation effects among particles during loading, leading

to lower K_0 values at low strain conditions (Yun and Evans, 2011, Lee et al., 2016). After cementation bonding is broken at higher strain and/or stress, the lateral stress response is controlled by the applied vertical stress and soil skeleton (Zhu et al., 1995, Yun and Evans, 2011). Therefore, the relation between the lateral stress and the vertical stress of the cemented soils is non-linear. This behavior is mainly controlled by the degree of cementation bonding and debonding, stress history, and specimen packing density and fabric (Yun and Evans, 2011, Andrawes and El-Sohby, 1973, Brooker and Ireland, 1965, Zhu et al., 1995, Northcutt and Wijewickreme, 2013).

The hydrate crystals in the sediment pore spaces can play an essential role in the stress-strain relation, strength, stiffness, permeability, and volume changes of hydrate-bearing sediments (Yun et al., 2005, Yoneda et al., 2019a, Waite et al., 2009, Dai et al., 2019, Lee et al., 2010a). For example, hydrate formation causes an increase in the stiffness of sediments due to cementation, and hydrate dissociation decreases the stiffness (Yun et al., 2007, Hyodo et al., 2017, Clayton et al., 2010, Priest et al., 2005, Lee et al., 2010a). Especially, the increased effective stress caused by the depressurization for gas production in deep-sea hydrate deposits can induce significant changes in the K_0 of hydrate-bearing sediments. Therefore, it is essential to understand the affecting factors of the values of K_0 in hydrate-bearing sediments. This study specifically investigates the impacts of hydrate saturation S_h and vertical stress σ'_v on the K_0 of hydrate-bearing sediments.

The purpose of this experimental study is to evaluate the evolution of the coefficient of earth pressure at rest K_0 in tetrahydrofuran (THF) hydrate-bearing sediments. The lateral stress response of hydrate-bearing sediments is experimentally investigated under various

vertical stress levels (from low to sufficiently high for sand particle crushing) considering hydrate formation and dissociation.

4.2 Experimental Study

4.2.1 Experimental Setup

An instrumented thick-wall oedometer cell (illustrated in Figure 4.1) is designed to measure the lateral stress in tested specimens under various vertical stress up to σ_v = 25 MPa. The inner diameter of the thick-wall cell is 50.8 mm, and the thickness of the wall is 50.8 mm. The oedometer cell is satisfactory to sustain lateral stress up to 24 MPa with the lateral strain level of $\varepsilon_r \leq 10^{-5}$. At the middle height of the specimen, a diaphragm pressure transducer (Omega PX61V0) is installed to monitor the lateral stress. Porous bronze disks are embedded on pedestals to allow uniform draining of pore fluid.

The applied vertical stress is controlled by using a hydraulic pump with a stiff reaction frame for high vertical stress (1 MPa < σ_v < 25 MPa) and by a Terraload consolidation loading device (S-450, Durham Geo Slope Indicator) for low levels of vertical stress (0.05 MPa < σ_v < 1 MPa). During the test, the vertical displacement is measured by a linear variable differential transformer (LVDT). The entire oedometer system is placed in a walk-in freezer to control the experimental temperature (i.e., 0.1°C-20°C) with an accuracy of 0.1°C.

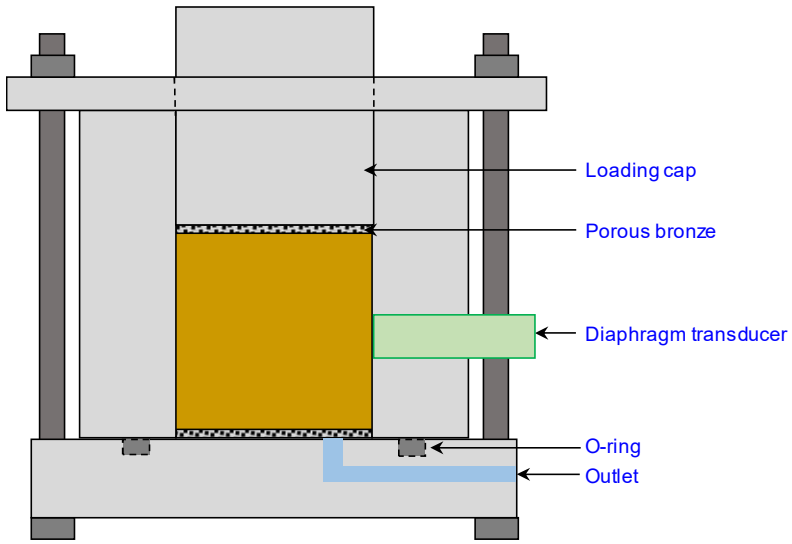

Figure 4.1 – A schematic drawing of the instrumented oedometer cell for lateral stress measurement.

4.2.2 Experimental Procedures

F110 fine sand (maximum void ratio e_{max} = 0.85, minimum void ratio e_{min} = 0.54, mean particle size d_{50} = 720 μm, and uniformity coefficient C_u = 1.21) is used in this experimental study. Specimens are prepared with a relative density of 40% and a corresponding void ratio of 0.726. The ratio of specimen height and diameter (*H/D*) is limited to 0.6 to avoid the effects of top and bottom boundary conditions for the lateral stress measurement (Shin and Santamarina, 2009). The sand is mixed with a predetermined mass ratio of THF:H_20 solution to achieve the targeted THF hydrate saturation. The THF:H_20 solution is prepared using the excess water condition, indicating pore space would be filled with the remaining water after hydrate formation. The mass ratios of THF:H_2O are 0:100, 9.8:90.2, 14.3:85.7, and 20.3:79.7, corresponding to hydrate saturation S_h = 0, 0.3, 0.6, and 0.96, respectively (Strauch et al., 2018).

After preparing and packing the specimens with the targeted hydrate saturation, the temperature is lowered to 0.1°C to trigger hydrate formation. The set temperature is kept constant for more than 24 hours after the hydrate nucleation to confirm that the hydrate formation process is completed. Note that the applied vertical stress during the hydrate formation is 0.025 MPa, caused by the self-weight of the top cap of the oedometer cell. After completing hydrate formation, additional vertical stress is applied step-by-step up to 25 MPa. At each loading step, the applied vertical stress is kept constant until both vertical and lateral stress is stabilized. Then, the applied vertical stress is lowered to 0.025 MPa. Lastly, the freezer temperature is set to 10°C to induce the hydrate dissociation.

In order to explore the effects of applied vertical stress during hydrate formation and dissociation on the lateral stress response, three additional specimens are prepared with various hydrate saturation levels (S_h = 0.3, 0.6, and 0.96) as complementary tests. These specimens are subjected to 25 MPa vertical stress first, followed by hydrate formation and dissociation. And lastly, the applied vertical stress is unloaded to 0.025 MPa.

4.2.3 Experimental Results

Figure 4.2 presents the measured temperature, vertical and lateral stresses, and the calculated coefficient of earth pressure at rest K_0 of the S_h = 0.96 specimen. This specimen experienced hydrate formation first under 0.025 MPa, loading up to 25 MPa followed by unloading, and finally hydrate dissociation. Once hydrate crystals start to nucleate, accompanied by a specimen temperature spike, the K_0 suddenly increases from 0.7 to 1.3. With further hydrate crystal nucleation and growth, the K_0 decreases and recovers to 0.7, which is close to the initial K_0 value before hydrate formation. After completing the hydrate

formation, vertical stress is applied to the specimen. At the moment of increasing vertical stress, the K_0 instantaneously drops to 0.05 and then recovers to 0.46 with the followed loading steps up to 25 MPa. The following unloading to 0.025 MPa causes an increase in K_0, and the values are finalized to 13.3 under 0.025 MPa vertical stress. Even though the vertical stress is constant during each the unloading step, the lateral stress is continuously decreasing with elapsed time, resulting in time-dependent changes in K_0. At the moment of the applied vertical stress is unloaded to 0.025 MPa, the value of K_0 peaks to 104.6 and then decreases and stabilizes at 13.3. During hydrate dissociation, a sudden decrease of K_0 is observed, and the values remain constant at 3.4 after the hydrate dissociation is completed.

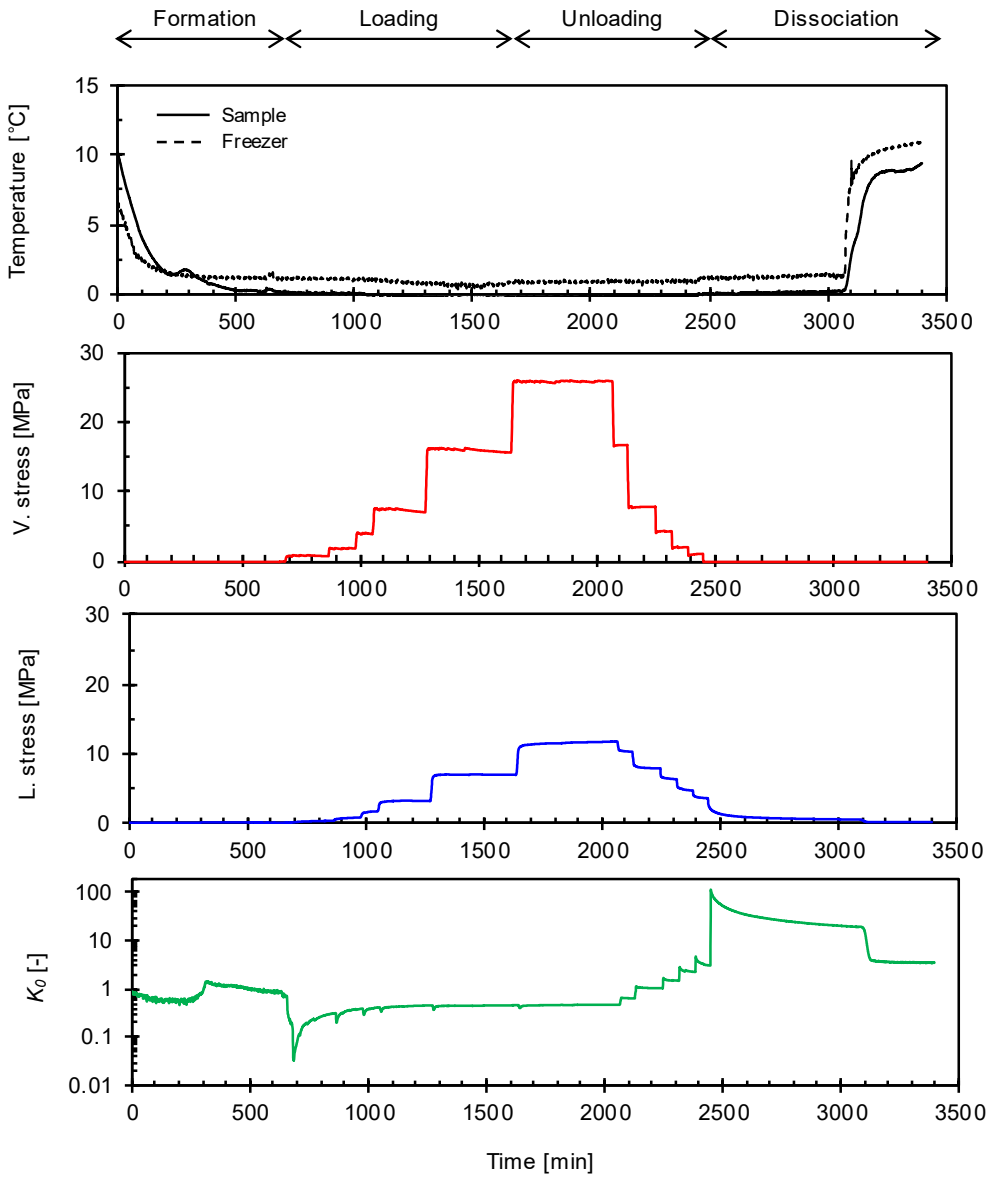

Figure 4.2 – Evolution of measured parameters (i.e., temperature, vertical and lateral stresses, and coefficient of earth pressure at rest K_0) for the S_h = 0.96 specimen. The specimen is experienced the hydrate formation under 0.025 MPa vertical stress, and then subjected to loading up to 25 MPa. After complete unloading back to 0.025 MPa, the hydrate dissociation is conducted.

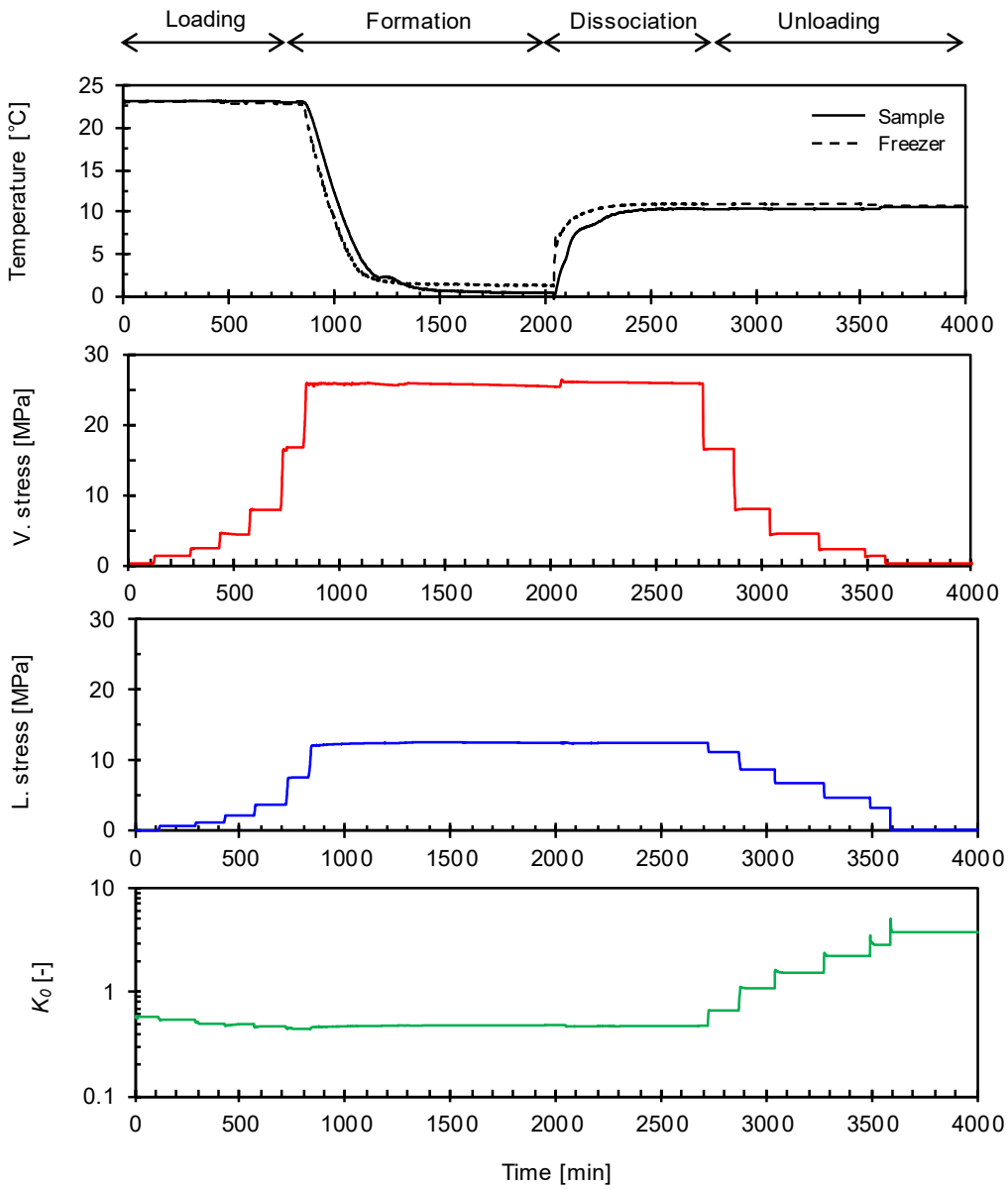

Figure 4.3 − Evolution of measured parameters for S_h = 0.96 Specimen. The specimen is subjected to 25 MPa vertical stress first, and then experienced the hydrate formation and dissociation processes with following unloading process.

Figure 4.3 shows the evolution of measured parameters for a specimen which is first subjected to 25 MPa vertical stress and then experienced hydrate formation and dissociation with the following unloading to 0.025 MPa. The K_0 of the hydrate-free specimen is 0.58 under 0.025 MPa and decreases to 0.45 as the vertical stress increases up to 25 MPa. Unlike the hydrate-bearing sediment shown in Figure 4.2, the loading process of hydrate-free sediment does not show a sudden reduction of K_0 and a time-delayed response to the lateral stress. During hydrate formation (cooling) and dissociation (warming) under 25 MPa vertical stress, no distinguishable change in K_0 is observed. The unloading process induces an increase in K_0 and finalizes to 3.8 under 0.025 MPa.

4.3 Experimental Results and Analyses

4.3.1 Effects of Hydrate Formation on Lateral Stress

The evolution of temperature and K_0 during hydrate formation in various hydrate-bearing sediments (S_h = 0, 0.3, 0.6, and 0.96) under 0.025 MPa vertical stress are summarized in Figure 4.4a. Hydrate nucleation occurs when the temperature is below 4.4°C for the S_h = 0.96 specimen. The values of K_0 of all specimens before hydrate formation are 0.65–0.75. Note that all specimens are saturated by the THF-H_2O mixture. As the temperature decreases to enable hydrate formation, specimens with relatively lower hydrate saturation (i.e., S_h = 0.3 and 0.6) have no observable changes in K_0, but the S_h = 0.96 specimen shows a sudden increase in K_0 from 0.65 to 1.3 when hydrate nucleation starts and then continuously decreases to the initial K_0. At the moment of hydrate nucleation, the K_0 increases due to the increase in lateral stress, but K_0 recover to the initial values as time progresses with further hydrate nucleation and growth. Consequently, the values of

K_0 before and after hydrate formation have no significant differences regardless of hydrate saturation, even though the specimen with S_h = 0.96 has a sudden increased lateral stress history. During hydrate formation, the specimens have only internal hydrate crystallization forces between particles and formed hydrate crystals under constant vertical stress of 0.025 MPa.

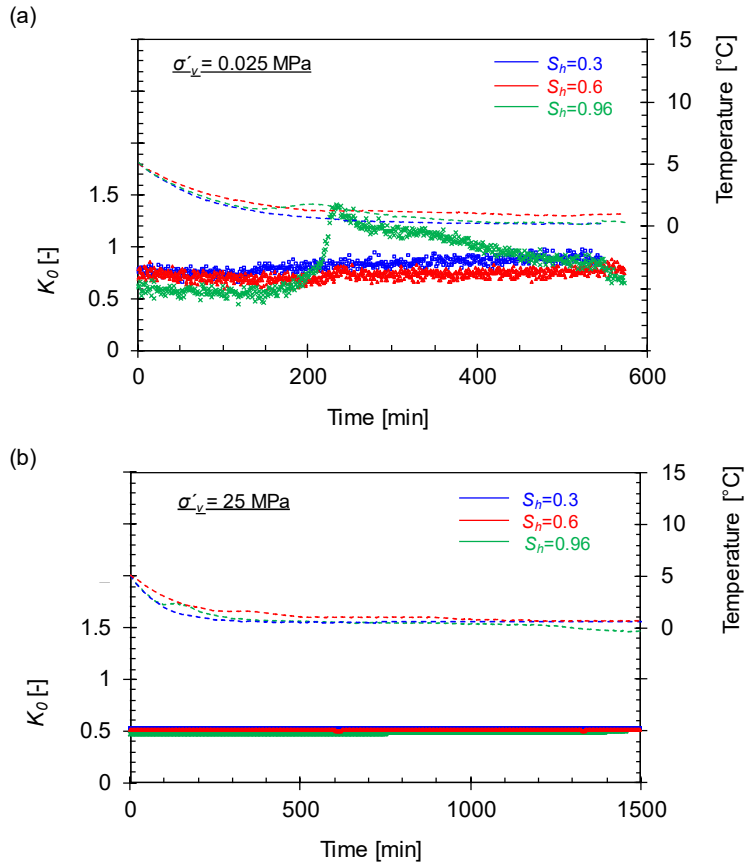

Figure 4.4 − Evolution of the coefficient of earth pressure K_0 and specimen temperature during hydrate formation. Dashed colored lines indicate the measured temperature of the specimens during cooling. (a) Hydrate formation under 0.025 MPa vertical stress. (b) Hydrate formation under 25 MPa vertical stress.

In Figure 4.4b, the evolution of K_0 during hydrate formation under the higher vertical

stress (σ_v = 25 MPa) is shown to illustrate the effects of applied vertical stress on K_0. No observable changes in K_0 are detected for all the hydrate-bearing specimens during hydrate formation. Compared with the stress conditions before the hydrate formation (i.e., 25 MPa vertical stress and 12.5 MPa lateral stress with measured K_0 = 0.5), the hydrate crystallization stress in pore spaces might be negligible to affect the specimen's stresses ratio.

4.3.2 Effects of Loading on Lateral Stress of Hydrate-Bearing Sediments

After completing hydrate formation at σ_v = 0.025 MPa, the hydrate-bearing specimens are subjected to additional vertical stress steps up to 25 MPa, and the corresponding responses of the lateral stress are monitored. The evolution of K_0 of hydrate-bearing specimens (i.e., S_h = 0, 0.3, 0.6, and 0.96) as a function of the applied vertical stress is plotted in Figure 4.5, and changes in stresses and K_0 with elapsed time are presented in Figure 4.6.

For the S_h = 0 (water-saturated) specimen, indicated by black circle markers in Figure 4.5, K_0 slightly decreases with an increase of applied vertical stress in the intermediate stress range (σ_v < 10 MPa). Since there is no hydrate present, the stress transfer from the vertical to lateral direction is mainly governed by the soil skeleton. The minor decrease in the value of K_0 can be attributed to the compaction effect caused by increased vertical stress. At the higher vertical stress region (10 MPa < σ_v < 25 MPa), K_0 shows no further reduction and remains nearly constant at 0.5. The response of K_0 of the S_h = 0.3 specimen is similar to that of the S_h = 0 specimen, indicating that lower hydrate saturation (S_h < 0.3) in the pore space has no significant effects on the value of K_0 during loading.

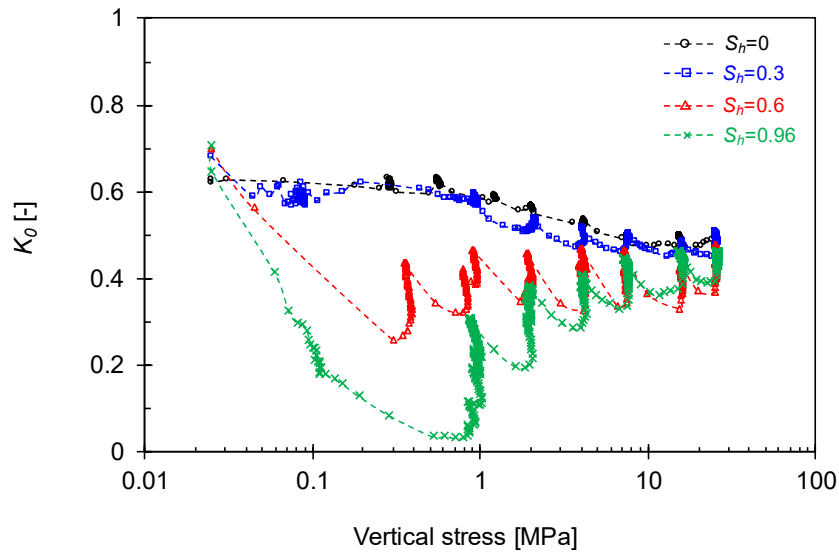

Figure 4.5 − Changes in the coefficient of earth pressure at rest K_0 of various hydrate-bearing specimens (S_h = 0, 0.3, 0.6, and 0.96) during loading. The loading process starts from 0.025 MPa and up to 25 MPa after complete the hydrate formation.

The specimens with high hydrate saturation (i.e., S_h = 0.6 and 0.96) show a significant reduction of K_0 at the low vertical stress level (σ_v < 1 MPa) as shown in Figure 4.5 and Figure 4.6, and this phenomenon is more pronounced in the higher saturated specimen. The decrease in K_0 during loading means that the stress transfer from the vertical to the lateral direction weakens. In the range of applied vertical stress from 1 MPa to 10 MPa, the K_0 suddenly decreases at the moment of increasing vertical stress and then rises again under the constant vertical stress. The higher saturated specimens have a more pronounced recovery of K_0 under constant vertical stress. Even though S_h = 0.6 and S_h = 0.96 specimens show the different history of K_0 (i.e., reduction and recovering) during loading, the values of K_0 converge to about 0.45-0.51 which is similar values of hydrate-free (S_h = 0) and S_h = 0.3 specimens under 25 MPa vertical stress.

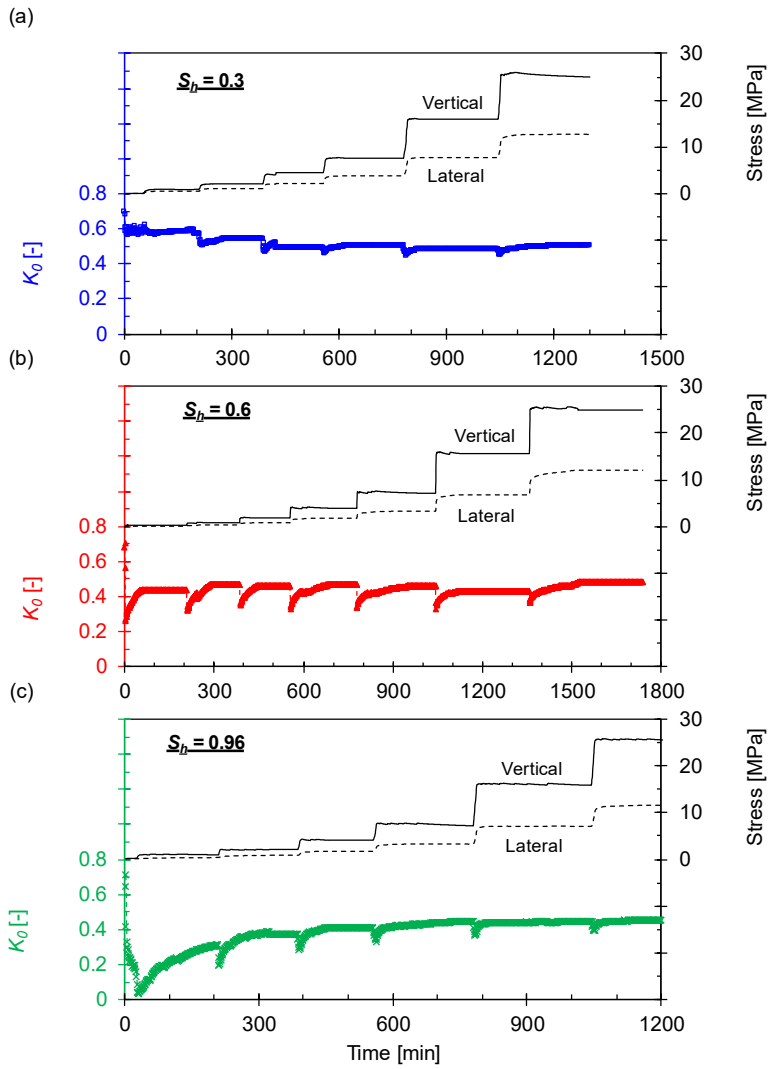

Figure 4.6 − Evolution of the coefficient of earth pressure at rest K_0 and stresses with the elapsed time during loading. (a) S_h = 0.3. (b) S_h = 0.6. (c) S_h = 0.96.

The following mechanism can be adapted to explain these phenomena, which are affected by the applied vertical stress and hydrate saturation levels.

Effects of cementation bonding (σ_v < 1 MPa): The presence of hydrate crystals in pore spaces can enhance the strength and stiffness of hydrate-bearing sediments; more pronounced effects are expected in higher hydrate-saturated specimens (Yun et al., 2005,

Yoneda et al., 2016, Lee et al., 2010a, Yun et al., 2007, Hyodo et al., 2016). The reduction of K_0-values under the low applied vertical stress ($\sigma_v < 1$ MPa), especially for the specimens with higher hydrate saturation (i.e., $S_h = 0.6$ and 0.96 in this study), may be caused by the enhanced strength and stiffness of the specimen (i.e., the cementation bonding effect between soil particles and hydrate crystals). Cementation effects can cause the less pronounced lateral stress transmission of the applied vertical stress because cementation can support and share the applied vertical stress (Yun and Evans, 2011, Yun and Santamarina, 2005, Zhu et al., 1995). As the applied vertical stress increases ($\sigma_v > 1$ MPa), the cementation bonding effect is reduced due to the breaking of cementation bonding among particles (Zhu et al., 1995, Lee et al., 2016, Yun and Evans, 2011). Higher stress is required to initiate cementation debonding for higher hydrate-saturated specimens.

<u>Effects of creep (time-dependent) behavior of hydrate crystals (1 MPa < σ_v < 25 MPa)</u>: It is observed that the creep behavior of lateral stress under identical applied vertical stress resulting in an increase of K_0. Even though a further reduction in K_0 occurs early in each loading step due to the remaining cementation is observed, post-increasing of K_0 after reaching the constant vertical stress is also monitored. The increment of K_0 is more pronounced under the lower vertical stress of the higher hydrate-saturated specimens. Since no creep behavior is detected in the $S_h = 0$ specimen, it can be said that the presence of hydrate crystals causes the creep behavior of the K_0. The effect of creep behavior on the K_0 is not critical in granular materials (Yamamuro et al., 1996). In other words, changes in the applied vertical stress transfer to both soil grain particles and hydrate crystals, but there is an apparent time-delayed response on the stress transferred through the hydrate crystals. In this applied vertical stress range (1 MPa < σ_v < 25 MPa), the effect of creep behavior is

more dominant than that of the remaining cementation bonding, which results in the overall increase in the value of K_0.

Effects of the presence of hydrate crystals (1 MPa < σ_v < 25 MPa): The lower K_0 of the higher hydrate-saturated specimens can be observed across the stress range up to 25 MPa vertical stress. The lower K_0 can be oriented from not only the cementation effect but also the presence of hydrate crystals in pore spaces. Even though the majority of the cementation is broken due to the increasing vertical stress (σ_v > 1MPa), the presence of hydrate crystals between particles plays a vital role in enhancing strength and stiffness which causes the lower K_0. Hydrate crystals in pores can be considered as another group of solid particles or skeletal structures that can share the load (Pinkert and Grozic, 2014, Yoneda et al., 2016, Yoneda et al., 2019b). Since dense packing specimens typically have lower K_0 (Northcutt and Wijewickreme, 2013, Chu and Gan, 2004, Lee et al., 2013, Wanatowski and Chu, 2007), it can be said that a larger volume of hydrate crystals in specimens (i.e., higher hydrate saturation) causes more dense packing density resulting in the lower K_0 during loading.

Effects of sand crushing (σ_v > 10 MPa): The applied vertical stress up to 25 MPa in this study is enough to induce the crushing of sand grain particles and hydrate crystals (Chuhan et al., 2002, Hagerty et al., 1993, Kim et al., 2019b). Sand crushing causes the increase in K_0 because the crushed particles allow plastic flow in pore spaces (Yamamuro et al., 1996, Yao et al., 2014, Chu and Gan, 2004, Coop and Atkinson, 1993, Leroueil and Vaughan, 2009). Therefore, the increase of K_0, especially at high-stress levels, can be explained by not only the effect of creep behavior but also the effect of sand crushing.

However, the higher hydrate-saturated condition inhibits sand crushing because hydrate crystals in pore spaces prevent particle rearrangement and rotation (Kim et al., 2019b). Since the degree of recovery of K_0 is more pronounced in the higher hydrate-saturated specimen, the effect of creep behavior is the dominant factor causing the overall increase of K_0 under the stress range 1 MPa < σ_v < 25 MPa.

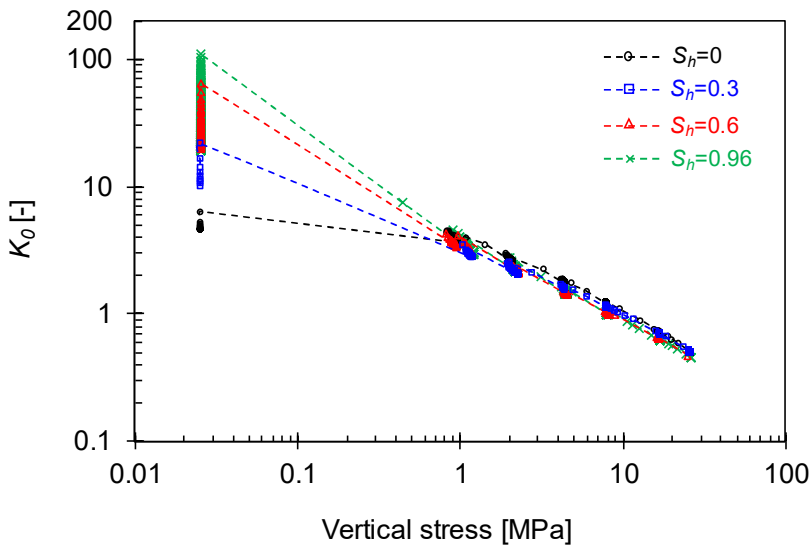

Figure 4.7 − Evolution of the coefficient of earth pressure K_0 during unloading for hydrate-bearing sediment with various hydrate saturation (S_h = 0, 0.3, 0.6, and 0.96).

In summary, the reduction in K_0 is expected for hydrate-bearing sediments under low vertical stress levels because of the cementation bonding effect, and this trend is more pronounced in the higher hydrate-saturated specimens. With the further increase of the vertical stress, the K_0 is governed by cementation debonding, the presence of hydrate crystals, the creep behavior of hydrate crystals, and sand crushing. These mixed influences cause the recovery of K_0 with the further increase of the vertical stress. Once the

cementation effect is weakened, the creep behavior of K-values is dominant resulting in the increase of K_0 as the applied vertical stress increases.

4.3.3 Effects of Unloading on Lateral Stress of Hydrate-Bearing Sediments

The behavior of K_0 during unloading is presented in Figure 4.7 and Figure 4.8. The values of K_0 of all specimens (S_h = 0, 0.3, 0.6, and 0.96) converge to 0.45-0.51 under 25 MPa vertical stress. As the vertical stress is unloaded, the values of K_0 of all specimens exponentially increase. During unloading, the values of K_0 increase more than 1, indicating the higher lateral stress than the vertical stress. It can be induced by the enhanced lateral direction particle interlocking with the decrease in applied vertical stress.

In Figure 4.7, there are no observable differences in the K_0 among various hydrate-bearing specimens until the vertical stress is reduced to 1 MPa. Once the vertical stress is further reduced to 0.025 MPa, significant differences in the values of K_0 among the specimens are observed. Once the vertical stress is lowered to 0.025 MPa, the higher saturated specimens have larger K_0 than the lower saturated specimens. As the vertical stress is kept constant at 0.025 MPa, the K_0 shows a significant reduction (creep behavior) with the elapsed time as shown in Figure 4.8. The creep behavior is more pronounced in the higher saturated specimens, but the higher saturated specimens have higher final K_0. After the K_0 stabilizes under 0.025 MPa vertical stress, the final values of K_0 are 4.6, 5.4, 18.1, and 18.9 for the specimens with S_h = 0, 0.3, 0.6, and 0.96, respectively.

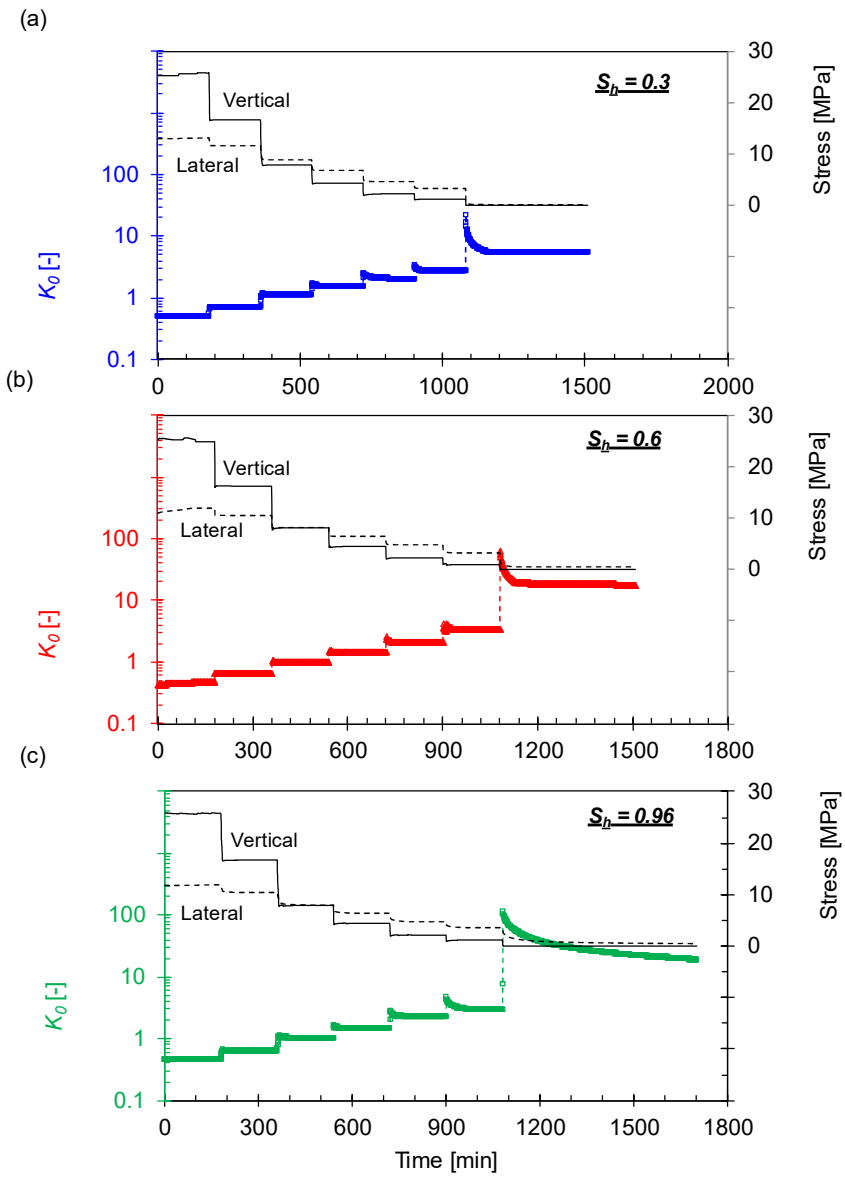

Figure 4.8 – The coefficient of earth pressure at rest K_0 and applied stresses versus time during unloading. (a) S_h = 0.3. (b) S_h = 0.6. (c) S_h = 0.96.

Rearrangement of sand particles and hydrate crystals: The values of K_0 have no substantial differences with varying hydrate saturation under 25 MPa vertical stress because of the rearrangement of internal structures with sand particles and hydrate crystals. This updated particle arrangement and skeletal structure contribute to having similar values

of K_0 during unloading (σ_v > 1 MPa) for all tested specimens. The results indicate that the degree of hydrate saturation, particle crushing, and remaining cementation bonding are minor factors to the evolution of K_0 because of the applied vertical stress (σ_v > 1 MPa) during unloading, but the enhanced interlocking in the lateral direction is a more dominant factor affecting the behavior of K_0.

Effects of the creep behavior of hydrate crystals: The creep behavior of K_0 during unloading is observed in Figure 4.8. This creep behavior during unloading is caused by the time-delayed response of the lateral stress, resulting in a sudden increase of K_0. When the vertical stress is reduced to 0.025 MPa, the value of K_0 increases sharply to more than 100 for the S_h = 0.96 specimen, and the peak values of K_0 are higher on the specimen with higher hydrate saturation. The result indicates that the presence of hydrate crystals may enhance the time-delayed response to lateral stress that results in the sudden increase of K_0 during unloading. During the following creep behavior, the values of K_0 decrease and then stabilize as the lateral stress decreases slowly. This creep behavior is much enhanced in the higher hydrate-saturated specimens. As a result of the creep behavior of lateral stress, the values of K_0 of the specimens show a considerable reduction and finalize to 5.4, 18.1, and 18.9 for S_h = 0.3, 0.6, and 0.96 specimens. The hydrate-free specimen (S_h = 0) has lower K_0 than the hydrate-bearing specimens after the unloading process. It can be said that the presence of hydrate crystals plays an important role in the considerable increase of K_0 of hydrate-bearing specimens. The higher K_0 of higher saturated sediments can be attributed to the larger volume of hydrate crystals in the sediments.

4.3.4 Effects of Hydrate Dissociation on Lateral Stress

After completing the unloading process, the temperature is raised to trigger hydrate dissociation on the hydrate-bearing specimens. The measured temperatures and K_0 during hydrate dissociation are summarized in Figure 4.9. Before hydrate dissociation, higher hydrate-bearing specimens have higher K_0 as a result of the loading and unloading processes. The values of K_0 show significant reductions when hydrate crystals start to dissociate as the temperature rises, and the degree of reduction is more pronounced in the higher hydrate-saturated specimens. This result indicates that the removal of hydrate crystals due to hydrate dissociation causes the reduction of K_0. In other words, the presence of hydrate crystals in the specimens contributes to higher K_0 for the higher saturated sediments. This phenomenon is also suggested by the hydrate dissociation experiment using natural cores of hydrate-bearing sediments from the Indian Ocean (Yoneda et al., 2019b).

After completed hydrate dissociation, no significant differences in K_0 are observed between hydrate-free sediments (S_h = 0, water-saturated) and hydrate-bearing sediments (S_h = 0.3, 0.6, and 0.96), even though the specimens with higher hydrate saturation have slightly higher K_0. Since all the hydrate crystals in the specimens are dissociated, the values of K_0 after the hydrate dissociation are mainly affected by the soil fabric. The sediments experienced hydrate formation, loading and unloading, and hydrate dissociation with various hydrate saturation levels. Although the various hydrate saturation levels cause different degrees of compression, sand crushing, and lateral stress history, the values of K_0 after hydrate dissociation show similar values comparing to the differences during the entire experimental procedures.

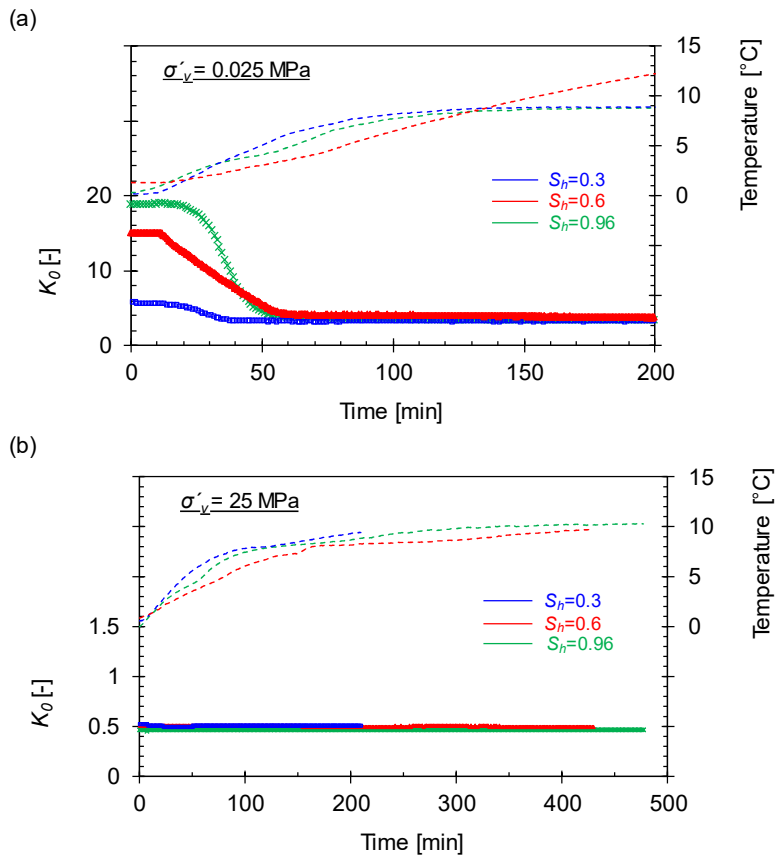

Figure 4.9 − Evolution of the coefficient of earth pressure at rest K_0 and specimen temperature during hydrate dissociation. Dashed colored lines indicate the measured temperature of the specimens during warming for hydrate dissociation. (a) Hydrate dissociation under 0.025 MPa vertical stress. (b) Hydrate dissociation under 25 MPa vertical stress.

The effects of hydrate dissociation under the higher vertical stress condition (i.e., 25 MPa) on the K_0 are summarized in Figure 4.9b. The hydrate is formed under 25 MPa vertical stress with various hydrate saturation (i.e., S_h = 0.3, 0.6, and 0.96), and then dissociated under identical vertical stress. With an increase in temperature, hydrate dissociation under 25 MPa vertical stress induces no distinguishable changes in K_0 in all

sediments. Unlike the behavior of K_0 during the hydrate dissociation under 0.025 MPa vertical stress (in Figure 4.9a), the removal of hydrate crystals has no significant effects on the K_0 under 25 MPa vertical stress. This result indicates that 25 MPa vertical stress does not allow any further changes in the particle arrangement and stress transmission to the lateral direction despite the removal of hydrate crystals. Since the values of K_0 show no observable changes during hydrate formation and dissociation under 25 MPa, it can be said the compressed pore space and soil skeleton caused by the applied vertical stress are more dominant factors in K_0 response than the presence of hydrate crystals.

4.3.5 Effects of Packing Density and Vertical Stress on Lateral Stress

Figure 4.10 presents the evolution of K_0 of hydrate-free specimens (S_h = 0, water-saturated) during loading and unloading with different maximum vertical stresses. The specimens are prepared with F110 fine sand with relative density D_r = 40% (loose packing) and 70% (dense packing). The water-saturated specimens are subjected to various maximum vertical stress levels (i.e., $\sigma_{v,max}$ = 0.05, 1, and 25 MPa). The dense specimens have slightly lower K_0 than the loose specimens before loading due to enhanced interlocking among particles (Zhu et al., 1995, Wanatowski and Chu, 2007, Yun and Evans, 2011). As the vertical stress increases to the targeted levels, the differences in K_0 between the loose and dense specimens become more pronounced. Since enhanced interlocked particles and less pronounced particle crushing are expected in the dense specimens with the increase in vertical stress (Lade et al., 1996, Guimaraes et al., 2007, Hagerty et al., 1993), the dense specimens show a more pronounced decrease in K_0 during loading.

Unloading induces an increase in K_0 for all specimens, but the higher OCR causes higher values of K_0. In other words, the specimens experiencing higher maximum vertical stress show a more pronounced increase in K_0 during unloading. This result can be explained by the fact that enhanced lateral stress locking is induced by higher OCR.

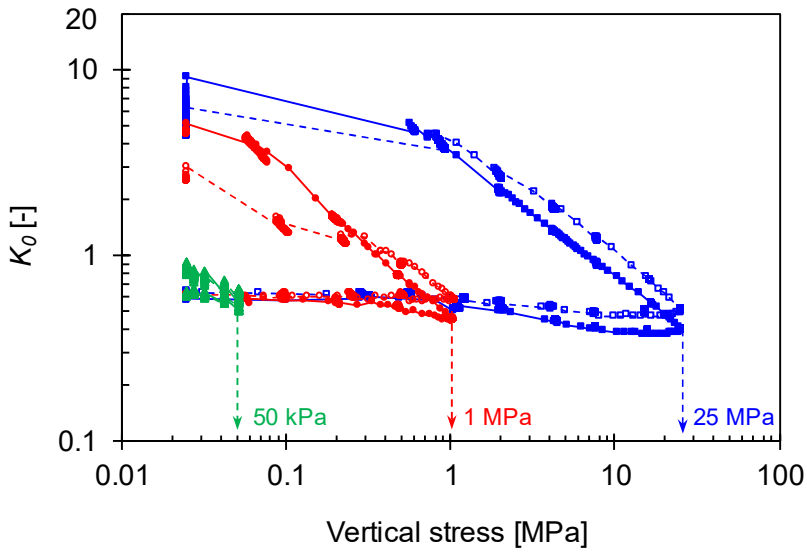

Figure 4.10 − Effects of the maximum vertical stress and packing density on the coefficient of earth pressure at rest K_0 for the hydrate-free specimen (i.e., S_h = 0, water-saturated). The specimens are prepared with a relative density of 40% (empty markers) and 70% (solid markers). The specimens are subjected to various maximum vertical stress (i.e., 0.05 MPa, 1 MPa, and 25 MPa) during the loading process and unloaded back to 0.025 MPa.

In the range of higher vertical stress during loading, the loose specimens have larger K_0 than the dense specimens. With further reduction in vertical stress, however, the K_0 of the dense specimens increase sharply resulting in the higher K_0 in the dense specimens under 0.025 MPa vertical stress. Therefore, it is confirmed that the higher K_0 of the

specimen with higher hydrate saturation can be resulting from the presence of hydrate crystals, which contribute to having dense packing conditions.

4.4 Conclusions

This study experimentally examines the evolution of the lateral stress coefficient at rest K_0 of hydrate-bearing specimens during hydrate formation, loading and unloading, and hydrate dissociation. The main conclusions follow.

- The hydrate formation process under low vertical stress (i.e., σ_v = 0.025 MPa) produces no remarkable changes in K_0 for S_h = 0.3 and 0.6 hydrate-bearing specimens. For S_h = 0.96 specimens, a sudden increase in K_0 is observed once the hydrate starts nucleation, but the values recover to the initial K_0.
- Hydrate-free sediment (S_h = 0, water-saturated) has slightly decreasing K_0 from 0.63 to 0.51 due to the compaction effect caused by the increasing vertical stress. When the applied vertical stress exceeds 10 MPa, the induced sand crushing prevents further decreases in K_0. The specimen with low hydrate saturation (S_h = 0.3) shows similar values of K_0 with the hydrate-free specimen, indicating no significant effects of hydrate crystals on stress transmission.
- Relatively higher hydrate saturation (S_h = 0.6 and 0.96) show a significant reduction in K_0 during loading up to 1 MPa, and this reduction is more pronounced as the hydrate saturation increases. For S_h = 0.96 specimens, the values of K_0 are smaller than 0.1, indicating that the presence of hydrate crystals provides strong cementation bonding between particles and less stress transmission in the lateral direction. With further increases of vertical stress (σ_v > 1 MPa), the values of K_0

start to recover with remarkable creep behavior (K_0-values increase with identical vertical stress levels). Finally, the values of K_0 all specimens under 25 MPa vertical stress show converged values of 0.45-0.51.

- During the unloading process, the K_0 increases due to lateral stress locking caused by the pre-loading process and the presence of hydrate crystals. When the vertical stress is reduced to 0.025 MPa, the higher hydrate-saturated specimens have higher values of K_0.
- Hydrate dissociation induces a significant reduction of K_0 due to the loss of hydrate crystals among particles, and the reduction is more pronounced in the specimen with higher hydrate saturation. After completion of hydrate dissociation, the values of K_0 of all specimens are close to 3.5-4.2. The results indicate that the presence of hydrate crystals plays an important role in the K_0 of hydrate-bearing specimens. The effects of hydrate dissociation on the K_0 are minor under high applied vertical stress levels (σ_v = 25 MPa in this study).
- Since the presence of hydrate crystals in the hydrate-bearing specimens play a vital role in the response of K_0 during loading and unloading through the cementation bonding/debonding and creep behavior, it is confirmed that the hydrate crystals can be considered as another group of solid materials which supporting and sharing the load with particles.

CHAPTER 5 PERMEABILITY ANISOTROPIC OF HYDRATE-BEARING SEDIMENT FROM OFFSHORE INDIA

5.1 Introduction

Gas production rate, heavily affected by reservoir permeability, governs the economic feasibility of producing natural gas from deep-water gas hydrate deposits (Ajayi et al., 2018, Moridis et al., 2009, Collett et al., 2019, Myshakin et al., 2019). Compared with other fundamental physical properties of hydrate-bearing sediments, studies on permeability in hydrate-bearing sediments are limited, especially for data on relative permeability, permeability anisotropy, and permeability at different length scales. The permeability of hydrate-bearing sediments can be measured in situ with downhole tools (Fujii et al., 2015) and in the laboratory on pressure cores (Konno et al., 2015a, Priest et al., 2015, Santamarina et al., 2015). However, measured permeability even for sediments at a single depth and location can vary by 4-5 orders of magnitude (Fujii et al., 2015), in part due to sampling disturbances (Dai and Santamarina, 2014, Waite et al., 2008) and differences between how various testing methods inherently measure permeability in different directions and at different scales (Dai and Santamarina, 2017).

Conventional permeability measurements in the laboratory are typically conducted using rigid- or flexible-wall cells, each designed to restrict the measured fluid flow to what passes through a known cross-sectional area of the specimen. The potential problem for a rigid-wall cell is that boundary flow can occur, especially for low-conductivity soils (Daniel et al., 1985). The contrasting flexible-walled approach, such as is used for a triaxial test, relies on a flexible membrane to eliminate side flow along the specimen boundary.

When measuring permeability anisotropy, permeameter must be able to change the direction of flow from vertical to horizontal. Horizontal flow is not well constrained in a cylindrical triaxial system, but a horizontal permeability estimate can be obtained through numerical modeling of measured relationships between the vertical and horizontal pressure gradients and associated fluid fluxes (Yoneda et al., 2019a).

This study uses a custom flow anisotropy cell to investigate geomechanical and hydrological properties of sediments recovered during the NGHP-02 expedition, with focuses on permeability anisotropy (i.e., horizontal to vertical permeability ratio) and relative permeability. Additional details of the geomechanical parameters of cores recovered from the same depths with and without tetrahydrofuran (THF) hydrate are described by Kim et al. (Kim et al., 2019a).

Two cores are tested in this study. One is a clayey silt core (Core NGHP-02-8B-30P, 247.44-247.50 mbsf) recovered from the seal-layer just above the primary hydrate reservoir of the Site NGHP-02-08 in Area-C (Figure 5.1). This core is hereafter called the seal core, containing fine-grained non-reservoir overburden sediment that overlies a coarser-grained reservoir section. Additional details about Site NGHP-02-08 are presented in Waite et al. (Waite et al., 2019) and additional studies of the seal core are presented in Jang et al. (Jang et al., 2019). The second core is a sandy silt core (Core NGHP-02-23C-10P, 284.5-284.65 mbsf) from within one of the primary hydrate reservoir layers at the anticline crest of Area-B (Figure 5.1), hereafter called the hydrate-bearing core. Additional details about Site NGHP-02-23 and the Area-B reservoir systems are presented by Jang et al. (Jang et al., 2019). Modeling studies conducted on the Area B and Area C sites are presented by

Moridis et al. (Moridis et al., 2009) and Myshakin et al. (Myshakin et al., 2019). Both the NGHP-02-08 and -23 cores were recovered as pressure cores. To preserve gas hydrate, cores were retained at high pressure and low temperature throughout the recovery, shipboard scanning and processing, storage, transport and analysis of these cores at the National Institute of Advanced Industrial Science and Technology (AIST) and the U.S. Geological Survey's Woods Hole Coastal and Marine Science Center (WHCMSC). Both cores were non-destructively examined with X-ray computed tomography, *P*-wave velocity, and γ-ray density scans using the Pressure-core Nondestructive Analysis Tools PNATs (Nagao et al., 2015). The cores were collected and stored with no effective stress, which allows each core to expand and increase its void ratio (Jang et al., 2019, Santamarina et al., 2015). The fine-grained seal core was tested using the Pressure Core Characterization Tools PCCTs (Santamarina et al., 2012) at the WHCMSC to obtain compressibility and permeability at near in situ effective stress (Jang et al., 2019), and the fine-grained specimen used here was depressurized at the in situ effective stress (~2 MPa) to minimize the sediment fabric disturbance. The coarser-grained hydrate-bearing core was also depressurized to allow the hydrate to dissociate. It could not be retained at its in situ stress during dissociation, but it was confined in its plastic core liner. The hydrate saturation was quantified by collecting and measuring the produced gas volume. Depressurized whole-round subsections were then shipped to the Georgia Institute of Technology for further geomechanical and hydraulic properties characterization of sediments with and without THF hydrate.

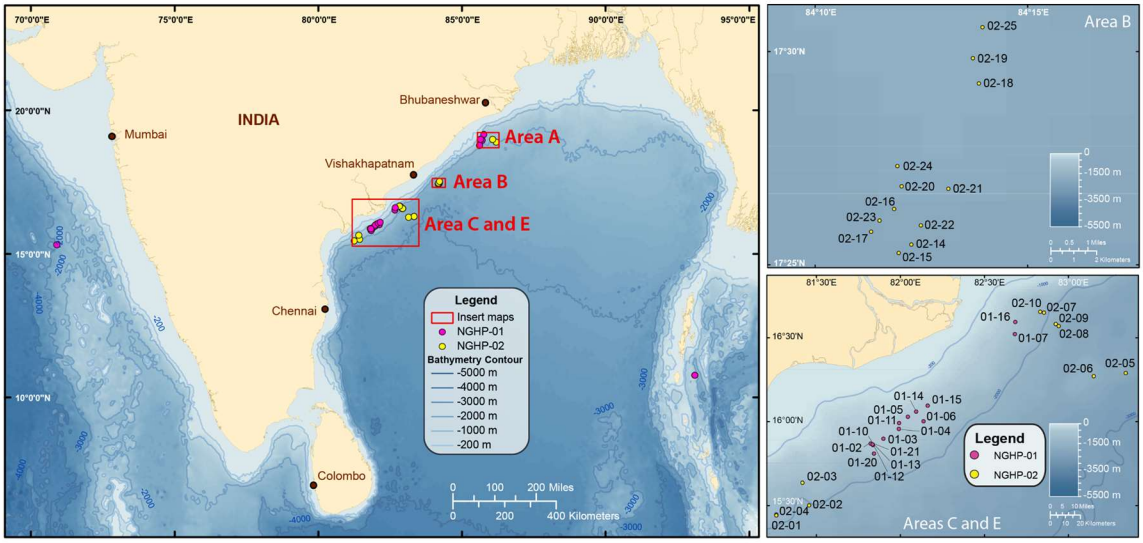

Figure 5.1 − Area map showing the NGHP drill sites from the 2006 NGHP-01 expedition and the 2015 NGHP-02 expedition.

5.2 Experimental Design

5.2.1 Index Properties

This study makes use of depressurized pressure cores; thus, they are initially gas-hydrate-free sediment samples. Specimens are retained as whole round cores to minimize sediment fabric disturbance. Based on specimen mass and the grain density measured with a pycnometer test, the seal core (Core NGHP-02-08B-30P) has an initial void ratio of e_o = 1.10 and the specific gravity of the sediment grains is G_s = 2.79. Liquid and plastic limits LL% = 60.6 and PL% = 22.5 are measured using a fall cone test, and the specific surface S_s = 278 m^2/g is obtained from the methylene blue method (Santamarina et al., 2002). The grain size distribution of the seal core, measured using a hydrometer, indicates a well-sorted clayey silt sediment, with median grain size d_{50} = 7.9 μm, characteristic grain size

d_{10} = 0.38 μm, coefficient of uniformity c_u = 33.8, coefficient of curvature c_c = 0.36, and only 3.4% by mass of sands (Figure 5.2).

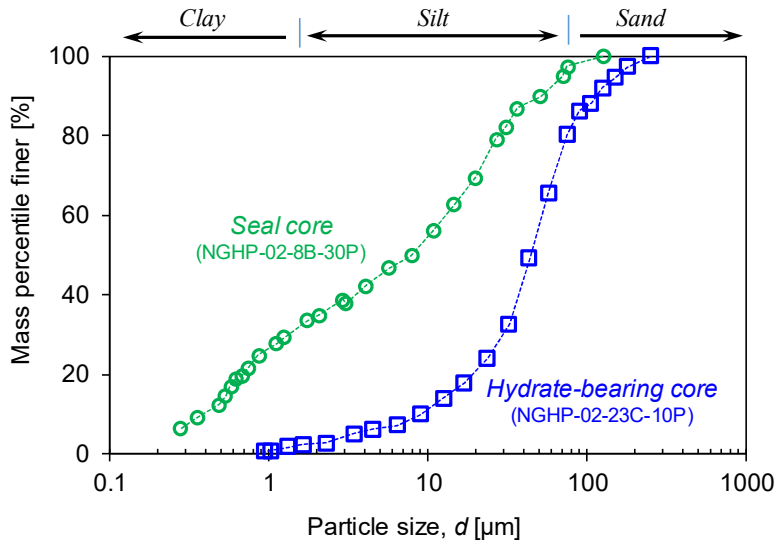

Figure 5.2 − The grain size distribution of the two tested specimens in this study: one clayey silt core (Core NGHP-02-08B-30P) from the seal layer above the primary gas hydrate reservoir at Site NGHP-02-08 (Area-C) and one silty sand core (Core NGHP-02-23C-10P) from within a Site NGHP-02-23 gas hydrate reservoir layer at offshore India.

Core NGHP-02-23C-10P, from a hydrate-bearing reservoir interval, has an initial void ratio of e_o = 1.09, specific gravity G_s = 2.65, liquid and plastic limits LL% = 35.1 and PL% = 15.5 (for fine grains < 75 μm only), and specific surface S_s = 17.7 m^2/g (for fine grains < 75 μm only). The grain size distribution analysis shows a sandy silt core, with median grain size d_{50} = 44.1 μm, characteristic grain size d_{10} = 9.0 μm, coefficient of uniformity c_u = 5.8, and coefficient of curvature c_c = 1.9, and 19.7% by mass of sands (Figure 5.2).

5.2.2 Experimental Procedures

Both cores are trimmed to fit into the 35.56×35.56×35.56 mm^3 sample chamber using a wire saw and loaded into a customized permeability anisotropy cell. Cores are then loaded vertically with vertical stresses of σ_v = 0.01, 0.1, 1, 2, 4, 8, 15, and 25 MPa, then unloaded to 10, 2, and 0.1 MPa. The peak vertical load, 25 MPa is chosen to simulate the 25.55 MPa effective stress suggested in the modeling study for the gas hydrate reservoir associated with Core NGHP-02-23C-10P (Myshakin et al., 2019). Loads are applied using a hydraulic piston within a reaction frame system. At the end of each loading or unloading step, vertical and horizontal permeability of the core are measured. Core height changes are monitored using a linear variable displacement transducer (LVDT) throughout the experiments. All tests are conducted within an environmental refrigerator with a constant temperature of 1 ± 0.1°C.

Two additional testing steps are performed on the Site NGHP-02- 23 core from the hydrate-bearing reservoir layer: (i) THF hydrate is formed at a nominal vertical stress σ_v = 0.01 MPa before loading, and dissociated after the core is unloaded to σ_v = 2 MPa; (ii) two water retention curves are obtained, one when the core with hydrate is loaded to 2 MPa and one after the core is unloaded back to 2 MPa and the hydrate had been dissociated. A hydrate saturation S_h = 0.8 (comparable with the sediment's in situ hydrate saturation calculated from the gas evolved from the core specimen during degassing, 79 ± 3%) is used in this study. To form THF hydrate, 30 pore-volumes of THF-water mixed solution is first circulated through the core to replace the initial pore fluid. The mixed solution has a mass ratio of 17.3THF:82.7H2O (Strauch et al., 2018), so that it would render a hydrate saturation S_h = 0.8 in the sediment pore space upon hydrate formation, with all remaining pore fluid fully saturated with THF.

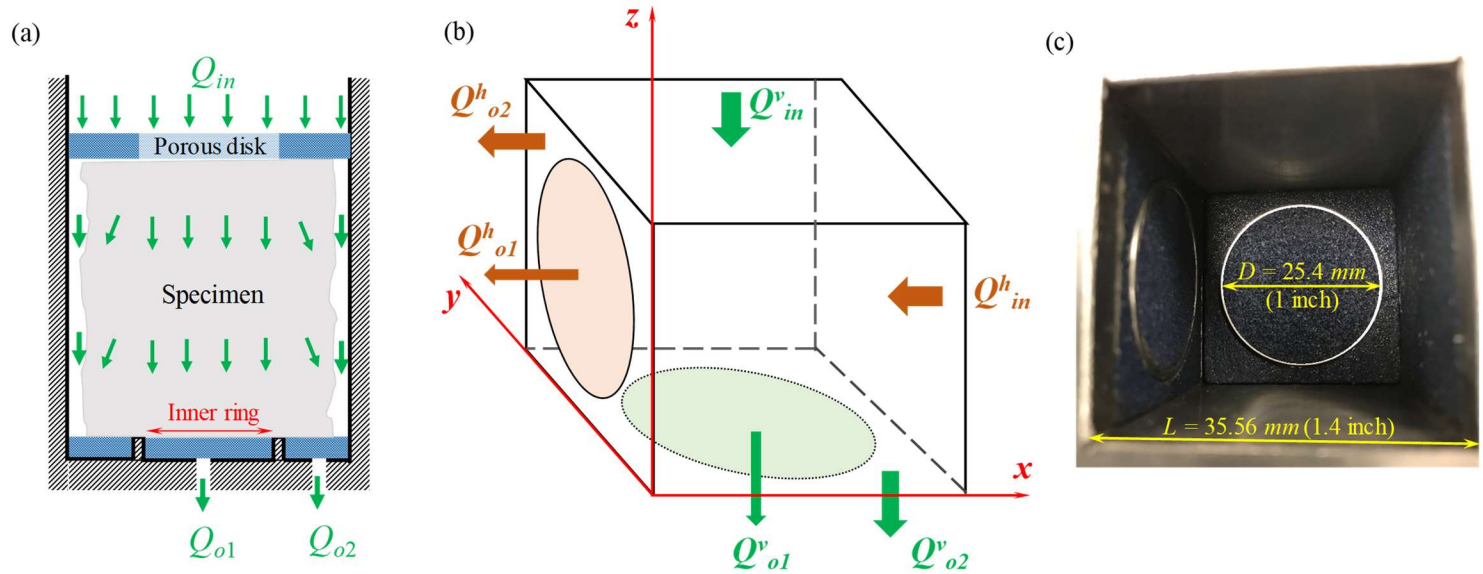

Figure 5.3 − Illustrations of the vertical and horizontal permeability measurement in a customized permeability anisotropy cell. (a) An illustration of the flow field with preferential flows at the boundary of a core in a rigid-wall permeameter. (b) The vertical and horizontal permeability is quantified using a double-ring concept to remove the boundary effects by utilizing only the fluid flowing through the central portion of the specimen (Q^v_{o1}). (c) The top view of the main chamber of the customized permeability anisotropy cell in this study.

5.2.3 A Customized Permeability Anisotropy Cell

A permeability anisotropy cell was customized in this study to quantify vertical and horizontal permeability in sediments. The cell uses a cubic specimen, 35.56 mm on a side, and specimen permeability is measured based on a double-ring concept to remove boundary effects (Figure 5.3). The gap between the specimen and the cell's rigid walls creates not only preferential flow at peripheral boundaries but also creates a distorted flow field and a variable hydraulic gradient across the specimen that presents a challenge to computing the measured permeability based on Darcy's law (Figure 5.3a).

Taking the vertical permeability measurement in the double-ring concept, for instance, a constant pressure difference ΔP is applied vertically across the specimen while the horizontal flow ports are all closed. The vertical outflow is collected separately from the inner ring Q^v_{o1} and the outer ring Q^v_{o2} (Figure 5.3b). Only flux through the inner ring Q^v_{o1}, which is not affected by the preferential boundary flow, is used to compute the permeability k_v given by:

$$k_v = \frac{Q^v_{o1}}{\Delta P}\frac{L}{A_{in}}\mu \tag{5-1}$$

where L is the specimen's height (or flow line length), μ is the viscosity of the fluid used for the permeability measurement, and A_{in} is the area of the inner ring, which has a diameter of 25.4 mm in this study (Figure 5.3c). Similarly, the horizontal permeability k_h can be determined (with all vertical inlet and outlets closed) as:

$$k_h = \frac{Q_{o1}^h}{\Delta P} \frac{L}{A_{in}} \mu \tag{5-2}$$

Porous disks are placed at each inflow and outflow side of the specimen to have uniformly spread flow passing through the tested specimen. Note also that preferential flow at core boundaries will be reduced with increasing load, which squeezes the specimen more tightly against the cell walls. Additional details of using the double-ring method to measure permeability can be found in ASTM D3385 and ASTM D5093.

Water retention curves are measured by applying a gas pressure on top of the core while collecting the drained water from the core's base. After no more drained water can be detected by a high precision scale (accuracy of 0.0001 g), gas pressure is increased and the measurement is repeated until the maximum pressure of 800 kPa is reached. Thus, the water retention curve consists of a series of relations between the applied gas pressures (i.e., capillarity) versus the amount of drained water (to be converted into saturation decrease). Water retention curves are measured in the vertical direction with all side valves closed.

5.3 Experimental Results

5.3.1 Stress-volume Responses

Figure 5.4 shows stress-volume responses for the two tested specimens within the flow cell under zero lateral strain and vertical stresses up to 25 MPa. The seal core (Core NGHP-02-08B-30P) starts with an initial height H_o = 39.88 mm and a corresponding initial void ratio e_o = 1.10 at a nominal vertical stress σ_v = 0.01 MPa. Void ratio decreases to e =

0.53 at the maximum applied vertical stress of 25 MPa. The compression index at this stress level is C_c = 1.20. The seal core swells slightly during unloading to 0.1 MPa, with a swelling (recompression) index C_s = 0.013 and final specimen height H_f = 29.54 mm.

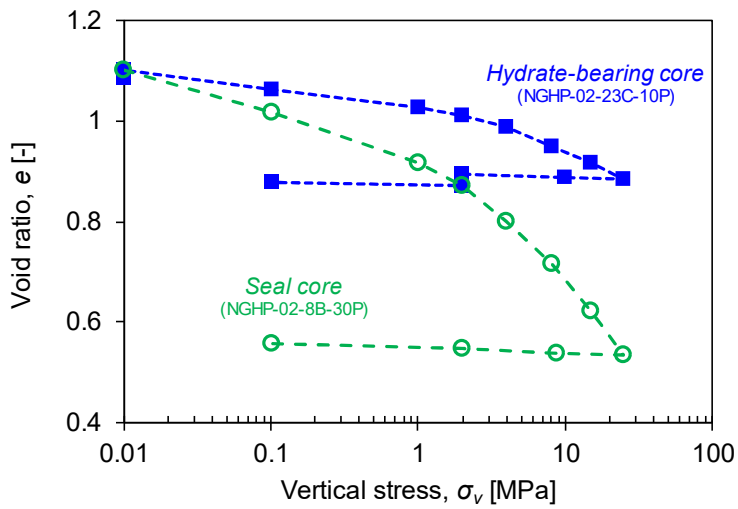

Figure 5.4 − The stress-volume responses (up to 25 MPa vertical stress) of the two tested specimens: one clayey silt seal core (Core NGHP-02-08B-30P) and one silty sand reservoir core (Core NGHP-02-23C-10P) with THF hydrate (S_h = 0.8).

The hydrate-bearing core (Core NGHP-02-23C-10P) starts with an initial height H_o = 39.37 mm and a corresponding initial void ratio e_o = 1.09 at a nominal vertical stress σ_v = 0.01 MPa. THF hydrate formation (S_h = 0.8) at this stress increases the specimen's height to 39.69 mm, an increase of 0.32 mm, equivalent to a vertical strain increase of $\Delta\varepsilon_z$ = 0.01. The void ratio decreases to e = 0.88 at the applied vertical stress of 25 MPa. The compression index is C_c = 0.13 as the specimen is loaded from 15 to 25 MPa. The specimen then swells from 35.57 mm to 35.74 mm when unloaded from 25 MPa to 2 MPa, corresponding to a swelling index C_s = 0.008. THF hydrate dissociation is triggered at this

stress and causes a 0.43 mm settlement, equivalent to a vertical strain change of $\Delta\varepsilon_z = 0.012$. After hydrate dissociation, vertical stress in unloaded to 0.1 MPa and the specimen's height increases to 35.27 mm, corresponding to a swelling index for hydrate-free sediments C_s = 0.005.

5.3.2 Vertical and Horizontal Permeability

Figure 5.5 presents measured vertical and horizontal permeabilities in the two tested cores at various stress conditions. At a vertical stress $\sigma_v = 0.1$ MPa, measured vertical and horizontal permeability are nearly identical. With increasing vertical stress, both vertical (k_v) and horizontal (k_h) permeability decrease due to compression decreasing the void space. However, horizontal permeability decreases more slowly than vertical permeability with increased vertical stress, i.e., the difference between the two permeabilities increases with vertically applied stress. After unloading, permeability barely recovers.

Both the vertical and horizontal permeability start from ~0.1 mD (mD = milliDarcy = 9.869×10^{-16} m^2) in the clayey silt seal core at $\sigma_v = 0.1$ MPa (Figure 5.5a). Horizontal permeability decreases to $k_h = 0.042$ mD when vertically applied stress increases to $\sigma_v = 8$ MPa. Beyond 8 MPa, the specimen is too short to reach the top of the horizontal inner ring due to the specimen's high compressibility. Any additional horizontal permeability measurements using collected flux through the inner ring would contain a boundary flow component (i.e., $Q_{o1}^{h} + Q_{o2}^{h}$, refer to Figure 5.3b). Therefore, horizontal permeability measurements are not taken above 8 MPa vertical stress. Vertical permeability at in situ vertical stress $\sigma_v = 2$ MPa is $k_v = 0.032$ mD. As a reference, the same core measured using the Pressure Core Characterization Tools has a vertical permeability $k_v = 0.012$ mD at the

in situ stress (Jang et al., 2019). Vertical permeability decreases with increasing vertical load until k_v = 0.008 mD at σ_v = 25 MPa. After unloading back to σ_v = 0.1 MPa, vertical permeability remains nearly unchanged k_v = 0.0082 mD.

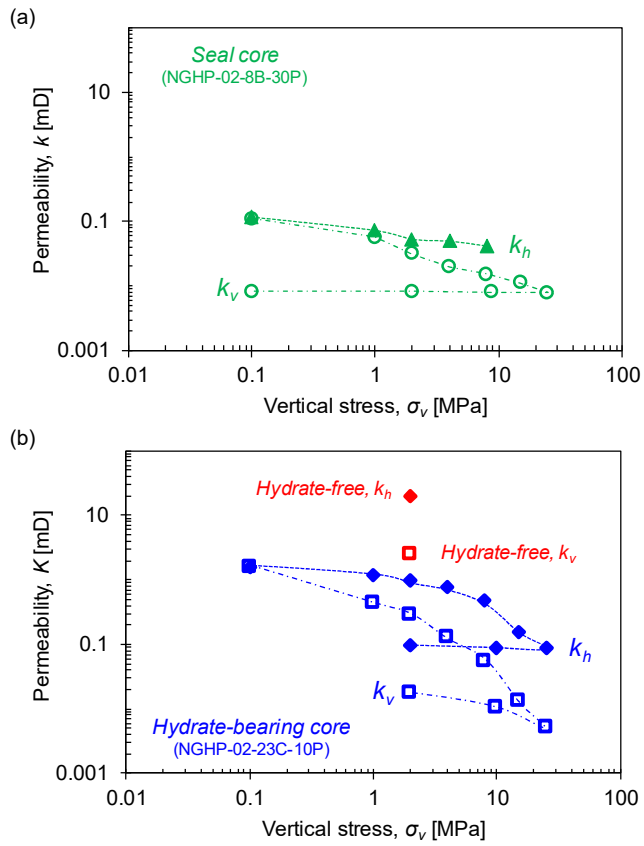

Figure 5.5 − Measured vertical and horizontal permeability in the two tested cores under various vertical stresses. (a) Vertical (open circles) and horizontal (solid triangles) permeability of the seal core during loading and unloading. (b) Vertical (open squares) and horizontal (solid diamonds) permeability of the silty sand specimen with hydrate S_h = 0.8. Hydrate is dissociated when the vertical stress is unloaded to 2 MPa and the vertical (open red square) and horizontal permeability (solid red diamond) of the hydrate-free sediments are also measured.

For the hydrate-bearing core (S_h = 0.8), the vertical and horizontal permeability are ~1.57 mD at a vertical stress of σ_v = 0.1 MPa (Figure 5.5b). Vertical permeability decreases

to k_v = 0.29 mD when the vertically applied stress increases to σ_v = 2 MPa and to k_v = 0.005 mD when σ_v = 25 MPa. After unloading to σ_v = 2 MPa, vertical permeability increases slightly to k_v = 0.017 mD. THF hydrate dissociation is triggered at this stress, leading to a vertical permeability increase to k_v = 2.46 mD for the hydrate-free sediments (nearly a factor of 145 increase). The horizontal permeability decreases to k_h = 0.96 mD at σ_v = 2 MPa, to k_h = 0.085 mD at σ_v = 25 MPa, and remains nearly unchanged at k_h = 0.094 mD when the vertical stress is unloaded to σ_v = 2 MPa. During this unloading, the specimen's height slightly increases from 35.57 mm to 35.74 mm. After hydrate dissociation, horizontal permeability increases to k_h = 20.02 mD (nearly 210 times higher than that of the hydrate-bearing specimen under the same vertical stress σ_v = 2 MPa).

5.3.3 Water Retention Curves

Figure 5.6 shows two water retention curves for the core from a hydrate-bearing reservoir layer (Core NGHP-02-23C-10P): one curve is obtained when the core contains THF hydrate at S_h = 0.8 and is measured at the in situ vertical stress of 2 MPa, and the second curve is measured after hydrate dissociation, also at 2 MPa but after the core has experienced 25 MPa maximum vertical stress. Both water retention curves are fitted using the van Genuchten model (Van Genuchten, 1980):

$$P_c = P_o \left[\left(\frac{S_w - S_{rw}}{1 - S_{rw}} \right)^{-\frac{1}{m}} - 1 \right]^{1-m} \tag{5-3}$$

where the capillarity-water saturation (P_c - S_w) relationship is characterized using three parameters: the gas-entry pressure P_o, residual water saturation S_{rw}, and the curve shape factor m. The inset table in Figure 5.6 lists best-fit values for these three parameters, which are all hydrate saturation dependent. The presence of hydrate in sediments increases air-entry pressures P_o due to reduced available pore throat sizes, and enhanced the residual water saturation S_{rw}, possibly due to reduced pore size and the blockage of drainage pathways by hydrate. The decrease in m-value in the presence of hydrate indicates a steeper water retention curve, indicating a stronger dependence of capillary pressure on water saturation (Dai and Santamarina, 2013, Mahabadi et al., 2016b).

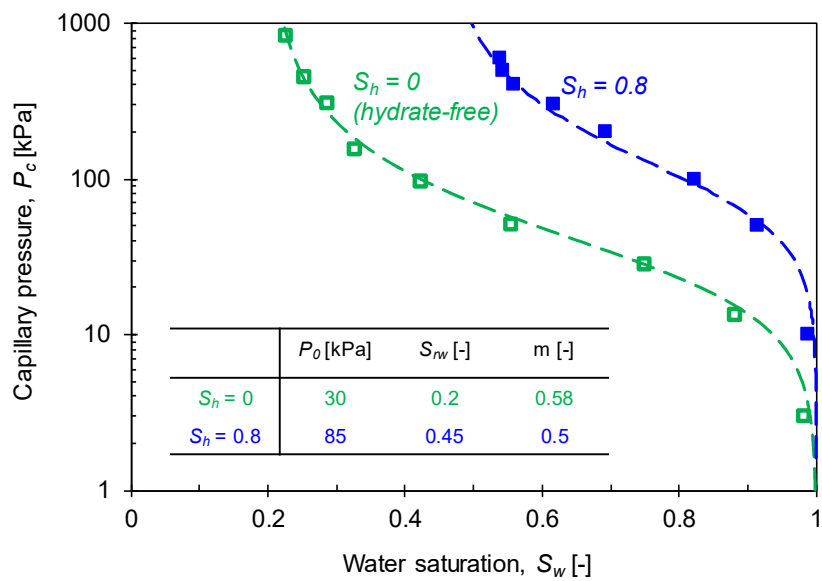

Figure 5.6 − Measured water retention curves in the silty sand core with and without THF hydrate (S_h = 0.8). The water retention curve in the sediments with hydrate is measured when the specimen is vertically loaded to 2 MPa. The curve in the sediments without hydrate is measured after hydrate dissociation when the core is unloaded back to 2 MPa vertical stress. Both curves are fitted using the van Genuchten model and the inset table lists the best-fit values for the three parameters in the model.

5.4 Analyses and Discussion

5.4.1 Permeability Anisotropy

Permeability anisotropy is presented in terms of the horizontal to vertical permeability ratio k_h/k_v in this study. The k_h/k_v ratios in the seal and hydrate-bearing core under various vertical stresses are plotted in Figure 5.7. At low-stress conditions, $\sigma_v \leq 0.1$ MPa, the k_h/k_v ratio approximates unity in both cores, i.e., no distinguishable permeability anisotropy. Inevitable sampling disturbances and the expansion of the core due to lack of effective stress may account for the permeability isotropy at the low-stress. However, the permeability anisotropy in both tested cores increases exponentially with vertically applied stress. Even more significant permeability anisotropy is observed in the hydrate-bearing core. The k_h/k_v ratio dependence on the vertical stress σ_v is described as:

$$\frac{k_h}{k_v} = \alpha \left(\frac{\sigma_v}{1MPa} \right)^{\beta} \tag{5-4}$$

where α is a reference permeability anisotropy at a reference vertical stress $\sigma_v = 0.1$ MPa, which is $\alpha = 1.6$ and 3 respectively for the seal and hydrate-bearing cores in this study. β reflects the sensitivity of permeability anisotropy to stress change, with $\beta = 0$ implying permeability anisotropy is not stress-dependent. The β values are 0.22 and 0.5 for the seal and hydrate-bearing cores respectively (Figure 5.7). The results suggest that at the in situ effective stress (~ 2 MPa), the permeability anisotropy is approximately $k_h/k_v = 1.86$ for the seal core and $k_h/k_v = 4.24$ for the core from the gas hydrate reservoir layer at a hydrate saturation $S_h = 0.8$. As a comparison, permeability anisotropy measured in a reservoir

sediment layer from the same reservoir (Core NGHP-02-16B-4P) with hydrate saturation S_h = 0.716 using a triaxial system with a jacketed specimen at in situ stress is k_h/k_v = 4 (Yoneda et al., 2019a). Both results compare well with the anisotropy ratio of 5 derived from history-matching a flow test at the Mallik permafrost gas hydrate research well (Uddin et al., 2012). The permeability anisotropy (i.e., higher k_h than k_v particularly at high stress) implies that permeability anisotropy must be considered; otherwise, assuming the vertical permeability obtained from permeameter tests is equivalent to the bulk permeability will underestimate the reservoir flow performance, which is mainly radial and horizontal during gas production. Additionally, because the depressurization required for gas production also reduces pore water pressure, the formation's effective stress increases and thus a more pronounced permeability anisotropy is expected as depressurization and effective stress increase. This stress-dependent permeability anisotropy can also help improve reservoir simulations by considering the changes in permeability and permeability anisotropy with the change in stresses due to sedimentation or transient pore pressure.

Permeability anisotropy in soils is usually attributed to macro-/micro-stratification and the flatness and orientation of particles (Witt and Brauns, 1983). The permeability of the tested seal and hydrate-bearing cores is isotropic at low-stress conditions, suggesting indistinguishable effects to permeability anisotropy from stratification or particle shape for these two tested cores in their unconfined state. The permeability becomes more anisotropic with increasing stress for both cores, however, highlighting how permeability anisotropy is inherently caused by anisotropic stress and deformation. Both tested cores are loaded at a zero lateral strain condition, meaning horizontal stress σ_h is proportional to vertical stress σ_v with a ratio given by the coefficient of earth pressure at rest, $K_o = \sigma_h/\sigma_v$,

which is a constant for a given specimen and mainly depends on friction angle and stress history. As vertical stress increases, the difference between the vertical and horizontal stress increases $(\sigma_h - \sigma_v) = (K_o - 1)\sigma_v$, and meanwhile, the cores are compressed vertically with zero lateral deformation. Although horizontal and vertical permeability both recover slightly after unloading (refer to Figure 5.5), the permeability anisotropy during unloading follows the same trend as during loading for the hydrate-bearing core.

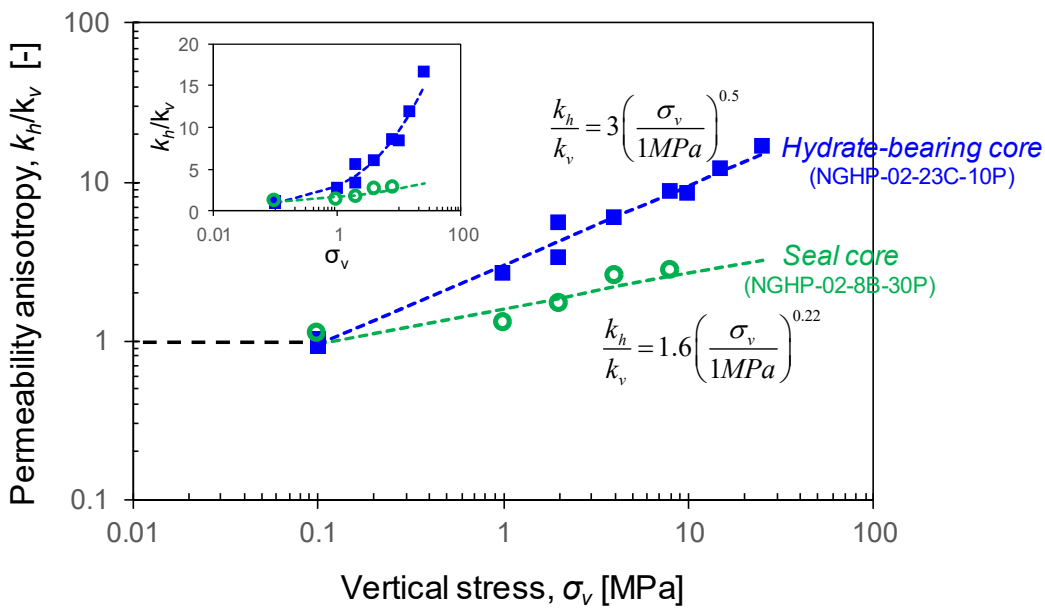

Figure 5.7 − Permeability anisotropy: the horizontal to vertical permeability ratio k_h/k_v in the seal core and the hydrate-bearing core as a function of vertically applied stress σ_v. The inset plot shows the permeability anisotropy on a linear scale.

5.4.2 Permeability-Porosity Relation

Permeability is often empirically linked with porosity in various geomaterials, such as shales (Soeder, 1988), mudstones (Yang and Aplin, 2010), coal (McKee et al., 1988), basalts (Saar and Manga, 1999), various types of sandy, silty, and clayey sediments (Ren

and Santamarina, 2018), and hydrate-bearing sediments (Konno et al., 2015b). Shown in Figure 5.8a, vertical and horizontal permeability in both cores under various stress conditions are plotted in terms of effective porosity, $\varphi_{eff} = \varphi\ (1 - S_h)$, which accounts for the effective pore spaces for flow in hydrate-bearing sediments and is equal to the sediment's bulk porosity φ when it is hydrate-free. The porosity of the hydrate-free seal core in this study is reduced from 0.53 to 0.35 due to the stress increase, which causes a reduction in permeability of bout one order of magnitude. For the hydrate-bearing core, its effective porosity is reduced only from 0.18 to 0.15 due to loading, yet this causes a reduction in permeability of about three orders of magnitude. The results highlight that permeability change is particularly sensitive to porosity change in hydrate-bearing sediments, especially for high hydrate saturations, which makes the initial effective porosity small. Strain in hydrate-bearing sediments is accommodated by the deformation of mostly the water-filled pores rather than the hydrate-filled pores, and thus decreases the effective pore spaces available for flow. Additionally, porosity as a bulk property of sediments does not reflect permeability anisotropy.

Permeability-porosity data of hydrate-bearing sands, silts, and clayey sediments from Nankai Trough (Konno et al., 2015b) are also presented in Figure 5.8a. This figure shows that sands, silt, and clay, in spite of having similar effective porosity (i.e., the volume ratio of effective pore spaces for flow over the total sediment volume), are 4–5 orders of magnitude different in permeability. Conversely, specimens with similar permeabilities, such as Core NGHP-02-23C-10P and Core NGHP- 02-8B-30P near ~0.1 mD, have effective porosity ranging from 0.15 to 0.5. These observations strongly suggest that permeability is not governed by void ratio but instead by pore size and soil type. Unique

permeability–porosity relations can only be established within individual soil types (Ren and Santamarina, 2018). For the two tested cores in this study, permeability for each core monotonically depends on its effective porosity regardless of whether the specimen is undergoing a loading or unloading stage.

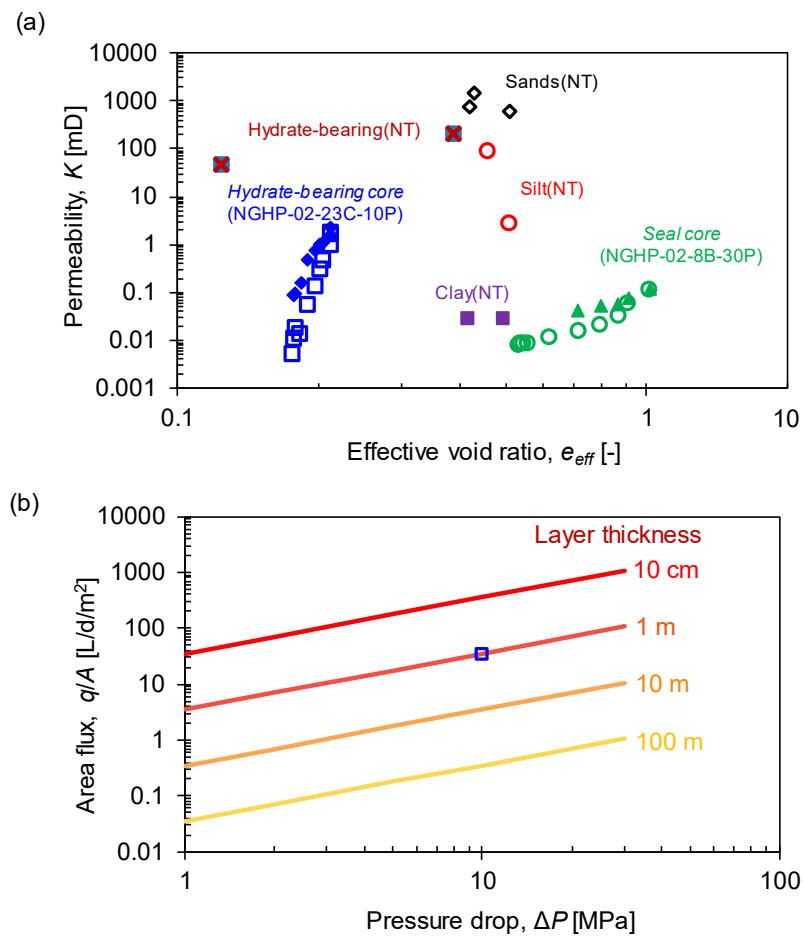

Figure 5.8 − Permeability in gas hydrate reservoirs. (a) Void ratio dependent permeability in the two tested NGHP-02 cores, together with data for hydrate-bearing sands, sands, and clayey sediments from Nankai Trough, noted by NK (Konno et al., 2015). Vertical permeability in open symbols for Cores and horizontal permeability in solid symbols. (b) The low permeability of the seal material may considerably slow down pore pressure recovery and cross-bedding flows during gas production. A 1m-thick seal layer subjected to 10 MPa pressure difference allows only 35.3 liters of cross-bedding water flow per day per m^2 in the reservoir (blue square).

The measured permeability of the seal core at the in situ vertical stress of ~2 MPa is about 0.03-0.05 mD. Such a low permeability material can compartmentalize pore pressure and dramatically slow down cross-bedding pore pressure recovery and reduces fluid fluxes during gas production. Having an essentially impermeable layer in contact with the hydrate reservoir is critical for enabling a depressurization technique to work. As modeled by Ajayi et al. (Ajayi et al., 2018), for instance, even small increases in the permeability of the sediment overlying the reservoir dramatically reduce how effectively the production well pumping are able to retain the low pore pressures needed in the gas hydrate-bearing reservoir sediment to continue dissociating gas hydrate. Figure 5.8b indicated the effectiveness of the tested seal sediment, showing computed water fluxes (in liter per day per square meter) across the seal material with different thicknesses subjected to pressure drops ranging from 1 MPa to 30 MPa. Results show that a 1 m-thick of this seal layer subjected to 10 MPa pressure difference will allow only 35.3 L of cross-bedding water flux per day per square meter. At an extreme condition, a 100 m-thick seal layer experiencing a 30 MPa pressure drop (note that in situ pore pressure 28.77 MPa) would pass only 1.1 L of water per day per square meter across the seal.

5.4.3 Water Retention Curves and Relative Permeability

The water retention curve describes capillarity at different water saturations in sediment. Since capillarity is primarily governed by pore radius r_p, assuming the water-gas interfacial tension (72 mN/m) and contact angle (0°) remain unchanged within the system during the measurement, water retention curves in the core with and without THF hydrate (Figure 5.6) captures the size distribution of effective pore spaces for flow, as shown in

Figure 5.9a. The effective pore radius for flow r_p, which is computed from the measured capillarity based on the Young-Laplace equation and the corresponding number of pores with effective radius r_p (described as an equivalent probability density function *PDF* here) is approximately by:

$$PDF = \left(\frac{\partial S_w}{\partial P_c} \right)^{1/3} \tag{5-5}$$

here $\partial S_w / \partial P_c$ is the ratio of saturation change over capillarity change and is quantified using the total discharged water volume at a particular capillarity. By approximating the volume as being the cube of the pore radius, the cube root of volume change at a particular capillarity becomes a measure of the number of pores at each pore radius (Figure 5.9a). Results show that the full pore size distribution of the core without THF hydrate ($S_h = 0$) and the distribution of effective non-hydrate pore-size for flow in the core with $S_h = 0.8$ both follow a log-normal distribution, as observed in many other natural sediments (Phadnis and Santamarina, 2011). THF hydrate formation decreases the mean effective pore size for flow from ~10 μm to ~2 μm, without evidently changing the distribution deviation (note: median grain size of this core $d_{50} = 44.1$ μm).

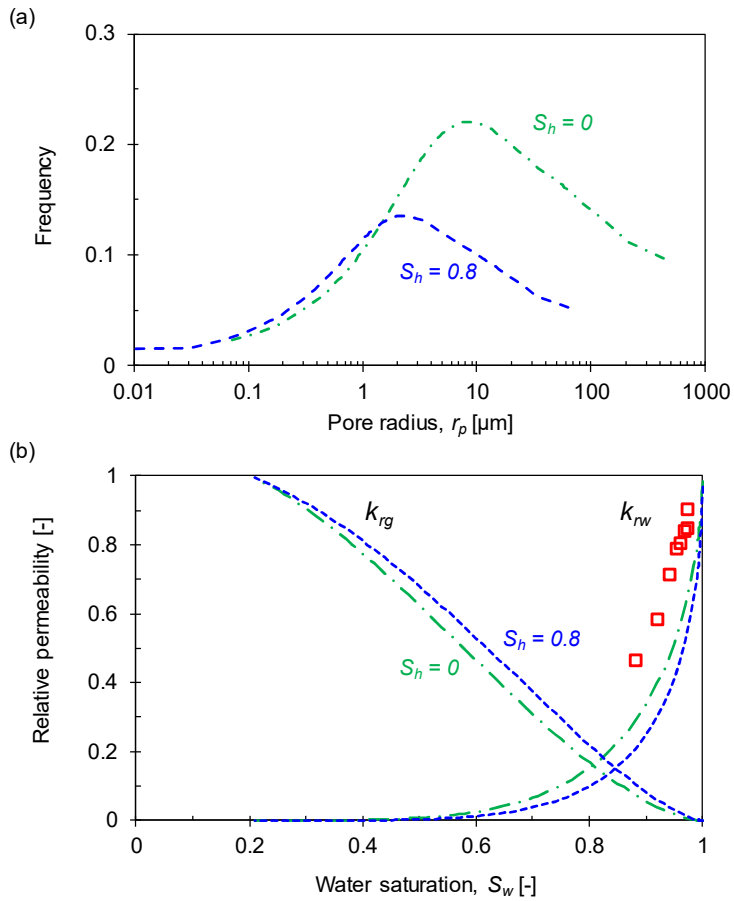

Figure 5.9 − Gas and water flow in hydrate-bearing sediments. (a) Inferred pore size distribution in the silty sand core with hydrate (S_h = 0.8) and without hydrate from the measured water retention curves. (b) Calculated relative gas k_{rg} and water k_{rw} permeability in the silty sand core with hydrate (S_h = 0.8) and without hydrate using the van Genuchten model and fitting parameters. Open squares are experimental values of relative water permeability in hydrate-free silty sand from Nankai Trough (Santamarina et al., 2015).

Figure 5.9 also indicates that THF hydrate preferentially forms in the larger pores. This result is a consequence of the manner in which the initial mixture of THF and water was introduced into the specimen. To preserve the sediment fabric, the THF/water mixture was not physically mixed into the sediment. Instead, the THF/water mixture was introduced by flushing the specimen with a volume of THF/water mixture equal to thirty

times the specimen pore volume. The final distribution of THF hydrate within the specimen indicated how flushing replaces original pore water only in the large pores that make up the dominant flow pathways through the specimen. Smaller pore networks that do not participate in the primary vertical fluid flow paths likely retained their original pore water and did not participate in hydrate formation. The hydrate formation preference for larger pores has been documented in natural systems, where the supply of methane dissolved in pore water is critical for supplying the methane necessary for hydrate growth (Uchida et al., 2009).

The two water retention curves have been fitted using the van Genuchten model with parameter values listed in Figure 5.6. These parameters can be further used to estimate relative permeability to gas k_{rg} and water k_{rw} (Parker et al., 1987, Van Genuchten, 1980):

$$k_{rw} = \sqrt{\frac{S_w - S_{rw}}{1 - S_{rw}}} \left\{ 1 - \left[1 - \left(\frac{S_w - S_{rw}}{1 - S_{rw}} \right)^{\frac{1}{m}} \right]^m \right\}^2 \tag{5-6}$$

$$k_{rg} = \sqrt{1 - \frac{S_w - S_{rw}}{S_{w\max} - S_{rw}}} \left[1 - \left(\frac{S_w - S_{rw}}{S_{w\max} - S_{rw}} \right)^{\frac{1}{m}} \right]^{2m} \tag{5-7}$$

where S_{wmax} is the water saturation at which gas percolates through the medium, assumed to be one here for simplicity (Moridis et al., 2009). As THF hydrate dissociates, m increases as shown in Figure 5.6 (see also (Mahabadi et al., 2016b, Mahabadi et al., 2016a)), leading to a downward shift in relative permeability to gas and upward shift in relative permeability

to water (Figure 5.9b). Note that the water saturation in hydrate-bearing sediments is defined as the ratio of the volume of water to the volume of the effective pore spaces for flow. Therefore, the water saturation in Figure 5.9b ranges between 0 and 1, not between 0 and 0.2, for hydrate-bearing sediments with $S_h = 0.8$.

Permeability is a measure of the ability of sediments to allow fluids (gases or liquids) to pass through. For hydrate-bearing sediments, the intrinsic permeability K_{int} typically refers to the permeability of the host sediments without hydrate. The presence of hydrate in sediments reduces pore spaces and thus decreases permeability to value, usually called the effective permeability K_{hyd}. A majority of experimental, numerical, and analytical studies to date have been looking into how effective permeability K_{hyd} decreases with increasing hydrate saturations S_h, i.e., the permeability reduction curve (Dai and Seol, 2014, Delli and Grozic, 2014, Kang et al., 2016, Kleinberg et al., 2003, Kleinberg et al., 2005, Minagawa et al., 2009, Kneafsey et al., 2011). Few studies address mixed gas and water flow in hydrate-bearing sediments during gas hydrate dissociation (Daigle, 2016, Johnson et al., 2011, Kneafsey et al., 2011, Mahabadi and Jang, 2014, Xu et al., 2017), mainly due to experimental difficulties in maintaining hydrate saturation and the complexity of capillarity on flow patterns in porous media. The apparent permeability of gas K_g and water K_w depend on the effective permeability K_{hyd} of the hydrate-bearing sediments and the relative permeability of each phase (ranging from zero to one):

$$K_{g,w} = K_{hyd} k_{rg,rw} = f\left(K_{\text{int}}, S_h\right) k_{rg,rw} \tag{5-8}$$

The change in intrinsic permeability K_{int} after hydrate dissociation is affected by in situ effective stress before hydrate dissociation, pore pressure drop during hydrate dissociation, and additional shear stress after hydrate dissociation. The effective stress increases with pore pressure reduction, so stress transfer from the water phase onto the skeleton during depressurization can cause sediment volume reduction or even particle crushing that leads to evident intrinsic permeability reduction. On the other hand, additional shear stress during hydrate dissociation (Hyodo et al., 2013) may cause skeleton dilation in densely packed sediments. Gas hydrate dissociation increases effective permeability K_{hyd} by reducing the hydrate saturation S_h. The relative permeability to gas k_{rg}, however, is governed by two competing mechanisms: hydrate saturation decrease shifts the curve of the relative gas permeability to gas downward (Figure 5.9b), but increased gas saturation (S_g = 1-S_w-S_h) during hydrate dissociation increases the values of relative permeability to gas. Given the narrow bounds between the k_{rg} curves for hydrate-bearing and hydrate-free sediments (Figure 5.9b), the increase in gas saturations due to gas hydrate dissociation prevails, so relative permeability to gas k_{rg} will rise according to the gas saturation, with k_{rg} transitioning from the high- to low-S_h curve during hydrate dissociation (Figure 5.9b).

5.5 Conclusions

This study experimentally investigates the hydraulic behaviors of cores recovered from the Site NGHP-02-08 seal layer and a Site NGHP-02-23 gas hydrate reservoir layer offshore India during NGHP Expedition 02. Results allow the following conclusions to be drawn:

- After unloading, both horizontal and vertical permeability barely recover, in keeping with the lack of void ratio recovery during unloading. This irreversible reduction in permeability is caused by the effective stress exceeding the sediment's pre-consolidation stress.
- The permeability decrease due to an effective stress increase is more sensitive in hydrate-bearing than hydrate-free sediments due to the limited fraction of fluid-filled volume that can compact in hydrate-bearing sediment.
- The measured permeability of the seal core at in situ vertical stress ~2 MPa is about 0.03-0.05 mD. A 10 cm-thin layer of this material interbedded with hydrate-bearing sediments can compartmentalize cross-bedding flow during gas production for about 10 years, and a 100 m-thick overburden of this material would be able to seal against pore pressure recovery over geologic timescales of approximately 10,000 years.
- The permeability of the tested seal core and the hydrate-bearing core is isotropic $k_h/k_v \approx 1$ at low-stress conditions, suggesting effects to permeability anisotropy from stratification or particle shape for these two tested cores are indistinguishable in the absence of effective stress. However, permeability anisotropy increases exponentially with effective vertical stress, as described by $\frac{k_h}{k_v} = \alpha\left(\frac{\sigma_v}{1MPa}\right)^{\beta}$ with α = 1.6, β = 0.22 for the seal core and α = 3, β = 0.5 for the hydrate-bearing core.
- At near in situ effective vertical stresses of ~2 MPa, the permeability anisotropy is approximately k_h/k_v = 1.86 for the seal core and k_h/k_v = 4.24 for the core from the gas hydrate reservoir layer, assuming a hydrate saturation S_h = 0.8. The results

imply that measured permeability from permeameter tests (for both pressure and conventional cores) along the vertical direction may underestimate the reservoir's flow performance, which is mainly horizontal (radial) during gas production from a vertical well.

- Effective stress increases have irreversible effects on permeability reduction, yet permeability anisotropy k_h/k_v during unloading follows the same trend as during loading for the hydrate-bearing core.
- The presence of gas hydrate in sediments increases the air-entry pressure and residual water saturation but decreases m-value resulting in a steeper water retention curve.
- The distributions of available pore spaces for flow in the core with (S_h = 0.8) and without (S_h = 0) THF hydrate, inferred from water retention curves, follow a lognormal distribution. Hydrate formation in the core decreases the apparent mean pore size from ~10 μm to ~2 μm, without evidently changing the distribution's standard deviation. THF hydrate preferentially forms in larger pores.
- Gas hydrate dissociation changes the intrinsic permeability K_{int}, reflecting the intricate interplay among in situ stress before hydrate dissociation, pore pressure drop during hydrate dissociation, and additional shear stress caused by hydrate dissociation. Gas hydrate dissociation increases the effective permeability K_{hyd} and the relative permeability to gas k_{rg}, which is affected by two processes that have competing effects, i.e., hydrate saturation decrease lowers the entire relative permeability curve, but the gas saturation increase shifts k_{rg} to higher values along the curve of relative permeability to gas, and the latter process dominates.

CHAPTER 6 MORPHOLOGY AND PHYSICAL PROPERTIES OF TETRAHYDROFURAN HYDRATE IN CLAYEY SEDIMENTS

6.1 Introduction

Gas hydrates in sandy deposits are considered to be the most favorable for future gas production (Boswell, 2009, Boswell and Collett, 2011). However, vast (over 90% of the global hydrate mass) but highly dispersed marine gas hydrates are found in fine-grained (i.e., silty and clayey) sediments (Boswell and Collett, 2006), implying that the hydrate-bearing, fine-grained sediments are essential in the future study of gas production as a natural energy source. The research on hydrate-bearing fine-grained sediments in the production of natural gas has not been fully explored as a result of the limitations in experiments conducted to explore the synthesis of gas from hydrate-bearing fine-grained sediments, such as clays and diatoms, as they occur in nature (Lei, 2017, Lei and Santamarina, 2018).

Gas hydrates grow in natural sediments by filling the pores and/or segregating the sediment grains and are governed by the skeleton and capillary forces at particle level during hydrate crystal growth (Clennell et al., 1999, Dai et al., 2012). For fined-grained sediments that possess high capillarity, there is segregation of gas hydrates forming interconnected networks that occur naturally, such as in the Krishna-Godavari Basin (Collett et al., 2008, Rees et al., 2011) and the Ulleung Basin (Yun et al., 2011). Segregated gas hydrates in natural clayey sediments manifest in nodules, chunks, and veins, as revealed by X-ray computed tomography (CT) (Rees et al., 2011, Schultheiss et al., 2006, Yun et al., 2011). These hydrates increase the heterogeneity of sediments and complicate

the interpretation of physical measurements, such as electrical resistivity (Cook et al., 2010, Cook et al., 2012) and seismic imaging (Lee and Collett, 2009, Riedel et al., 2010).

Fine-grained sediments are characterized by small-sized pores, low diffusion rates and a high specific surface (Dai and Santamarina, 2017, Lei, 2017). Although dispersed clay particles in suspensions may serve as hydrate nucleation sites (Cha et al., 1988), and clay mineral surface can serve as part of the methane hydrate clathrate structure as revealed in molecular dynamics simulations (Cygan et al., 2004, Park and Sposito, 2003, Sposito et al., 1999), the extremely small pore sizes in natural clayey sediments lead to prevailed capillarity and reduced water activity, which hinder hydrate formation (Clennell et al., 1999, Handa and Stupin, 1992, Henry et al., 1999). Experiments conducted to facilitate the formation of methane hydrates in laboratories have been limited by low methane solubility and extremely time-consuming diffusion transport and lens growth processes. Several strategies have been employed to synthesize segregated hydrates in kaolinite and diatoms using carbon dioxide gas (Lei and Santamarina, 2018).

The physical and mechanical properties of hydrate-bearing clays have been investigated using tetrahydrofuran and ice analogs. Published experimental studies of THF hydrate-bearing clays have covered physical, mechanical, thermal, and electromagnetic properties (Cortes et al., 2009, Lee et al., 2010a, Lee et al., 2010b, Yun et al., 2007, Santamarina and Ruppel, 2010), although without fully recognizing the segregated, anisotropic, and heterogeneous nature of the hydrate in clayey sediments or attributing morphology effects to measured properties. There are fundamental differences in the processes of nucleation, growth, and dissociation between the natural hydrates and the THF

hydrate in clayey sediments. However, the formed crystals in the analogs are similar to the fracture morphology and heterogeneity hydrates in clay, as the underlying physical processes in the analogs are also governed by capillarity, cryogenic force, and stress state. Thus, they are suitable alternatives to the static characterization of hydrate-bearing clays, particularly for studying the effects of hydrate morphology on the fundamental properties of hydrate-bearing clays.

This study aims to explore the underlying physics of the formation of interconnected hydrates in clays in a laboratory, as well as the ensuing effects of hydrate morphology on the physical properties of hydrate-bearing clays. Here, we form THF hydrates in kaolinite clay in a laboratory, use X-ray CT to visualize the three-dimensional hydrate distribution and morphology, and deploy *P*- and *S*-waves to characterize the elastic and dynamic properties of hydrate-bearing clayey sediments. The results are expected to provide a comprehensive understanding of the nucleation and distribution of THF hydrate in clays. In addition, the results are used to reveal the advantages and disadvantages of using this analog method in the laboratory to investigate natural clay hydrates.

6.2 Experimental Design

6.2.1 Specimen Preparation

The tested specimens are made by mixing kaolinite clay and stoichiometric THF-water solution. The grain diameter of kaolinite is d_{50} of 1.1 μm specific surface area S_s of 36 m^2/g, specific gravity G_s of 2.6, and liquid limit LL of 60%. The stoichiometric THF-water solution contains a 19THF:81H_2O mass ratio makes it possible for the highest possible conversion to be attained for THF-water solution into THF hydrate, which is

approximately 95% of the bulk solution (Strauch et al., 2018). This THF-water solution is added into kaolinite with three different solution-clay mass ratios: R_m = 0.5:1, 0.6:1, and 0.7:1. After being mixed in plastic bags, the THF-water-kaolinite paste is packed in a customized aluminum testing chamber.

6.2.2 Experimental Setup

The inner diameter of the cylindrical aluminum testing chamber is 20.32 mm with a thickness of 1.6 mm and a height of 40 mm. The top and bottom parts inside the testing chambers are made Teflon pedestals, equipped with piezo pads and bender elements for *P*- and *S*-wave measurements. The piezo materials (PSI-5A4E from Piezo Systems, Inc.) are cut into the desired geometry (i.e., 5 mm in diameter for piezo pads, 3 mm in width for bender elements, and both are 0.66 mm in thickness) and soldered with mini-coaxial cables (8700 coax miniature, Belden). They are electrically grounded using pure silver paint (SPI Supplies) and then installed onto the Teflon pedestals and covered by high-strength epoxy. The top pedestal is spring-loaded to apply constant vertical stress of 10 kPa throughout the entire course of the tests. Both the top and bottom pedestals also have K-type thermocouples to monitor the temperatures within the cylinder during the test, which are controlled by a walk-in refrigerator (a Darwin environmental chamber with ±0.1°C precision), to trigger the formation of THF hydrate (and also for hydrate dissociation at the end of the test). Once hydrate is formed, the specimen within the aluminum chamber is visualized using a micro-focus X-ray CT scanner. During scanning, the specimens' temperatures are maintained constantly at 1°C (note that THF hydrate stability temperature

for 19THF:81H_2O mixture is 4.4°C at atmospheric pressure) by circulating anti-freezing polyethylene glycol through Tygon tubes wrapped around the aluminum chamber.

6.2.3 Experimental Procedures

Dry kaolinite is mixed with stoichiometric THF-water solution in predetermined mass ratios within a sealed plastic bag. The mixture is then scooped into the aluminum chamber, and constant vertical stress of 10 kPa is applied through the spring-loaded top pedestal throughout the test. After connecting all sensors (i.e., piezo crystals and thermocouples), the entire setup is placed within the environmental chamber, where the temperature is set at −10°C. THF hydrate formation is triggered by cooling. The temperature evolution within the specimens is monitored through the embedded thermocouples. Once hydrate formed, the chamber temperature is raised to 1°C, and the specimen is kept under this temperature for further nucleation to complete. Approximately 10 hours after initial hydrate nucleation, the specimen is scanned using the micro-focus X-ray CT to obtain the morphology of THF hydrate in kaolinite. Finally, the hydrate is dissociated by raising the temperature to 20°C. Both *P*- and *S*-waves are continuously measured during the cooling, hydrate nucleation, and hydrate dissociation processes.

6.3 Experimental Methods, Data Reduction, and Experimental Results

6.3.1 Temperature Signatures during Hydrate Formation

Figure 6.1 illustrates the temperature evolution of two specimens throughout the entire course of the testing. These specimens have identical compositions (i.e., 0.7 solution:1 kaolinite by mass) but different subcooling temperatures T_{sc} at which hydrate

nucleation initiates. The induction time of THF hydrate formation is inherently random. Hydrate formation may occur at any moment during cooling as long as the specimen's temperature is lowered below the THF hydrate nucleation temperature, which is ~4.4°C at atmospheric pressure for the stoichiometric 19THF:81H_2O solution. Once a thermal spike is observed indicating hydrate formation, the environmental chamber temperature is raised to 1°C and kept under this condition for later X-ray CT scanning approximately 10 hours after the thermal spikes are being observed.

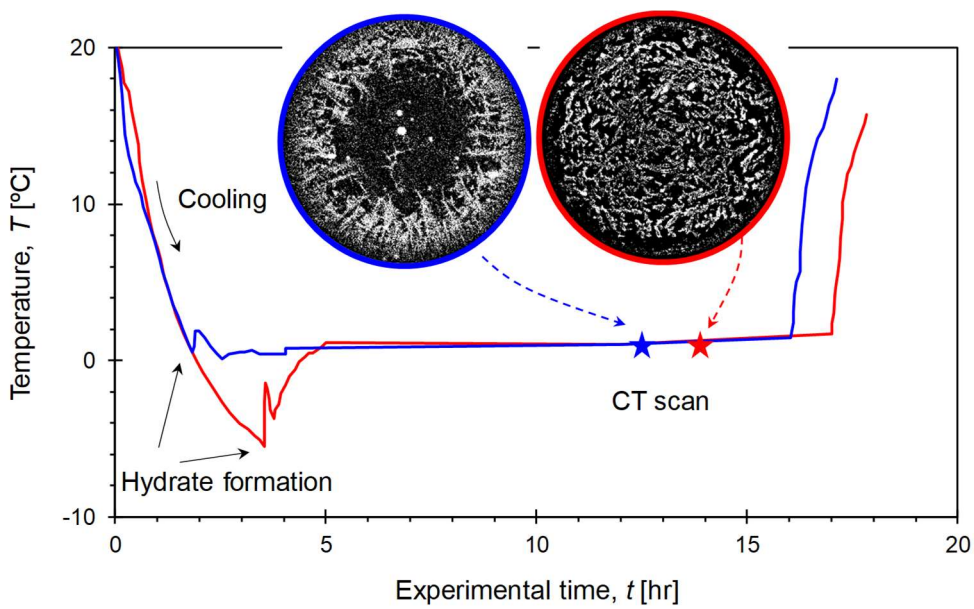

Figure 6.1 − Temperature signatures of two specimens with identical (stoichiometric tetrahydrofuran-water) solution-kaolinite mass ratio (R_m = 0.7:1, in this case) during the whole course of the tests. The environmental chamber is initially set at −10°C. Stochastic hydrate nucleation occurs randomly at different subcooling temperatures T_{sc}. X-ray CT is taken approximately 10 hours after hydrate nucleation. The chamber temperature is then raised back to room temperature to cause hydrate dissociation.

The inset images in Figure 6.1 show slice views of the X-ray CT scans of the two corresponding specimens, with the white phase representing the hydrate phase. The results show that specimens with similar compositions are likely to end up with very different hydrate morphologies under different thermal histories. The specimen that experienced a lower subcooling (T_{sc} = 4.4°C, i.e., the temperature at which nucleation initiates is ~0°C as shown in the blue curve in Figure 6.1) tends to have hydrate distributed near the core-periphery boundaries, while the one that experienced a higher subcooling temperature (T_{sc} = 8.2°C; the red curve in Figure 6.1) has hydrate distributed relatively uniformly across the whole cross-section of the core. The following session explains the details of CT imaging and image processing.

6.3.2 Volume Fraction of THF Hydrate in Clayey Sediments

The micro-focus X-ray CT scanner used in this study has a micro-focus X-ray source (Thermo Scientific PXS10) and a Varian PaxScan1313 detector with a 127 μm pixel pitch and 1,024×1,024 pixels. The specimens are scanned using a 120 kV voltage and a 70 μA current. Each CT scan takes 35 minutes, with three frames per second and 1,800 projections in total. The obtained scanning images have a resolution of 20 μm in this study, which is 203 μm^3 voxel in the volume.

Figure 6.2 illustrates the image processing used to separate the hydrate phase from the clayey matrix. Since the formed THF hydrate in clayey sediments is segregated and the two have different densities (i.e., hydrate ρ_h = ~0.9 g/cm^3 and the bulk clay matrix ρ_{kao} = ~1.5 g/cm^3), the histograms of the CT images are bimodal, as shown in Figure 6.2a. The inset slice view is the corresponding raw CT image in grayscale, normalized into 8 bits

(i.e., gray values vary between 0 and 255). An overestimation of the hydrate phase using a threshold pixel value of PV = 104 (Figure 6.2b) and an underestimation using PV = 115 (Figure 6.2c) result in hydrate volume fractions VF_h of 0.22 and 0.20, respectively. After thresholding, the hydrate veins are marked in white and the clay matrix in black in binary images. This result demonstrates that the different hydrate phases can be determined with the help of CT scan images with an accuracy of ±0.01 in volume fraction.

At this point, attention must be paid to the definition of hydrate saturation S_h in clayey sediments. Hydrate saturation can be defined as the ratio of the hydrate volume over the pore volume if hydrate is a pore constituent as in sandy sediments. However, this definition is not applicable to the case of hydrate-bearing clays as the hydrate crystals tend to segregate and no longer manifest as a pore-occupying component. Thus, the hydrate saturation in clayey sediments should be defined as the volume of hydrate over the total volume of the specimen, that is, the volume fraction VF_h described herein.

The distribution and morphology of the formed THF hydrate (recolored in cyan using ImageJ) in specimens with three different initial solution-clay mass ratios R_m are illustrated in Figure 6.3. For each mass ratio, specimens with two different subcooling temperatures and the resulted hydrate volume fractions are presented. The results demonstrate that although started with identical mass compositions, the formed hydrates may vary significantly in volume and morphology as they are affected by the specimens' temperature histories. The specimens that experience more significant subcooling temperatures (i.e., lower absolute temperatures at which hydrate nucleation initiates) tend to have more uniformly distributed hydrate and slightly larger hydrate volume, while the specimens that

experience lower subcooling temperatures tend to result in preferential hydrate formation at core boundaries with lower hydrate volume fractions. This result demonstrates that THF hydrate can be an expedited and convenient analog in a laboratory to study natural hydrate-bearing clayey sediments, but that this depends on the quantification of the hydrate volume (or saturation). Unless directly visualized, for instance, using X-ray CT and nuclear magnetic resonance imaging, or indirectly estimated based on thermal signatures during hydrate nucleation, the volume of the formed hydrate in clayey sediments cannot be determined solely based on the amount and the initial mass ratio of THF and water in the system.

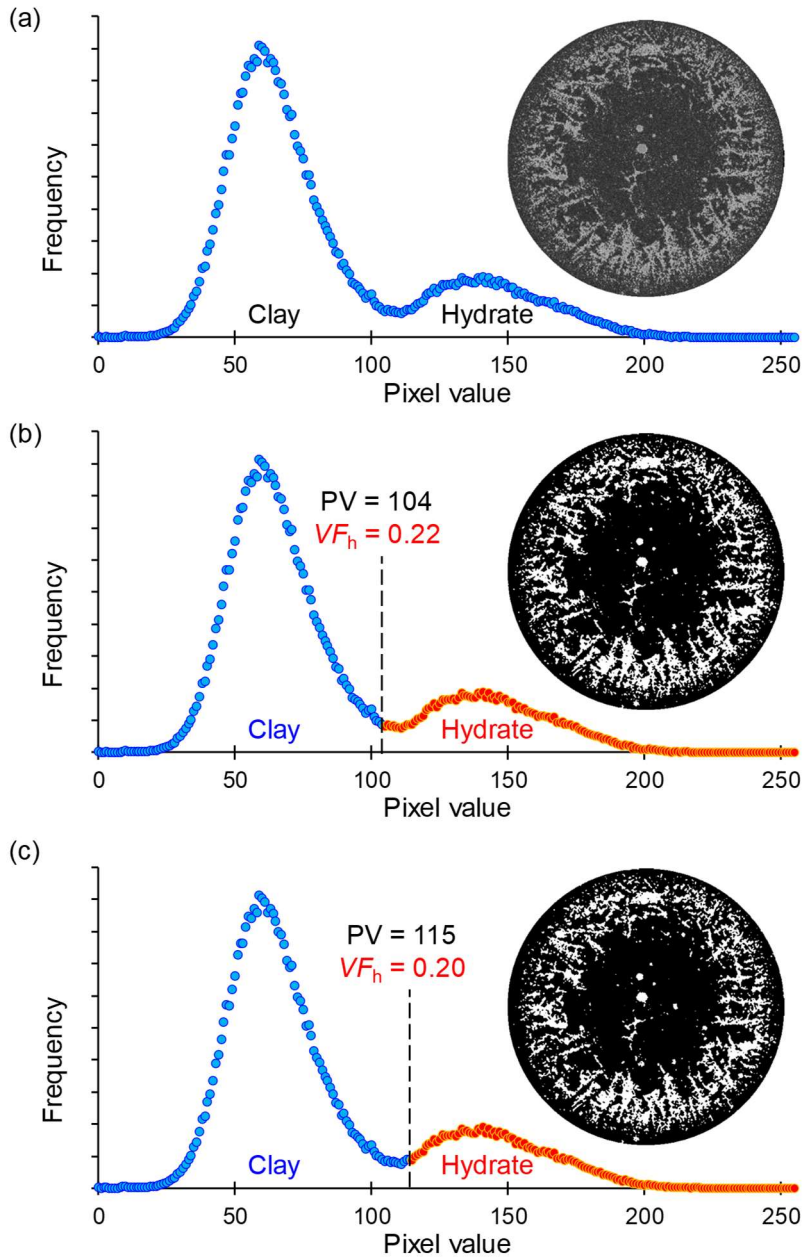

Figure 6.2 − X-ray CT image processing. (a) The histogram of a raw CT image (inset, converted into an 8-bit grayscale image) is bimodal, and the two humps represent the clay and hydrate phases, respectively. (b) An overestimation of the hydrate phase using a threshold pixel value *PV* of 104 results in a hydrate volume fraction VF_h of 0.22. The inset CT slice view presents the corresponding binary image with the hydrate phase shown in white and the clay phase in black. (c) An underestimation of the hydrate phase using a threshold pixel value *PV* of 115 results in a hydrate volume fraction VF_h of 0.20.

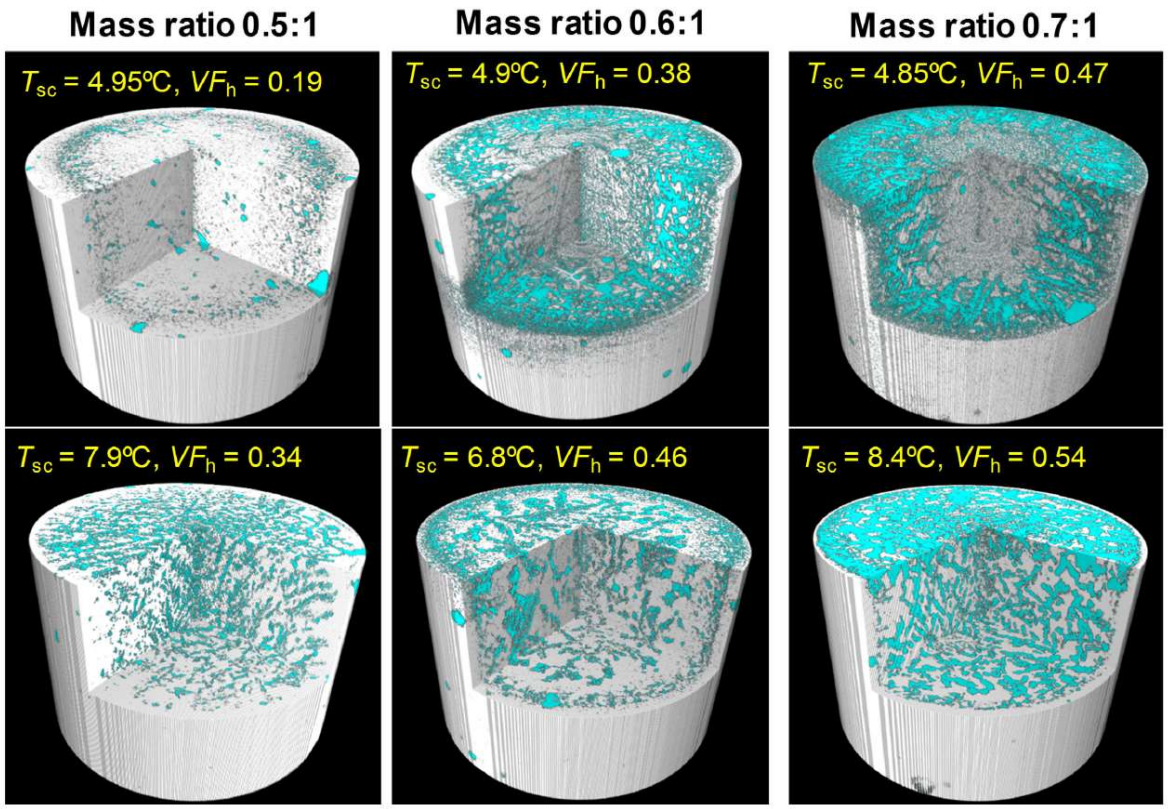

Figure 6.3 − 3D X-ray CT scans reveal tetrahydrofuran hydrate (recolored in cyan) in kaolinite clay. For specimens with identical solution-kaolinite mass ratios, their thermal histories affect the saturation and morphology of hydrate in kaolinite. Note: T_{sc} is the subcooling temperature and VF_h is the hydrate volume fraction calculated from the CT results.

6.3.3 Compressional and Shear Wave Velocities

P- and *S*-waves are obtained throughout the cooling, hydrate formation, and hydrate dissociation processes. Both the square and sinusoidal waves have a frequency of 20 kHz and an amplitude of 10 volts, produced by a generator (Agilent 34970A) as the source signal for the measurement of the *P*- and *S*-waves, respectively. The received wave signals are filtered (Krohn-Hite 3361) with a high pass of 500 Hz and a low pass of 1 MHz and are recorded and stored using an Agilent DSOX2004A oscilloscope.

Figure 6.4a shows the chronological wave cascades collected throughout the test for a specimen with a solution-kaolinite mass ratio R_m = 0.6:1. The horizontal axis shows the wave travel time, and the vertical axis shows the received *P*- and *S*-waveforms cascading from the cooling to the hydrate formation, as well as to the hydrate dissociation stages. The wave signatures are then normalized by use of their maximum amplitudes and then indicated by color with blue for peaks and yellow for valleys. On top of each wave cascade is the first waveform collected at the beginning of the test. The first deflection point, indicated by the circle, is selected as the first arrival time (Abbiss, 1981, Viggiani and Atkinson, 1995). The first arrival times of consecutive signals (indicated by dashed lines) are determined through cross-correlation calculation in reference to the first signal.

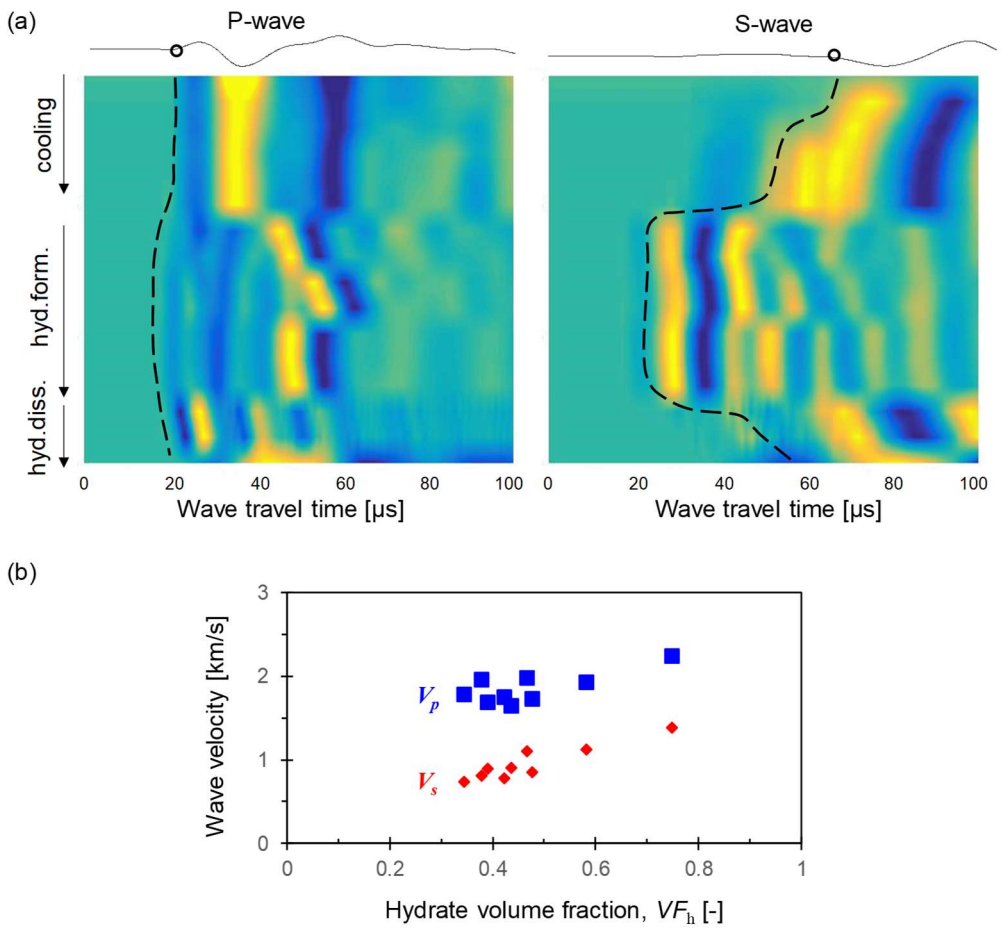

Figure 6.4 − Wave velocities of hydrate-bearing clays. (a) Chronological wave cascades throughout the tests. The figures show the collected *P*- and *S*-waves in a specimen with a solution-kaolinite mass ratio R_m of 0.6:1 during the cooling, hydrate formation (hyd. form.), and hydrate dissociation (hyd. diss.) stages. Dashed lines indicate the first arrival time. (b) *P*- and *S*-wave velocities as functions of the bulk hydrate volume fraction VF_h in the tested specimens.

During the cooling stage, there is no significant change in *P*-wave velocity V_p = ~1.54 km/s, which is mainly governed by the velocity of the water. However, a slight increase in the *S*-wave velocity V_s from ~260 to ~300 m/s is observed, indicating changes in the sample's effective stress during cooling, yet the cause of this is unidentified. As hydrate nucleation initiates (indicated by thermal spikes in the temperature signature), increases in

both V_p and V_s are observed, which are associated with increased wave frequencies. Hydrate dissociation lowers both V_p and V_s. After hydrate dissociation and the specimen's temperature returns to room temperature, V_p remains nearly identical to its measurement at the beginning of the test, but V_s is slightly faster than before the hydrate formation, suggesting that hydrate formation and dissociation can cause a certain irreversible increase in skeleton stiffness, possibly due to localized consolidation.

Figure 6.4b summarizes the measured V_p and V_s as a function of bulk hydrate volume fraction VF_h from CT imaging in all tested specimens. Increased hydrate volume in clayey sediments generally increases both *P*- and *S*-wave velocities, and the increase in V_s due to increased VF_h is slightly more evident than in V_p.

6.3.4 Wave Attenuation in Hydrate-Bearing Clayey Sediments

Collected wave signatures show that increased wave velocity due to hydrate formation is associated with decreased wave amplitude, implying increased wave attenuation. The value of wave attenuation Q^{-1} (i.e., the inverse of quality factor Q) can be quantified using the following (Toksöz et al., 1979):

$$Q^{-1} = \frac{V}{\pi l}\gamma \tag{6-1}$$

where V is the wave velocity, l is the length of the wave travel path (i.e., specimen height), and γ is the ratio of the slope of the logarithmic frequency spectrum of the tested specimen over that of a reference aluminum rod with identical geometry to the specimen, which can be calculated by the spectral ratio method (Toksöz et al., 1979). Specifically, Fourier

transform of the wave signals of the specimen and the reference aluminum rod is implemented to obtain their frequency spectra (Figure 6.5a). This result is then replotted in terms of the natural logarithmic ratio of the spectrum of the aluminum rod over that of the tested specimen, and the corresponding slope is $\gamma = \gamma_{spec} - \gamma_{alu}$ (Figure 6.5b). Since the quality factor Q of aluminum is approximately 120,000–250,000 (Zemanek Jr and Rudnick, 1961), taking $\gamma_{alu} = 0$ introduces an error of less than 1%, and thus, the constant γ_{spec} for the tested specimens can be exactly equal to the slope value γ in Figure 6.5b.

Figure 6.5c summarizes the attenuation of the *P*- and *S*-waves (i.e., Q^{-1}_p and Q^{-1}_s) as a function of the hydrate volume fraction in tested hydrate-bearing kaolinite specimens. Note that the hydrate volume fraction used in this plot is a bulk value of the whole specimen and does not necessarily reflect the hydrate volume fraction along the wave travel path. The results show that the attenuation of both *P*- and *S*-waves increase with increased hydrate volume in the clayey sediments, and the presence of hydrate attenuates *P*-waves more evidently than *S*-waves.

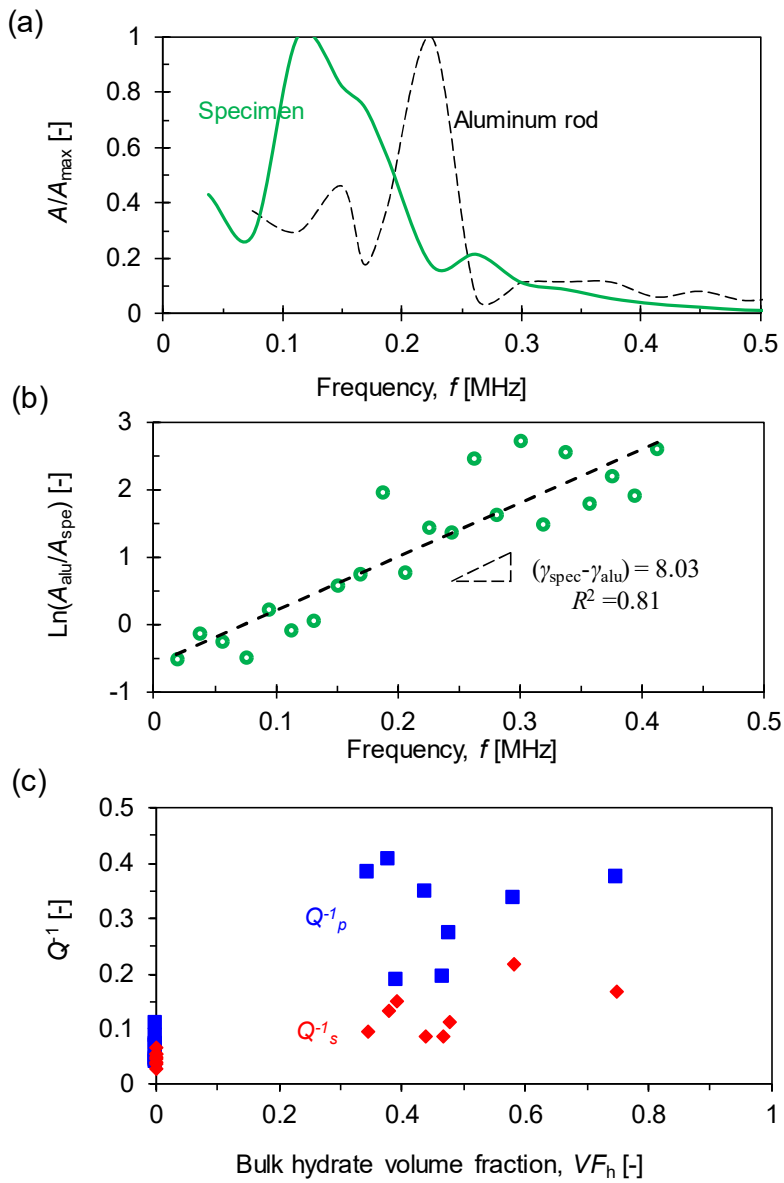

Figure 6.5 − The spectra ratio method and wave attenuation. (a) The frequency spectra of a tested specimen and a reference aluminum rod with identical geometry to the tested specimen. (b) The natural logarithmic amplitude ratio of the frequency spectra. (c) The attenuation (Q^{-1}) of *P*- and *S*-waves in tested hydrate-bearing kaolinite.

6.4 Analyses and Discussion

6.4.1 Hydrate Formation and Morphology – A Multiphysics Coupled Process

Figure 6.6a summarizes the bulk hydrate volume calculated from the CT results in all tested specimens at different initial solution-clay mass ratios R_m. The final volume fraction of formed hydrate VF_h in kaolinite increases with the subcooling temperature T_{sc} in specimens with the solution-clay mass ratios R_m of 0.5 and 0.6. For the specimens with $R_m = 0.7$, the final hydrate volume fraction VF_h does not monotonically increase with the subcooling temperature T_{sc}, and the specimen in which hydrate nucleation occurs with a subcooling $T_{sc} = 4.6$°C renders the highest $VF_h = 0.75$. However, as revealed by X-ray CT scanning, all specimens with high hydrate volume fractions tend to have a relatively uniform hydrate distribution, while the specimens in which hydrate accumulates preferentially at the core-periphery and grows inward in a dendritic pattern have relatively lower hydrate volume fractions (refer to Figure 6.3). The following underlying mechanisms govern these phenomena:

- Hydrate nucleation is inherently spontaneous and appears to be random in induction time, affected by the thermal history, physical properties, impurities, and mechanical agitation of the solution (Dai et al., 2014, Mullin, 2001). Thus, the location and the induction time (or subcooling temperature Tsc) of hydrate nucleation initiation are unpredictable. Once hydrate forms, continued formation tends to sustain the growth of existing hydrates rather than nucleating at new sites.
- The specimens are initially prepared at room temperature (~20°C) and then placed inside the environmental chamber with a temperature set at −10°C. Thus, the

temperature at the core boundary first drops to the hydrate phase equilibrium temperature (i.e., ~4.4°C at atmospheric pressure), while the temperature at the core center takes a certain amount of time, depending on the size and thermal diffusivity of the specimens, to reach the hydrate equilibrium temperature. Therefore, for specimens in which hydrate nucleates at a higher subcooling temperature T_{sc} (i.e., a longer cooling time), the temperature throughout the specimen falls below the hydrate phase equilibrium temperature, providing the possibility of hydrate nucleation across the whole specimen after a long induction time. However, for the specimens in which hydrate nucleates at a lower subcooling temperature, the temperature at the core-periphery drops to the phase equilibrium temperature slightly earlier than in the central zone of the core. This can lead to preferential hydrate formation only at the core-periphery. The reasons for the lack of further hydrate growth in the central part of the specimen are unclear. Presumably, volume expansion caused by hydrate formation can induce additional stress in the clay matrix, which may inhibit hydrate nucleation in the central part of the specimens.

- Continued hydrate crystal growth depends on the transport of water and THF. For kaolinite with a consolidation coefficient C_v of ~10^{-7}–10^{-8} m^2/s, the time for water to be extracted from the core center to the periphery (i.e., $r = 1$ cm) ranges between several tens of minutes and a few hours (i.e., estimated by $t \approx r^2/C_v$). Thus, the hydrate that initially forms at the core-periphery may also be constrained by solution transport.
- The kaolinite used in this study has a liquid limit of LL = 60%, that is, approximately 60% by weight of water needs to be added to the kaolinite to change

the clay from plastic to liquid state. Added water with a content that is less than the liquid limit tends to be retained on the clay surface; after hydrate formation consumes a certain amount of free water, the residual water becomes less active to be contributable to sustain hydrate crystal growth, with additional impediments of the further consolidation of the clay matrix and the potentially high capillarity if an unsaturated condition occurs.

- Other than heat transfer and mass migration, hydrate nucleation and growth are associated with crystal volume expansion and capillarity change that may lead to localized consolidation and pore pressure variation, which in turn impacts further heat and mass transfer and crystal growth. Our current knowledge of these processes for a clayey system remains in its infancy.

Assuming all of the stoichiometric THF-water solutions can be converted into hydrate and without considering localized consolidation due to hydrate formation, the maximum hydrate volume fractions $VF_h^{\max}$ are 0.67, 0.81, and 0.94 in the specimens with solution-clay mass ratios of R_m = 0.5, 0.6, and 0.7, respectively. The maximum hydrate saturation can be calculated as follows:

$$VF_h^{\max} = \frac{V_h}{V_{kao}} = \frac{m_h}{m_{kao}} \frac{\rho_{kao}}{\rho_h} = R_m \frac{\rho_{kao}}{\rho_h} \tag{6-2}$$

where m and ρ are mass and density and subscripts kao and h represent kaolinite (bulk matrix) and hydrate. The bulk density of kaolinite is computed assuming a void ratio of e = 1.19 under effective stress of σ' = 10 kPa, according to the following :

$$e = e_{100} - C_c \log\left(\frac{\sigma'}{100kPa}\right) \tag{6-3}$$

where the reference void ratio e_{100} = 0.9 at 100 kPa effective stress and the compressibility coefficient C_c = 0.29 for kaolinite clay (Burland, 1990). The actual hydrate conversion ratio ranges from 0.3 to 0.8 in all tested specimens based on X-ray CT results, with a majority of the specimens having a hydrate conversion ratio between 0.4 and 0.7 (Figure 6.6b). Therefore, aside from the innate heterogeneity of the stoichiometric solution that prevents the full conversion of THF hydrate in bulk solution (Strauch et al., 2018), hydrate nucleation and growth in kaolinite are severely constrained by water activity and solution transport.

Admittedly, the effective stress state during nucleation, which affects the clay pore size and thus the capillarity in the system that governs the transport, is not considered in this study. The observed hydrate morphology, as well as the ensuing physical properties described herein, may be subject to change under higher confining stresses.

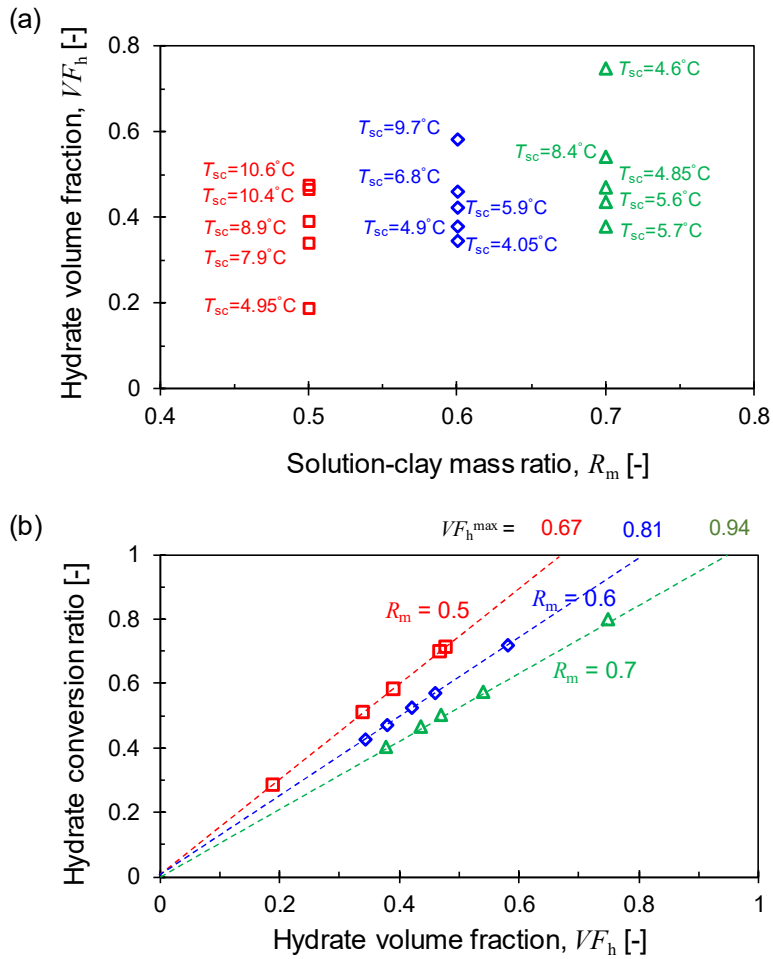

Figure 6.6 – The hydrate volume fraction VF_h in clayey specimens tested in this study. (a) Hydrate volume fraction VF_h in specimens with different initial (stoichiometric tetrahydrofuran-water) solution-clay mass ratios R_m and subcooling temperatures T_{sc}. (b) The hydrate conversion ratio in most of the tested clayey specimens ranges from 0.4 to 0.7.

6.4.2 Elastic Properties of Hydrate-Bearing Clays

The velocity of the waves through the hydrate-bearing clays tested in this study are a few kilometers per second and tens of kilohertz in frequency. Thus, the corresponding wavelength is in the decimeter scale, which is much larger than the characteristic

dimension of the hydrate lenses formed in the millimeter scale. Therefore, the waves propagate through these heterogeneous specimens as through a continuum. Due to segregated and disseminated hydrate distribution in kaolinite, the measured wave velocities reflect the lumped moduli of the material only along the wave propagation paths.

The solid markers in Figure 6.7 are measured *P*- and *S*-wave velocities as a function of the bulk hydrate volume fraction in the tested specimens, while the open markers use calibrated hydrate volume fractions along the wave propagation paths. Specifically, *P*-wave sensors are located in the center of the specimen, and a concentric cylindrical sub-core with a radius that is half of the sample radius is extracted from the 3D X-ray CT results to compute the calibrated hydrate volume fraction. Conversely, the *S*-wave sensors are located at the half-radius position, and thus, a sub-cored cylindrical zone with a radius that is half of the specimen's radius along the *S*-wave propagation direction is used to calculate the corresponding calibrated hydrate volume fraction for *S*-waves. The inset diagrams in Figure 6.7 illustrate the positions of piezo pads and bender elements relative to the specimen. For specimens in which hydrates preferentially accumulate at the core-periphery, the measured *P*-wave velocities reflect a clayey medium in the core center that contains a lower local hydrate volume fraction than the bulk hydrate volume fraction. In contrast, there is not an evident discrepancy between the calibrated hydrate volume fraction along the *S*-wave propagation path and that of the bulk hydrate volume fraction of the specimen.

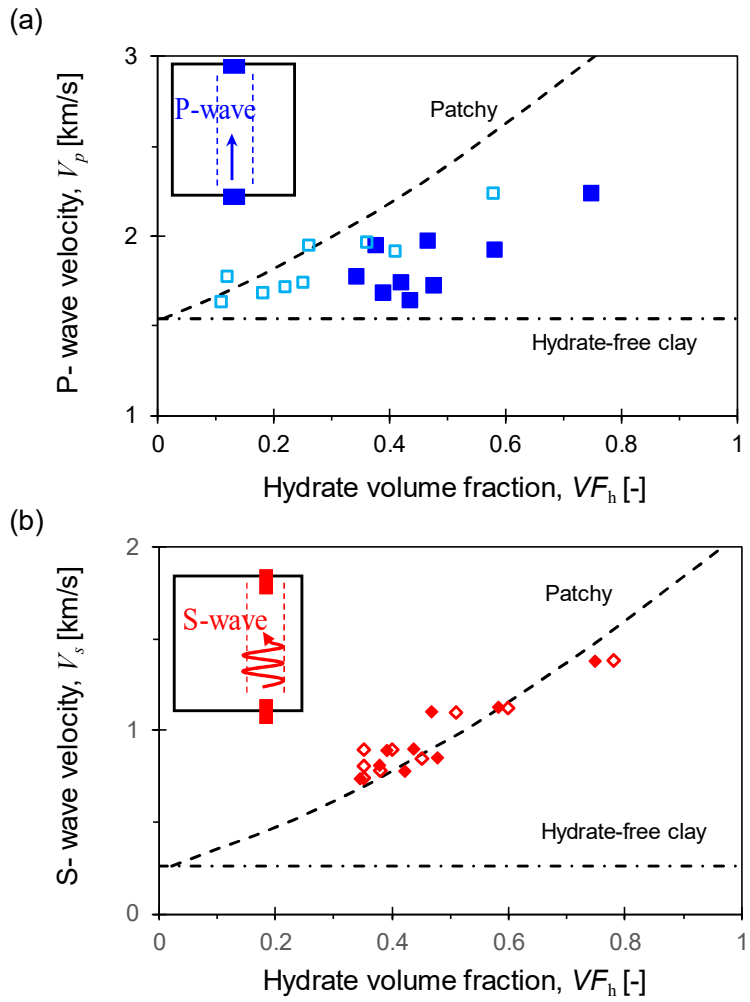

Figure 6.7 – Wave velocities of THF hydrate-bearing kaolinite. (a) *P*-wave velocity V_p. (b) *S*-wave velocity *Vs*. Solid markers indicate the bulk hydrate volume fraction of the specimens. Open markers correspond to the hydrate volume fraction in sub-cored cylindrical zones (from X-ray CT results) along the wave propagation paths. The two reference lines indicate the wave velocities of the hydrate-free clayey specimen and the patchy model predictions.

Together with the measured data, the velocities of the hydrate-free kaolinite and the kaolinite matrix containing patchy hydrate inclusions (noted as patchy in Figure 6.7) are calculated using the self-consistent method (Berryman, 1980). This method computes the effective macroscopic elastic constants of the inhomogeneous composite with two

endmembers: water-saturated hydrate-free kaolinite (V_p = 1,538 m/s and V_s = 260 m/s, as measured in this study) and pure THF hydrate crystals (V_p = 3,670 m/s and V_s = 1,890 m/s from (Helgerud et al., 2003). The computed results that consider spherical and needle-shaped inclusions do not show distinguishable differences, so only the results of kaolinite containing spherical hydrate patches are presented in Figure 6.7. The relationship between the measured wave velocity and the calibrated hydrate volume fraction can be accurately predicted by the self-consistent model.

In summary, the wave velocity of heterogeneous specimens reflects the stiffness of the material along the wave travel path, and the innate heterogeneity in hydrate-bearing clays creates challenges in the wave velocity-based characterization of such specimens. Additionally, the self-consistent model can predict the bulk elastic properties of hydrate-bearing clays. Other often-used rock physics models that consider different hydrate pore habits are invalid because segregated hydrate crystals are inclusions in the clayey matrix rather than being pore constituents.

6.4.3 Attenuation in Hydrate-Bearing Clays

The *P*- and *S*-wave attenuation results of using a calibrated hydrate volume fraction are shown in Figure 6.8, together with the results of laboratory synthesized hydrate-bearing sands using resonant column testing (Priest et al., 2006), natural hydrate-bearing sediments from the Mallik 2L-38 research well using sonic logs (Guerin and Goldberg, 2002), and THF hydrate crystals using ultrasonic waves (Pohl et al., 2018). The results agree with the previous finding that higher hydrate saturation generally increases specimens' stiffness and wave attenuation.

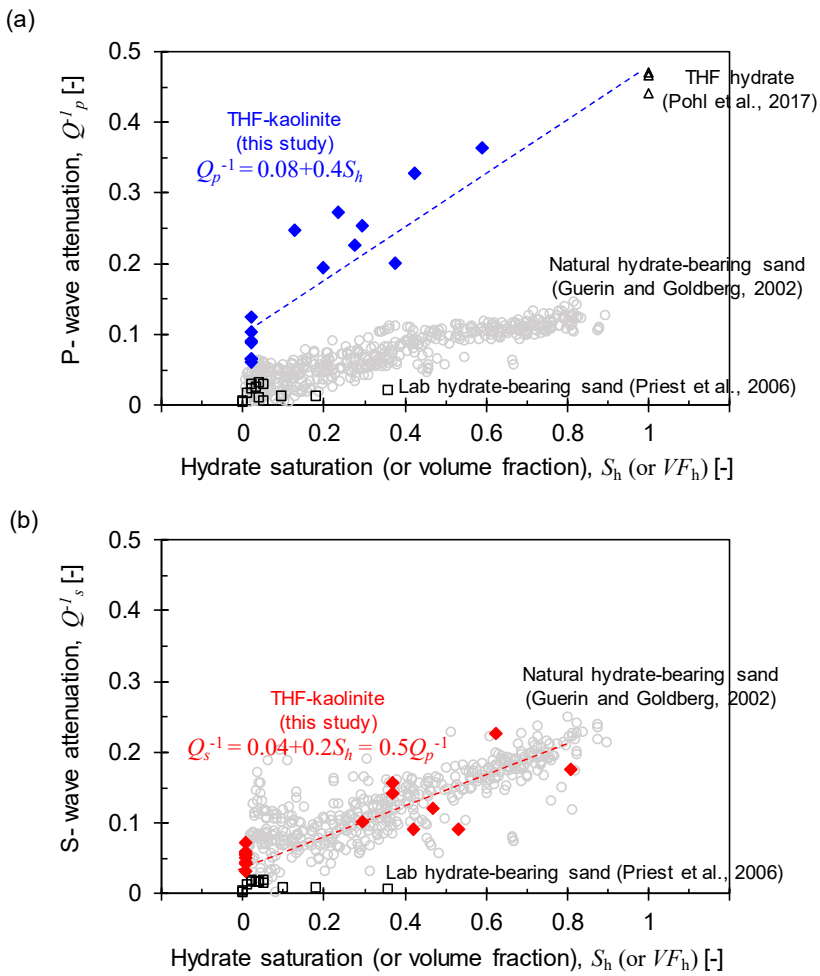

Figure 6.8 − Wave attenuations in hydrate-bearing kaolinite (noted as solid diamonds). (a) *P*-wave attenuation Q^{-1}_p. (b) *S*-wave attenuation Q^{-1}_s. Wave attenuation in the following specimens is included for comparison: laboratory-synthesized methane hydrate-bearing sands, natural hydrate-bearing sands at the Mallik site, and laboratory-formed tetrahydrofuran (THF) hydrate crystals.

Pure THF crystal has a relatively high *P*-wave attenuation Q^{-1} = ~0.45, possibly caused by the viscous squirt flow of unconverted water within the hydrate crystals (Pohl et al., 2017). This value is much higher than that of the water-saturated clays with Q^{-1} = ~0.1, as measured in this study (Figure 6.8a). Additional loss mechanisms in hydrate-bearing sediments may attribute to microsquirt among hydrate crystals, submicrosquirt flow due to

inclusions of air and water in hydrate, or gas bubble resonance (Marín-Moreno et al., 2017). The *P*-wave attenuations of all tested specimens increase with hydrate volume fraction and can be fitted by the following:

$$Q_p^{-1} = 0.08 + 0.4VF_h \tag{6-4}$$

This result highlights the dominant role of hydrate crystal in the *P*-wave attenuation of hydrate-bearing clays. Due to the segregated nature of THF hydrate inclusions in clays, the measured wave attenuation of hydrate-bearing clays becomes a volume fraction weighted average of the attenuations of the clay matrix and the THF hydrate crystal.

Similarly, the *S*-wave attenuations of hydrate-bearing clays also increase with hydrate volume fraction (Figure 6.8b) as follows:

$$Q_s^{-1} = 0.04 + 0.2VF_h \tag{6-5}$$

which is approximately half of the *P*-wave attenuation. This agrees with the attenuation results for partially saturated rocks (Mavko and Nur, 1979) but contradicts the findings for natural hydrate-bearing sands, which show slightly more significant attenuation in *S*-waves than in *P*-waves (Guerin and Goldberg, 2002), implying the existence of gas in the tested hydrate-bearing clays that have evident damping in *P*-waves. The physical causes of wave attenuation by intergranular friction, viscous squirt flow, and the coexistence of free gas in hydrate-bearing sediments are intricate. Nevertheless, the linear increase in wave attenuation with hydrate volume fraction highlights the critical role of hydrate crystal in

wave damping and demonstrates the potential of using a wave attenuation based method to quantify the hydrate volume in clayey sediments.

6.5 Conclusions

This study uses X-ray CT and wave measurements to visualize the distribution and morphology of THF hydrate in kaolinite, explore the underlying physics of hydrate formation in fine-grained sediments, and enhance the wave-based characterization of hydrate-bearing clays.

Hydrate formation in fine-grained sediments is innately segregated and heterogeneous. The traditional definition of hydrate saturation as the volume ratios of hydrate over the pore space is not applicable in clays. Since the manifestation of hydrate in kaolinite appears to be crystal inclusions embedded within the relatively homogenous clayey matrix, it is more reasonable to describe hydrate saturation using the volume fraction of hydrate over the specimen's total volume for hydrate-bearing clays.

The nucleation and growth of THF hydrate in kaolinite in a laboratory are dominated by the thermal condition and constrained by water and mass transport, which can result in low conversion ratios from stoichiometric solution to hydrate. As all tested specimens are cooled from the core boundaries inwardly, the specimens that undergo longer induction times result in disseminated hydrate nodules and veins across the whole specimen, while those that undergo shorter induction times result in preferential hydrate accumulation at the core-periphery in dendritic patterns and with relatively lower hydrate saturation. Estimation of THF hydrate saturation in clayey sediments based only on the stoichiometric THF-H_2O ratio can be erroneous and, more specifically, result in overestimation.

Wave velocity reflects the stiffness of materials along the wave travel path only. The innate heterogeneity in hydrate-bearing clays imposes challenges in the wave velocity based characterization of such specimens. The bulk elastic properties of hydrate-bearing clays can be accurately predicted using the self-consistent model. Other often-used rock physics models that consider different hydrate pore habits are invalid, as segregated hydrate acts as inclusions in the clayey matrix rather than being a pore constituent.

Clayey specimens with higher THF hydrate saturations have higher wave attenuations, highlighting the dominant role of THF hydrate in wave attenuation. Measured wave attenuations of hydrate-bearing kaolinite in this study show that $Q_p^{-1} = 0.08 + 0.4VF_h = 2Q_s^{-1}$. The increase in wave attenuations with hydrate volume fraction demonstrates the potential of using wave attenuation based methods to evaluate hydrate saturation in clayey sediments.

CHAPTER 7 CONCLUSIONS AND FUTURE WORK

7.1 Conclusions

The purpose of this research is to explore the changes in the mechanical, physical, and hydraulic properties of hydrate-bearing specimens under various applied stress levels, particularly under high stress. The scope of this work includes the following aspects: particle crushing in hydrate-bearing specimens, the investigation of natural core sediments focusing on compressibility and permeability anisotropy, coefficient of earth pressure at rest K_0 in hydrate-bearing specimens, and hydrate morphology and wave attenuation of hydrate-bearing clayey. Salient conclusions drawn from this research are as follows.

Particle Crushing in Hydrate-Bearing Sediments

- Hydrate crystals can increase skeleton stiffness, restrain particle rotation/rearrangement, and support part of the total stress. These processes result in less pronounced particle crushing in higher hydrate-saturated sediments. The loss of hydrate crystals during gas production can exacerbate particle crushing in hydrate deposits.
- Relatively large particles undergo surface grinding and breakage, and the crushed fine particles are very angular and slender.
- The total volumetric strain of hydrate-bearing sediments decreases with the increase of hydrate saturation, and the strain can be estimated using known hydrate saturation, skeleton stiffness, and effective stress.
- Reduction in particle size suggests a significant decrease in hydraulic conductivity,

and the degree of the reduction is estimated using changes in the particle size and volume of hydrate-bearing sediments.

Compressibility and Particle Crushing of Natural Sediments from Offshore India

- The stiffness of hydrate-bearing sediments is mainly governed by both the grain-supporting nature of the interconnected hydrate phase and the stress state on the sediment skeleton.
- The compression index C_c of hydrate-bearing sediments is influenced by compressing hydrate crystals and sediment grains rather than only compressing a water-filled void ratio.
- The presence of hydrate crystals can reduce the sediment's compressibility by approximately a factor of two.
- Hydrate crystals can support a portion of the load and interfere with the particle rearrangement of the post-crushing particles. More severe crushing is expected in larger particles with less hydrate subjected to higher stresses.

Coefficient of earth pressure at Rest K_0 in Hydrate-Bearing Sediments

- Hydrate formation only causes the sudden increase of K_0 once hydrate crystals start to be nucleated for sediment with high hydrate saturation, but the values of K_0 stabilize and return to their initial values with further hydrate nucleation and growth.
- K_0 of hydrate-bearing sediments decreases as vertical stress increases until cementation effects are dominant. The reduction is more pronounced in sediments

with higher hydrate saturation. With further increases of vertical stress (σ_v > 1 MPa), the values of K_0 start to recover with remarkable creep behavior.

- After the unloading process, higher hydrate saturation leads to higher K_0.
- The loss of hydrate crystals during hydrate dissociation causes the reduction of K_0.
- The presence of hydrate crystals plays a vital role in the mechanical behavior of hydrate-bearing specimens. The hydrate crystals can be considered as other solid materials that can support and share the load with soil particles.

Permeability Anisotropic of Hydrate-Bearing Sediment from Offshore India

- The permeability reduction caused by the increase of effective stress is more pronounced in hydrate-bearing sediments due to a limited fraction of fluid-filled volume that can compact in hydrate-bearing sediment.
- The permeability anisotropy of hydrate-bearing sediments increases exponentially with effective stress. The results indicate that the measured permeability from the permeameter along the vertical direction may underestimate the reservoir's flow performance.
- The presence of gas hydrate in sediments increases the air-entry pressure and residual water saturation but decreases the curve shape factor *m*-value (van Genuchten model), resulting in a steeper water retention curve.

Morphology and Physical Properties of THF Hydrate in Clayey Sediments

- It is reasonable to decide the hydrate saturation in fine-grained sediments using the volume fraction of hydrate over the total volume of sediments since the hydrate formation in fine-grained sediments is innately segregated and heterogeneous.
- The hydrate morphology and saturation are dominated by temperature conditions and constrained by water and mass transport.
- The low conversion ratios from stoichiometric solution to hydrate are observed, suggesting possible overestimation of THF hydrate saturation in clayey sediments based on the THF:H_2O ratio.
- For the segregated hydrate that acts as inclusion in the clay matrix, the bulk elastic properties can be well-predicted using the self-consistent model.
- *P* and *S*-wave attenuation increase with the increase of hydrate saturation.

7.2 Future Work

- In addition to investigating the effect of hydrate crystals on the evolution of particle size, research into this effect on particle shape, roundness, and angularity is also required.
- Visualization or numerical simulations of THF hydrate crystallization, cementation bonding and debonding between hydrate crystals and grain particles, and the movement of grain particles during loading and hydrate dissociation is needed.
- The Discrete Element Method (DEM) simulation is required to enhance the understanding of the coefficient of earth pressure at rest K_0 under various hydrate saturation and loading conditions

REFERENCES

Standard Test Method for Field Measurement of Infiltration Rate Using Double-Ring Infiltrometer with Sealed-Inner Ring.

Standard Test Method for Infiltration Rate of Soils in Field Using Double-Ring Infiltrometer.

ABBISS, C. 1981. Shear wave measurements of the elasticity of the ground. *Geotechnique,* 31**,** 91-104.

AJAYI, T., ANDERSON, B. J., SEOL, Y., BOSWELL, R. & MYSHAKIN, E. M. 2018. Key aspects of numerical analysis of gas hydrate reservoir performance: Alaska North Slope Prudhoe Bay Unit "L-Pad" hydrate accumulation. *Journal of Natural Gas Science and Engineering,* 51**,** 37-43.

ANDRAWES, K. Z. & EL-SOHBY, M. A. 1973. Factors affecting coefficient of earth pressure Ko. *Journal of Geotechnical and Geoenvironmental Engineering,* 99**,** 527-539.

BATHE, M., VAGLE, S., SAUNDERS, G. & LAMBSON, E. 1984. Ultrasonic wave velocities in the structure II clathrate hydrate THF· 17H 2 O. *Journal of materials science letters,* 3**,** 904-906.

BELLOTTI, R., FRETTI, C., GHIONNA, V. & PEDRONI, S. Compressibility and crushability of sands at high stresses. Proceedings of the international symposium on calibration chamber testing, Potsdam, New York, 1991. 79-90.

BERRYMAN, J. G. 1980. Long-wavelength propagation in composite elastic media I. Spherical inclusions. *J. Acoust. Soc. Am,* 68**,** 6.

BILLAM, J. 1972. Some aspects of the behaviour of granular materials at high pressures. *Stress-Strain behaviour of Soils, Proc. of the Roscoe Memorial Symp.***,** 69-80.

BOSWELL, R. 2009. Is gas hydrate energy within reach? *Science,* 325**,** 957-958.

BOSWELL, R. & COLLETT, T. 2006. The gas hydrates resource pyramid. *Natural Gas & Oil,* 304**,** 285-4541.

BOSWELL, R. & COLLETT, T. S. 2011. Current perspectives on gas hydrate resources. *Energy & environmental science,* 4**,** 1206-1215.

BOSWELL, R., MYSHAKIN, E., MORIDIS, G., KONNO, Y., COLLETT, T. S., REAGAN, M., AJAYI, T. & SEOL, Y. 2018. India National Gas Hydrate Program Expedition 02 summary of scientific results: Numerical simulation of reservoir response to depressurization. *Marine and Petroleum Geology,* 108**,** 154-166.

BOSWELL, R., YONEDA, J. & WAITE, W. F. 2019. India National Gas Hydrate Program Expedition 02 summary of scientific results: Evaluation of natural gas-hydrate-bearing pressure cores. *Marine and Petroleum Geology,* 108**,** 143-153.

BROOKER, E. W. & IRELAND, H. O. 1965. Earth pressures at rest related to stress history. *Canadian geotechnical journal,* 2**,** 1-15.

BUFFETT, B. & ZATSEPINA, O. Y. 2000. Formation of gas hydrate from dissolved gas in natural porous media. *Marine geology,* 164**,** 69-77.

BURLAND, J. 1990. On the compressibility and shear strength of natural clays. *Géotechnique,* 40**,** 329-378.

CARMAN, P. C. 1939. Permeability of saturated sands, soils and clays. *The Journal of Agricultural Science,* 29**,** 262-273.

CHA, S., OUAR, H., WILDEMAN, T. & SLOAN, E. 1988. A third-surface effect on hydrate formation. *The Journal of Physical Chemistry,* 92**,** 6492-6494.

CHENG, Y., BOLTON, M. & NAKATA, Y. 2004. Crushing and plastic deformation of soils simulated using DEM. *Geotechnique,* 54**,** 131-141.

CHO, G.-C., DODDS, J. & SANTAMARINA, J. C. 2006. Particle shape effects on packing density, stiffness, and strength; natural and crushed sands. *Journal of Geotechnical and Geoenvironmental Engineering,* 132**,** 591-602.

CHU, J. & GAN, C. 2004. Effect of void ratio on K 0 of loose sand. *Geotechnique,* 54**,** 285-288.

CHUHAN, F. A., KJELDSTAD, A., BJØRLYKKE, K. & HØEG, K. 2002. Porosity loss in sand by grain crushing—Experimental evidence and relevance to reservoir quality. *Marine and Petroleum Geology,* 19**,** 39-53.

CLENNELL, M. B., HOVLAND, M., BOOTH, J. S., HENRY, P. & WINTERS, W. J. 1999. Formation of natural gas hydrates in marine sediments: 1. Conceptual model of gas hydrate growth conditioned by host sediment properties. *Journal of Geophysical Research: Solid Earth,* 104**,** 22985-23003.

COLLETT, T. S., BOSWELL, R., WAITE, W. F., KUMAR, P., ROY, S. K., CHOPRA, K., SINGH, S. K., YAMADA, Y., TENMA, N. & POHLMAN, J. 2019. India National Gas Hydrate Program Expedition 02 summary of scientific results: gas hydrate systems along the eastern continental margin of India. *Marine and Petroleum Geology,* 108**,** 39-142.

COLLETT, T. S., JOHNSON, A., KNAPP, C. C. & BOSWELL, R. 2010. *Natural Gas Hydrates: Energy Resource Potential and Associated Geologic Hazards, AAPG Memoir 89*, The American Association of Petroleum Geologists.

COLLETT, T. S., RIEDEL, M., COCHRAN, J. R., BOSWELL, R., KUMAR, P. & SATHE, A. Indian continental margin gas hydrate prospects: results of the Indian National Gas Hydrate Program (NGHP) expedition 01. Proc. 6 th Int. Conf. Gas Hydrates, Vancouver., 2008. Citeseer.

COOK, A. E., ANDERSON, B. I., MALINVERNO, A., MROZEWSKI, S. & GOLDBERG, D. S. 2010. Electrical anisotropy due to gas hydrate-filled fractures. *Geophysics,* 75**,** F173-F185.

COOK, A. E., ANDERSON, B. I., RASMUS, J., SUN, K., LI, Q., COLLETT, T. S. & GOLDBERG, D. S. 2012. Electrical anisotropy of gas hydrate-bearing sand reservoirs in the Gulf of Mexico. *Marine and petroleum geology,* 34**,** 72-84.

COOP, M. & ATKINSON, J. 1993. The mechanics of cemented carbonate sands. *Geotechnique,* 43**,** 53-67.

COOP, M., SORENSEN, K., BODAS FREITAS, T. & GEORGOUTSOS, G. 2004. Particle breakage during shearing of a carbonate sand. *Géotechnique,* 54**,** 157-163.

CORTES, D. D., MARTIN, A. I., YUN, T. S., FRANCISCA, F. M., SANTAMARINA, J. C. & RUPPEL, C. 2009. Thermal conductivity of hydrate-bearing sediments. *Journal of Geophysical Research: Solid Earth,* 114.

CYGAN, R. T., LIANG, J.-J. & KALINICHEV, A. G. 2004. Molecular models of hydroxide, oxyhydroxide, and clay phases and the development of a general force field. *The Journal of Physical Chemistry B,* 108**,** 1255-1266.

DAI, S., KIM, J., XU, Y., WAITE, W. F., JANG, J., YONEDA, J., COLLETT, T. S. & KUMAR, P. 2019. Permeability anisotropy and relative permeability in sediments from the National Gas Hydrate Program Expedition 02, offshore India. *Marine and Petroleum Geology,* 108**,** 705-713.

DAI, S., LEE, C. & SANTAMARINA, J. C. 2011. Formation history and physical properties of sediments from the Mount Elbert Gas Hydrate Stratigraphic Test Well, Alaska North Slope. *Marine and Petroleum Geology,* 28**,** 427-438.

DAI, S., LEE, J. Y. & SANTAMARINA, J. C. 2014. Hydrate nucleation in quiescent and dynamic conditions. *Fluid Phase Equilibria,* 378**,** 107-112.

DAI, S. & SANTAMARINA, J. C. 2013. Water retention curve for hydrate-bearing sediments. *Geophysical Research Letters,* 40**,** 5637-5641.

DAI, S. & SANTAMARINA, J. C. 2014. Sampling disturbance in hydrate-bearing sediment pressure cores: NGHP-01 expedition, Krishna–Godavari Basin example. *Marine and Petroleum Geology,* 58**,** 178-186.

DAI, S. & SANTAMARINA, J. C. 2017. Hydrate-bearing clayey sediments: morphology, physical properties, production and engineering/geological implications. Georgia Tech Research Corporation, Atlanta, GA (United States).

DAI, S., SANTAMARINA, J. C., WAITE, W. F. & KNEAFSEY, T. J. 2012. Hydrate morphology: Physical properties of sands with patchy hydrate saturation. *Journal of Geophysical Research: Solid Earth,* 117**,** B11205.

DAI, S. & SEOL, Y. 2014. Water permeability in hydrate-bearing sediments: A pore-scale study. *Geophysical Research Letters,* 41**,** 4176-4184.

DAIGLE, H. 2016. Relative permeability to water or gas in the presence of hydrates in porous media from critical path analysis. *Journal of Petroleum Science and Engineering,* 146**,** 526-535.

DANIEL, D. E., ANDERSON, D. C. & BOYNTON, S. S. 1985. Fixed-wall versus flexible-wall permeameters. *Hydraulic barriers in soil and rock.* ASTM International.

DELLI, M. L. & GROZIC, J. L. 2014. Experimental determination of permeability of porous media in the presence of gas hydrates. *Journal of petroleum science and engineering,* 120**,** 1-9.

DVORKIN, J., HELGERUD, M. B., WAITE, W. F., KIRBY, S. H. & NUR, A. 2000. Introduction to physical properties and elasticity models. *Natural Gas Hydrate***,** 245-260.

EINAV, I. 2007a. Breakage mechanics—part I: theory. *Journal of the Mechanics and Physics of Solids,* 55**,** 1274-1297.

EINAV, I. 2007b. Breakage mechanics—Part II: Modelling granular materials. *Journal of the Mechanics and Physics of Solids,* 55**,** 1298-1320.

FUJII, T., SUZUKI, K., TAKAYAMA, T., TAMAKI, M., KOMATSU, Y., KONNO, Y., YONEDA, J., YAMAMOTO, K. & NAGAO, J. 2015. Geological setting and characterization of a methane hydrate reservoir distributed at the first offshore production test site on the Daini-Atsumi Knoll in the eastern Nankai Trough, Japan. *Marine and Petroleum Geology,* 66**,** 310-322.

GLASBY, G. 2003. Potential impact on climate of the exploitation of methane hydrate deposits offshore. *Marine and petroleum geology,* 20**,** 163-175.

GROZIC, J. 2010. Interplay between gas hydrates and submarine slope failure. *Submarine mass movements and their consequences.* Springer.

GUERIN, G. & GOLDBERG, D. 2002. Sonic waveform attenuation in gas hydrate-bearing sediments from the Mallik 2L-38 research well, Mackenzie Delta, Canada. *Journal of Geophysical Research: Solid Earth,* 107**,** EPM 1-1-EPM 1-11.

GUIMARAES, M., VALDES, J., PALOMINO, A. & SANTAMARINA, J. 2007. Aggregate production: fines generation during rock crushing. *International journal of mineral processing,* 81**,** 237-247.

HAGERTY, M., HITE, D., ULLRICH, C. & HAGERTY, D. 1993. One-dimensional high-pressure compression of granular media. *Journal of Geotechnical Engineering,* 119**,** 1-18.

HANDA, Y. P. & STUPIN, D. Y. 1992. Thermodynamic properties and dissociation characteristics of methane and propane hydrates in 70-. ANG.-radius silica gel pores. *The Journal of Physical Chemistry,* 96**,** 8599-8603.

HARDIN, B. O. 1985. Crushing of Soil Particles. *Journal of Geotechnical Engineering,* 111**,** 1177-1192.

HELGERUD, M., WAITE, W., KIRBY, S. & NUR, A. 2003. Measured temperature and pressure dependence of V p and V s in compacted, polycrystalline sI methane and sII methane ethane hydrate. *Canadian journal of physics,* 81**,** 47-53.

HENRY, P., THOMAS, M. & CLENNELL, M. B. 1999. Formation of natural gas hydrates in marine sediments: 2. Thermodynamic calculations of stability conditions in porous sediments. *Journal of Geophysical Research: Solid Earth,* 104**,** 23005-23022.

HOLDER, G., KAMATH, V. & GODBOLE, S. 1984. The potential of natural gas hydrates as an energy resource. *Annual Review of Energy,* 9**,** 427-445.

HOLLAND, M., SCHULTHEISS, P. & ROBERTS, J. 2019. Gas hydrate saturation and morphology from analysis of pressure cores acquired in the Bay of Bengal during expedition NGHP-02, offshore India. *Marine and Petroleum Geology,* 108**,** 407-423.

HYODO, M., WU, Y., ARAMAKI, N. & NAKATA, Y. 2016. Undrained monotonic and cyclic shear response and particle crushing of silica sand at low and high pressures. *Canadian Geotechnical Journal,* 54**,** 207-218.

HYODO, M., YONEDA, J., YOSHIMOTO, N. & NAKATA, Y. 2013. Mechanical and dissociation properties of methane hydrate-bearing sand in deep seabed. *Soils and foundations,* 53**,** 299-314.

JANG, J., DAI, S., YONEDA, J., WAITE, W. F., STERN, L. A., BOZE, L.-G., COLLETT, T. S. & KUMAR, P. 2019. Pressure core analysis of geomechanical and fluid flow properties of seals associated with gas hydrate-bearing reservoirs in the Krishna-Godavari Basin, offshore India. *Marine and Petroleum Geology,* 108**,** 537-550.

JANG, J. & SANTAMARINA, J. C. 2015. Fines classification based on sensitivity to pore-fluid chemistry. *Journal of Geotechnical and Geoenvironmental Engineering,* 142**,** 06015018.

JOHNSON, A., PATIL, S. & DANDEKAR, A. 2011. Experimental investigation of gas-water relative permeability for gas-hydrate-bearing sediments from the Mount Elbert Gas Hydrate Stratigraphic Test Well, Alaska North Slope. *Marine and petroleum geology,* 28**,** 419-426.

JUNG, J. W. & SANTAMARINA, J. C. 2011. Hydrate adhesive and tensile strengths. *Geochemistry Geophysics Geosystems,* 12**,** Q08003.

KANG, D. H., YUN, T. S., KIM, K. Y. & JANG, J. 2016. Effect of hydrate nucleation mechanisms and capillarity on permeability reduction in granular media. *Geophysical Research Letters,* 43**,** 9018-9025.

KAYEN, R. E. & LEE, H. J. 1991. Pleistocene slope instability of gas hydrate-laden sediment on the Beaufort sea margin. *Marine Georesources & Geotechnology,* 10**,** 125-141.

KIM, J., DAI, S., JANG, J., WAITE, W. F., COLLETT, T. S. & KUMAR, P. 2019a. Compressibility and particle crushing of Krishna-Godavari Basin sediments from offshore India: Implications for gas production from deep-water gas hydrate deposits. *Marine and Petroleum Geology,* 108**,** 697-704.

KIM, J., ZHANG, Y., SEOL, Y. & DAI, S. 2019b. Particle crushing in hydrate-bearing sands. *Geomechanics for Energy and the Environment***,** 100133.

KLEINBERG, R., FLAUM, C. & COLLETT, T. 2005. Magnetic resonance log of JAPEX/JNOC/GSC et al. Mallik 5L-38 gas hydrate production research well: gas hydrate saturation, growth habit, and relative permeability. *BULLETIN-GEOLOGICAL SURVEY OF CANADA,* 585**,** 114.

KLEINBERG, R., FLAUM, C., GRIFFIN, D., BREWER, P., MALBY, G., PELTZER, E. & YESINOWSKI, J. 2003. Deep sea NMR: Methane hydrate growth habit in

porous media and its relationship to hydraulic permeability, deposit accumulation, and submarine slope stability. *Journal of Geophysical Research: Solid Earth,* 108.

KNEAFSEY, T. J., SEOL, Y., GUPTA, A. & TOMUTSA, L. 2011. Permeability of laboratory-formed methane-hydrate-bearing sand: measurements and observations using X-ray computed tomography. *SPE Journal,* 16**,** 78-94.

KONNO, Y., JIN, Y., YONEDA, J., KIDA, M., EGAWA, K., ITO, T., SUZUKI, K. & NAGAO, J. 2015a. Effect of methane hydrate morphology on compressional wave velocity of sandy sediments: Analysis of pressure cores obtained in the Eastern Nankai Trough. *Marine and Petroleum Geology,* 66**,** 425-433.

KONNO, Y., YONEDA, J., EGAWA, K., ITO, T., JIN, Y., KIDA, M., SUZUKI, K., FUJII, T. & NAGAO, J. 2015b. Permeability of sediment cores from methane hydrate deposit in the Eastern Nankai Trough. *Marine and petroleum geology,* 66**,** 487-495.

KOZENY, J. 1927. Uber kapillare leitung der wasser in boden. *Royal Academy of Science, Vienna, Proc. Class I,* 136**,** 271-306.

KUMAR, P., COLLETT, T., SHUKLA, K., YADAV, U., LALL, M. & VISHWANATH, K. 2019. India National Gas Hydrate Program Expedition-02: Operational and Technical Summary. *Mar. Petrol. Geol.,* 108**,** 3-38.

KVENVOLDEN, K. A. 1993. Gas hydrates—geological perspective and global change. *Reviews of geophysics,* 31**,** 173-187.

LADE, P. V., YAMAMURO, J. A. & BOPP, P. A. 1996. Significance of particle crushing in granular materials. *Journal of Geotechnical Engineering,* 122**,** 309-316.

LEE, J., FRANCISCA, F. M., SANTAMARINA, J. C. & RUPPEL, C. 2010a. Parametric study of the physical properties of hydrate-bearing sand, silt, and clay sediments: 2. Small-strain mechanical properties. *Journal of Geophysical Research: Solid Earth,* 115.

LEE, J., LEE, D., PARK, D., KYUNG, D., KIM, G. & KIM, I. 2016. Effect of freezing and thawing on K_0 geostatic stress state for granular materials. *Granular Matter,* 18**,** 69.

LEE, J., SANTAMARINA, J. C. & RUPPEL, C. 2010b. Volume change associated with formation and dissociation of hydrate in sediment. *Geochemistry, Geophysics, Geosystems,* 11.

LEE, J., YUN, T., SANTAMARINA, J. & RUPPEL, C. 2007. Observations related to tetrahydrofuran and methane hydrates for laboratory studies of hydrate-bearing sediments. *Geochemistry, Geophysics, Geosystems,* 8.

LEE, J., YUN, T. S., LEE, D. & LEE, J. 2013. Assessment of K0 correlation to strength for granular materials. *Soils and Foundations,* 53**,** 584-595.

LEE, K. L. & FARHOOMAND, I. 1967. Compressibility and crushing of granular soil in anisotropic triaxial compression. *Canadian geotechnical journal,* 4**,** 68-86.

LEE, M. & COLLETT, T. 2009. Gas hydrate saturations estimated from fractured reservoir at Site NGHP-01-10, Krishna-Godavari Basin, India. *Journal of Geophysical Research: Solid Earth,* 114.

LEI, L. 2017. *Gas hydrate in fine-grained sediments—laboratory studies and coupled processes analyses.* Georgia Institute of Technology.

LEI, L. & SANTAMARINA, J. 2018. Laboratory Strategies for Hydrate Formation in Fine-Grained Sediments. *Journal of Geophysical Research: Solid Earth,* 123**,** 2583-2596.

LEROUEIL, S. & VAUGHAN, P. 2009. The general and congruent effects of structure in natural soils and weak rocks. *Selected papers on geotechnical engineering by PR Vaughan.* Thomas Telford Publishing.

LO, K. Y. & ROY, M. 1973. Response of particulate materials at high pressures. *Soils and Foundations,* 13**,** 61-76.

MAHABADI, N., DAI, S., SEOL, Y., SUP YUN, T. & JANG, J. 2016a. The water retention curve and relative permeability for gas production from hydrate-bearing sediments: pore-network model simulation. *Geochemistry, Geophysics, Geosystems,* 17**,** 3099-3110.

MAHABADI, N. & JANG, J. 2014. Relative water and gas permeability for gas production from hydrate-bearing sediments. *Geochemistry, geophysics, geosystems,* 15**,** 2346-2353.

MAHABADI, N., ZHENG, X. & JANG, J. 2016b. The effect of hydrate saturation on water retention curves in hydrate-bearing sediments. *Geophysical Research Letters,* 43**,** 4279-4287.

MARÍN-MORENO, H., SAHOO, S. & BEST, A. 2017. Theoretical modeling insights into elastic wave attenuation mechanisms in marine sediments with pore-filling methane hydrate. *Journal of Geophysical Research: Solid Earth,* 122**,** 1835-1847.

MAVKO, G. M. & NUR, A. 1979. Wave attenuation in partially saturated rocks. *Geophysics,* 44**,** 161-178.

MAYNE, P. W. & KULHAWY, F. H. 1982. Ko- OCR Relationships in Soil. *Journal of the Soil Mechanics and Foundations Division,* 108**,** 851-872.

MCDOWEL, G. R. & BOLTON, M. D. 1998. On the micromechanics of crushable aggregates. *Géotechnique,* 48**,** 667-679.

MCDOWELL, G., BOLTON, M. & ROBERTSON, D. 1996. The fractal crushing of granular materials. *Journal of the Mechanics and Physics of Solids,* 44**,** 2079-2101.

MCDOWELL, G. R. 1999. Micromechanics of Clastic Soil. *Proceedings of the International Workshop on Soil Crushability.* Yamaguchi, Japan.

MCKEE, C. R., BUMB, A. C. & KOENIG, R. A. 1988. Stress-dependent permeability and porosity of coal and other geologic formations. *SPE formation evaluation,* 3**,** 81-91.

MESRI, G. & VARDHANABHUTI, B. 2009. Compression of granular materials. *Canadian Geotechnical Journal,* 46**,** 369-392.

MINAGAWA, H., OHMURA, R., KAMATA, Y., NAGAO, J., EBINUMA, T., NARITA, H. & MASUDA, Y. 2009. Water permeability of porous media containing methane hydrate as controlled by the methane-hydrate growth process. *The American Association of Petroleum Geologists*, 734-739.

MORIDIS, G. J. Numerical studies of gas production from methane hydrates. SPE Gas Technology Symposium, 2002. Society of Petroleum Engineers.

MORIDIS, G. J. 2008. Toward production from gas hydrates: current status, assessment of resources, and simulation-based evaluation of technology and potential. *SPE Reservoir Evaluation & Engineering,* 12**,** 745-771.

MORIDIS, G. J., COLLETT, T. S., BOSWELL, R., KURIHARA, M., REAGAN, M. T., KOH, C. & SLOAN, E. D. 2009. Toward production from gas hydrates: current status, assessment of resources, and simulation-based evaluation of technology and potential. *SPE Reservoir Evaluation & Engineering,* 12**,** 745-771.

MORIDIS, G. J. & REAGAN, M. T. 2007. Strategies for gas production from oceanic class 3 hydrate accumulations. *SPE Reservoir Evaluation & Engineering*.

MULLIN, J. W. 2001. *Crystallization*, Elsevier.

MYSHAKIN, E. M., SEOL, Y., LIN, J.-S., UCHIDA, S., COLLETT, T. S. & BOSWELL, R. 2019. Numerical simulations of depressurization-induced gas production from an interbedded turbidite gas hydrate-bearing sedimentary section in the offshore India: Site NGHP-02-16 (Area-B). *Marine and Petroleum Geology,* 108**,** 619-638.

NAGAO, J., YONEDA, J., KONNO, Y. & JIN, Y. Development of the Pressure-core Nondestructive Analysis Tools (PNATs) for Methane Hydrate Sedimentary Cores. EGU General Assembly Conference Abstracts, 2015.

NAKATA, Y., BOLTON, M. D. & CHENG, Y. P. 2005. Relating particle characteristics to macro behavior of DEM crushable material. *Powders and grains. Taylor & Francis Group, London***,** 1387-1391.

NAKATA, Y., HYODO, M., HYDE, A. F., KATO, Y. & MURATA, H. 2001. Microscopic particle crushing of sand subjected to high pressure one-dimensional compression. *Soils and foundations,* 41**,** 69-82.

NORTHCUTT, S. & WIJEWICKREME, D. 2013. Effect of particle fabric on the coefficient of lateral earth pressure observed during one-dimensional compression of sand. *Canadian Geotechnical Journal,* 50**,** 457-466.

OKOCHI, Y. & TATSUOKA, F. 1984. Some factors affecting K0-values of sand measured in triaxial cell. *Soils and Foundations,* 24**,** 52-68.

PARK, S.-H. & SPOSITO, G. 2003. Do montmorillonite surfaces promote methane hydrate formation? Monte Carlo and molecular dynamics simulations. *The Journal of Physical Chemistry B,* 107**,** 2281-2290.

PARKER, J., LENHARD, R. & KUPPUSAMY, T. 1987. A parametric model for constitutive properties governing multiphase flow in porous media. *Water Resources Research,* 23**,** 618-624.

PHADNIS, H. & SANTAMARINA, J. 2011. Bacteria in sediments: pore size effects. *Geotechnique Letters,* 1**,** 91-93.

PINKERT, S. & GROZIC, J. L. 2014. Failure mechanisms in cemented hydrate-bearing sands. *Journal of Chemical & Engineering Data,* 60**,** 376-382.

POHL, M., PRASAD, M. & BATZLE, M. L. 2018. Ultrasonic attenuation of pure tetrahydrofuran hydrate. *Geophysical Prospecting,* 66**,** 1349-1357.

PRIEST, J. A., BEST, A. I. & CLAYTON, C. R. I. 2006. Attenuation of seismic waves in methane gas hydrate-bearing sand. *Geophysical Journal International,* 164**,** 149-159.

PRIEST, J. A., DRUCE, M., ROBERTS, J., SCHULTHEISS, P., NAKATSUKA, Y. & SUZUKI, K. 2015. PCATS Triaxial: A new geotechnical apparatus for characterizing pressure cores from the Nankai Trough, Japan. *Marine and petroleum geology,* 66**,** 460-470.

REES, E. V., KNEAFSEY, T. J. & SEOL, Y. 2011. Methane hydrate distribution from prolonged and repeated formation in natural and compacted sand samples: X-ray CT observations. *Journal of Geological Research,* 2011.

REN, X. & SANTAMARINA, J. 2018. The hydraulic conductivity of sediments: A pore size perspective. *Engineering Geology,* 233**,** 48-54.

RIEDEL, M., COLLETT, T., KUMAR, P., SATHE, A. & COOK, A. 2010. Seismic imaging of a fractured gas hydrate system in the Krishna–Godavari Basin offshore India. *Marine and Petroleum Geology,* 27**,** 1476-1493.

RUPPEL, C. D. & POHLMAN, J. W. 2008. Climate change and global carbon cycle: Perspectives and opportunities. *Fire in the Ice: NETL Methane Hydrate Newsletter,* 8**,** 5-8.

SAAR, M. O. & MANGA, M. 1999. Permeability-porosity relationship in vesicular basalts. *Geophysical Research Letters,* 26**,** 111-114.

SADREKARIMI, A. & OLSON, S. M. 2010. Particle damage observed in ring shear tests on sands. *Canadian Geotechnical Journal,* 47**,** 497-515.

SANTAMARINA, J., KLEIN, K., WANG, Y. & PRENCKE, E. 2002. Specific surface: determination and relevance. *Canadian Geotechnical Journal,* 39**,** 233-241.

SANTAMARINA, J. C., DAI, S., JANG, J. & TERZARIOL, M. 2012. Pressure core characterization tools for hydrate-bearing sediments. *Scientific Drilling,* 14**,** 44-48.

SANTAMARINA, J. C., DAI, S., TERZARIOL, M., JANG, J., WAITE, W. F., WINTERS, W. J., NAGAO, J., YONEDA, J., KONNO, Y. & FUJII, T. 2015. Hydro-bio-geomechanical properties of hydrate-bearing sediments from Nankai Trough. *Marine and Petroleum Geology,* 66**,** 434-450.

SANTAMARINA, J. C. & RUPPEL, C. 2010. The impact of hydrate saturation on the mechanical, electrical, and thermal properties of hydrate-bearing sand, silts, and clay. *Geophysical Characterization of Gas Hydrates, Geophys. Dev. Ser,* 14**,** 373-384.

SCHULTHEISS, P., FRANCIS, T., HOLLAND, M., ROBERTS, J., AMANN, H., PARKES, R., MARTIN, D., ROTHFUSS, M., TYUNDER, F. & JACKSON, P. 2006. Pressure coring, logging and subsampling with the HYACINTH system. *Geological Society, London, Special Publications,* 267**,** 151-163.

SHIN, H. & SANTAMARINA, J. C. 2009. Mineral dissolution and the evolution of k 0. *Journal of Geotechnical and Geoenvironmental Engineering,* 135**,** 1141-1147.

SLOAN, E. D. & KOH, C. 2007. *Clathrate hydrates of natural gases*, CRC press.

SOEDER, D. J. 1988. Porosity and permeability of eastern Devonian gas shale. *SPE Formation Evaluation,* 3**,** 116-124.

SPANGENBERG, E., KULENKAMPFF, J., NAUMANN, R. & ERZINGER, J. 2005. Pore space hydrate formation in a glass bead sample from methane dissolved in water. *Geophysical Research Letters,* 32.

SPANGENBERG, E., PRIEGNITZ, M., HEESCHEN, K. & SCHICKS, J. M. 2014. Are laboratory-formed hydrate-bearing systems analogous to those in nature? *Journal of Chemical & Engineering Data,* 60**,** 258-268.

SPOSITO, G., SKIPPER, N. T., SUTTON, R., PARK, S.-H., SOPER, A. K. & GREATHOUSE, J. A. 1999. Surface geochemistry of the clay minerals. *Proceedings of the National Academy of Sciences,* 96**,** 3358-3364.

STRAUCH, B., SCHICKS, J. M., LUZI-HELBING, M., NAUMANN, R. & HERBST, M. 2018. The difference between aspired and acquired hydrate volumes–A laboratory study of THF hydrate formation in dependence on initial THF: H2O ratios. *The Journal of Chemical Thermodynamics,* 117**,** 193-204.

TOHIDI, B., ANDERSON, R., CLENNELL, M. B., BURGASS, R. W. & BIDERKAB, A. B. 2001. Visual observation of gas-hydrate formation and dissociation in synthetic porous media by means of glass micromodels. *Geology,* 29**,** 867-870.

TOKSÖZ, M., JOHNSTON, D. H. & TIMUR, A. 1979. Attenuation of seismic waves in dry and saturated rocks: I. Laboratory measurements. *Geophysics,* 44**,** 681-690.

UCHIDA, T., WASEDA, A. & NAMIKAWA, T. 2009. Methane accumulation and high concentration of gas hydrate in marine and terrestrial sandy sediments. *The American Association of Petroleum Geologists*.

UDDIN, M., WRIGHT, J., DALLIMORE, S. & COOMBE, D. 2012. Gas hydrate production from the Mallik reservoir: numerical history matching and long-term production forecasting. *Geological Survey of Canada, Bulletin,* 601**,** 261-289.

VAN GENUCHTEN, M. T. 1980. A closed-form equation for predicting the hydraulic conductivity of unsaturated soils 1. *Soil science society of America journal,* 44**,** 892-898.

VIGGIANI, G. & ATKINSON, J. 1995. Interpretation of bender element tests. *Géotechnique,* 45**,** 149-154.

WAITE, W. F., JANG, J., COLLETT, T. S. & KUMAR, P. 2019. Downhole physical property-based description of a gas hydrate petroleum system in NGHP-02 Area C: A channel, levee, fan complex in the Krishna-Godavari Basin offshore eastern India. *Marine and Petroleum Geology,* 108**,** 272-295.

WAITE, W. F., KNEAFSEY, T. J., WINTERS, W. J. & MASON, D. 2008. Physical property changes in hydrate-bearing sediment due to depressurization and subsequent repressurization. *Journal of Geophysical Research: Solid Earth,* 113.

WAITE, W. F., SANTAMARINA, J. C., CORTES, D. D., DUGAN, B., ESPINOZA, D. N., GERMAINE, J., JANG, J., JUNG, J., KNEAFSEY, T. J. & SHIN, H. 2009. Physical properties of hydrate-bearing sediments. *Reviews of geophysics,* 47.

WANATOWSKI, D. & CHU, J. 2007. K 0 of sand measured by a plane-strain apparatus. *Canadian Geotechnical Journal,* 44**,** 1006-1012.

WITT, K.-J. & BRAUNS, J. 1983. Permeability-anisotropy due to particle shape. *Journal of geotechnical engineering,* 109**,** 1181-1187.

XIAO, Y., LIU, H., DING, X., CHEN, Y., JIANG, J. & ZHANG, W. 2015. Influence of particle breakage on critical state line of rockfill material. *International Journal of Geomechanics,* 16**,** 04015031.

XU, Y., SEOL, Y., JANG, J. & DAI, S. 2017. Water and gas flows in hydrate-bearing sediments. *Geotechnical Frontiers 2017.*

YAMAMURO, J. A., BOPP, P. A. & LADE, P. V. 1996. One-dimensional compression of sands at high pressures. *Journal of geotechnical engineering,* 122**,** 147-154.

YANG, Y. & APLIN, A. C. 2010. A permeability–porosity relationship for mudstones. *Marine and Petroleum Geology,* 27**,** 1692-1697.

YAO, X., QI, J. & YU, F. 2014. Study on lateral earth pressure coefficient at rest for frozen soils. *Journal of Offshore Mechanics and Arctic Engineering,* 136**,** 011301.

YONEDA, J., JIN, Y., KATAGIRI, J. & TENMA, N. 2016. Strengthening mechanism of cemented hydrate-bearing sand at microscales. *Geophysical Research Letters,* 43**,** 7442-7450.

YONEDA, J., OSHIMA, M., KIDA, M., KATO, A., KONNO, Y., JIN, Y., JANG, J., WAITE, W. F., KUMAR, P. & TENMA, N. 2019a. Permeability variation and anisotropy of gas hydrate-bearing pressure-core sediments recovered from the Krishna–Godavari Basin, offshore India. *Marine and Petroleum Geology,* 108**,** 524-536.

YONEDA, J., OSHIMA, M., KIDA, M., KATO, A., KONNO, Y., JIN, Y. & TENMA, N. 2019b. Consolidation and hardening behavior of hydrate-bearing pressure-core sediments recovered from the Krishna–Godavari Basin, offshore India. *Marine and Petroleum Geology,* 108**,** 512-523.

YUN, T., FRANCISCA, F., SANTAMARINA, J. & RUPPEL, C. 2005. Compressional and shear wave velocities in uncemented sediment containing gas hydrate. *Geophysical Research Letters,* 32.

YUN, T. S. & EVANS, T. M. 2011. Evolution of at-rest lateral stress for cemented sands: experimental and numerical investigation. *Granular Matter,* 13**,** 671.

YUN, T. S., LEE, C., LEE, J. S., BAHK, J. J. & SANTAMARINA, J. C. 2011. A pressure core based characterization of hydrate-bearing sediments in the Ulleung Basin, Sea of Japan (East Sea). *Journal of Geophysical Research: Solid Earth,* 116.

YUN, T. S. & SANTAMARINA, J. C. 2005. Decementation, softening, and collapse: changes in small-strain shear stiffness in k 0 loading. *Journal of Geotechnical and Geoenvironmental engineering,* 131**,** 350-358.

YUN, T. S., SANTAMARINA, J. C. & RUPPEL, C. 2007. Mechanical properties of sand, silt, and clay containing tetrahydrofuran hydrate. *Journal of Geophysical Research: Solid Earth,* 112.

ZEMANEK JR, J. & RUDNICK, I. 1961. Attenuation and dispersion of elastic waves in a cylindrical bar. *The Journal of the Acoustical Society of America,* 33**,** 1283-1288.

ZHENG, W. & TANNANT, D. 2016. Frac sand crushing characteristics and morphology changes under high compressive stress and implications for sand pack permeability. *Canadian Geotechnical Journal,* 53**,** 1412-1423.

ZHU, F., CLARK, J. I. & PAULIN, M. J. 1995. Factors affecting at-rest lateral stress in artificially cemented sands. *Canadian geotechnical journal,* 32**,** 195-203.